

**UCSF**

**UC San Francisco Electronic Theses and Dissertations**

**Title**

Rapid and Robust Non-Cartesian Magnetic Resonance Imaging Methods

**Permalink**

<https://escholarship.org/uc/item/0ck0q91f>

**Author**

Jiang, Wenwen

**Publication Date**

2016

**Supplemental Material**

<https://escholarship.org/uc/item/0ck0q91f#supplemental>

Peer reviewed|Thesis/dissertation

Rapid and Robust Non-Cartesian Magnetic Resonance Imaging Methods

by

Wenwen Jiang

DISSERTATION

Submitted in partial satisfaction of the requirements for the degree of

DOCTOR OF PHILOSOPHY

in

Bioengineering

in the

GRADUATE DIVISION

of the

UNIVERSITY OF CALIFORNIA, SAN FRANCISCO

AND

UNIVERSITY OF CALIFORNIA, BERKELEY

Copyright 2016

by

Wenwen Jiang

## Acknowledgments

As I have two advisors across two campuses (UC Berkeley/UCSF), the length of my acknowledgments doubles. First and foremost, I would like to thank my advisors Peder Larson and Michael (Miki) Lustig:

I was very lucky to be Peder's first Ph.D. student! Peder is the most patient and gentle person I have ever known. I have always been impressed by his broad knowledge on MR physics, pulse sequence, EPIC and many more. His commitment to excellence and dedicated efforts for improvements set him a role model for me! Although Peder's schedule is very full every single day, he always makes sure he has time to talk to me and make sure everything is on right track with me. I appreciate his patience to discuss all the naive ideas I have and his sound advices on scientific writing and presentation over the past five years. His dedicated attitude and passion to research have great influences on me and my future paths.

It was Miki who introduced me to the marvelous world of MRI when I took his class. I was impressed by his vivid classes and his amazing devotion to MRI. It was through Miki's Principle of MRI class, that I started my first project: concentric rings trajectory for  $^{13}\text{C}$  MRSI. He had the power to explain every complicated idea in a super clear way and his class was always a lot of fun. Since I started to work with Miki, every day I have appreciated his faith in my abilities and in my potential, even though I had never done any MRI research before. I appreciate his patience to teach me cvx from scratch, and his kindness to give me so much freedom to learn and pursue my own interest. I sincerely thank him for guiding me, helping me, and driving me to where I am today.

This dissertation was not made possible without Miki and Peder. I learned so much from both their intellects and characters (Miki and Peder do have very different characters and I regard them as my academic father and mother respectively). I could not have had a better advisor than both of them together. I thank them a million to be my advisors!

Steve Conolly has always been a great person for advice and encouragement. I took his class, rotated with him, and GSied his class. I enjoyed talking to Steve a lot. He always has

very insightful ideas about life and career paths. Steve constantly reminds me of the bigger impacts of my work, and inspires me to keep working hard and be critical about my own research. I thank him for all these advices!

Michael Ohliger always has very insightful ideas about research and clinical applications. His enthusiasm and insights truly influence everyone in the big office! I also thank him for proofreading this dissertation draft, even though I sent it very late.

I am extremely lucky to work with and learn from my fellows during the past five-and-a-half years and would like to thank all of them! To my colleagues in Berkeley: from Martin Uecker, I learned “Martin is always right”. I also learned Anita Flynn’s Law: “it is always a connection problem”. It actually solves a lot of problems.

I learned gridding methods from Pat. Pat Virtue is a very energetic man and very helpful. I will never forget that he saved my life during our first group trip. I could not swim during the trip to Arroyo Seco (where 90% of the trail is in water), and ended up holding onto Pat’s leg to survive the trip.

When Jon Tamir is around, the group feels more team cohesive. He always brings people together, and connects with everyone. He manages all the computing resources and also is one of the main contributors to BART. I learned a lot of useful tips about computing and reconstruction from him. Joe Corea is the hardware engineer in our group. Every time I have hardware questions, Joe is always the right person to ask. He is also very good at making stuff far beyond my imagination (such as making a turkey rocket).

By the way, I still think Joe and Jon resemble each other.

Dara Bahri was an undergrad when I joined the lab. We took two classes together but we did not talk to each other too much. We became close friends when he shared his little secret with me (only). But it turned out he told everyone else in the group about the same thing... When Dara is around, there are always more laughters. Sana Varizi was the youngest post-undergrad I had ever known! She started to work in the lab earlier than I did. She gave me a lot of practical tips on programming, very useful guidances, though she is much younger than I am!

To my colleagues in UCSF: thank you for being the best cubicle mates, offering scientific insights, and giving me so much help! I thank Jeremy Gordon for volunteering for many of my scans and providing very good SNR! He is a very good speaker and gave me many suggestions on academic talks. Peng Cao also volunteered and helped me to set up many of my scans. Peng is very capable and hardworking! He always offers his help to me.

Shuyu Tang sits next to me for four years and also lives very close to me. I got a lot of help from him, including research, scans, EPIC programming, and even moving. He has been very helpful, especially when we need him to take the carpool lane from SF to Berkeley... Although Xucheng Zhu is the most junior graduate student in the lab, we worked very closely with each other on the motion project. We share a common curiosity for research topics and also passion for good food!

I also want to thank my collaborators for their great contributions: Kevin Johnson, Scott Nagle, Thomas Hope, and Mariya Doneva; my senior Bioengineering fellows in UCSF to help me start my Ph.D. journey: Peter Shin, Galen Reed, Christine Swisher and Cornelius Von Morze; and my junior colleagues in both Berkeley and UCSF for their support: Michael Kellman, Teresa Ou, Sid Iyer, Hong Shang, and Zihan Zhu. Thank you for being the best coworkers! My Ph.D. life has been so wonderful with you folks!

I want to thank all my friends in Berkeley for their friendship and support: Jue Chen, Xiaofei Hu, Yifan Jiang, Te Ke, Paul Keselman, Harrison Liu, Kun Li, Tuan Tran, Jun Xie, Yang Yang, Weixi Zhong, Jie Zou.

Lastly, I thank Frank Ong, who is a very intelligent engineer, considerate colleague and also my boyfriend! Frank has comforted me when I had difficult times and encouraged me when times were tough. Frank has inspired me with a lot of research ideas. I really appreciate Frank's considerable patience to read my abstracts, papers and listen to my practice talks over and over again. I would be nowhere without the unfailing support from Frank!

Wenwen Jiang

*December 2016*

## Abstract

Rapid and Robust Non-Cartesian Magnetic Resonance Imaging Methods

by

Wenwen Jiang

Doctor of Philosophy in Bioengineering

University of California, San Francisco

Professor Michael Lustig, Co-chair

Professor Peder E.Z. Larson, Co-chair

Magnetic resonance imaging (MRI) is a powerful non-invasive medical imaging modality. Unlike computed tomography (CT), MRI does not use ionizing radiation and provides a broad range of soft-tissue contrasts. However, imaging speed remains a fundamental limitation to many potential applications.

Using non-Cartesian trajectories to efficiently traverse k-space has been a promising research direction for rapid MRI. The ability to traverse k-space rapidly is also beneficial for applications where the signal is short-lived. In addition, many non-Cartesian trajectories result in incoherent image artifacts that can spread across dimensions. This allows for high acceleration factors when incorporated with parallel imaging and compressed sensing.

On the other hand, non-Cartesian trajectories are not widely adopted clinically because they are often sensitive to many error sources, such as gradient delays and eddy currents. Hence, it is crucial to develop non-Cartesian imaging methods that provide both rapid k-space traversal and robustness to potential system errors at the same time. This dissertation considers two particular applications that require rapid and robust imaging methods: hyper-

polarized  $^{13}\text{C}$  MR spectroscopic imaging (MRSI) where the polarized signal is short-lived, and pulmonary imaging where the transverse magnetization decays rapidly.

For hyperpolarized  $^{13}\text{C}$  MRSI, this dissertation proposes using a concentric rings trajectory (CRT) as the image acquisition method. CRT provides the essential scan time efficiency and robustness to system imperfections: (1) the image acquisition time is halved compared with Cartesian counterparts; (2) CRT is inherently robust to first-order eddy currents and gradient system delays; (3) this sampling scheme results in low noise amplification for parallel imaging. Preclinical studies demonstrate the feasibility and efficacy of using CRT in hyperpolarized  $^{13}\text{C}$  MRSI.

For pulmonary imaging, this dissertation proposes using a 3D radial based ultrashort echo time (UTE) imaging sequence, combined with a novel reconstruction framework to provide motion robust high resolution 3D images in a 5-minute acquisition time. In particular, this dissertation develops: (1) a lower-resolution, high frame rate dynamic 3D self-navigator, which provides robust and accurate motion estimation; (2) high-resolution image reconstruction techniques to compensate for respiratory motion with soft-gating and motion-resolved strategies. For further acceleration, this work incorporates the above techniques into an iterative reconstruction framework with parallel imaging and compressed sensing.

Despite its motion robustness and fast acquisition time, the proposed pulmonary imaging method is susceptible to gradient delays. Motivated by this problem, a general solution for correcting gradient system delays is proposed by exploiting data redundancy in multi-channel coil array data. The proposed method requires no additional calibration scans, and estimates both gradient system delays and auto-calibration data simultaneously. This work is general to many other non-Cartesian imaging trajectories as validated by both simulation and in vivo scans.



# Table of Contents

<b>1</b>	<b>Introduction</b>	<b>1</b>
1.1	Outline . . . . .	3
<b>2</b>	<b>Principles of Magnetic Resonance Imaging</b>	<b>5</b>
2.1	Nuclear Magnetic Resonance Physics . . . . .	6
2.2	Magnetic Resonance Imaging . . . . .	7
2.2.1	Spatial Encoding . . . . .	7
2.2.2	Spectral Encoding . . . . .	8
2.3	Non-Cartesian Imaging . . . . .	10
2.4	Accelerated Encoding . . . . .	12
2.4.1	Parallel Imaging . . . . .	12
2.4.2	Compressed Sensing . . . . .	14
2.4.3	Non-Cartesian Imaging with Parallel Imaging and Compressed Sensing	15
<b>3</b>	<b>Concentric Rings for Hyperpolarized <math>^{13}\text{C}</math> MR Spectroscopic Imaging</b>	<b>18</b>
3.1	Introduction . . . . .	18
3.2	Methods . . . . .	20
3.2.1	Concentric Rings Trajectory Design for MRSI . . . . .	20
3.2.2	Comparison of the Concentric Rings Trajectory with EPSI and Spiral	23
3.2.3	Experiment . . . . .	27
3.3	Results . . . . .	32
3.3.1	Theoretical Comparison of the Concentric Rings Trajectory with EPSI and Spiral . . . . .	32
3.3.2	Comparison of CRT, Spiral and EPSI on $^{13}\text{C}$ Phantom . . . . .	37
3.3.3	Hyperpolarized $^{13}\text{C}$ In Vivo Spectroscopic Imaging with Concentric Rings . . . . .	38
3.3.4	Comparison between Concentric Rings and EPSI with Hyperpolarized $^{13}\text{C}$ In Vivo . . . . .	40
3.3.5	Parallel Imaging with the Concentric Rings . . . . .	44
3.4	Discussion . . . . .	46
3.5	Conclusion . . . . .	47

<b>4</b>	<b>Motion Robust High Resolution Free-breathing Pulmonary Imaging</b>	<b>49</b>
4.1	Introduction . . . . .	49
4.2	Methods . . . . .	51
4.2.1	Data Acquisition . . . . .	51
4.2.2	Locally Low Rank Constraints for Respiration Motion Estimation . . . . .	53
4.2.3	Motion Compensated Reconstruction . . . . .	55
4.2.4	Experiments . . . . .	59
4.3	Results . . . . .	60
4.3.1	Evaluation of Dynamic 3D Self-Navigator . . . . .	60
4.3.2	Evaluation of Motion Compensated Image Reconstruction . . . . .	67
4.4	Discussion . . . . .	74
4.4.1	Dynamic 3D Self-navigator . . . . .	74
4.4.2	Soft-gating versus Respiratory Motion-resolved Method . . . . .	75
4.4.3	Feasibility in in Cystic Fibrosis and Pulmonary Nodules . . . . .	77
4.5	Conclusion . . . . .	79
<b>5</b>	<b>Estimation of Gradient Delays in non-Cartesian Parallel MRI</b>	<b>80</b>
5.1	Introduction . . . . .	80
5.2	Theory . . . . .	82
5.2.1	Low Rank Property in Parallel Imaging . . . . .	82
5.2.2	Solve for Gradient Timing Delays with Low Rank Constraints . . . . .	83
5.3	Methods . . . . .	88
5.3.1	Simulation Validation . . . . .	88
5.3.2	Phantom and In Vivo Experiments for Center-out Radial Trajectory . . . . .	89
5.3.3	In Vivo Experiments for Projection Reconstruction Trajectory and Spiral Trajectory . . . . .	90
5.4	Results . . . . .	91
5.4.1	Simulation Validation . . . . .	91
5.4.2	Phantom and In Vivo Experiments for Center-out Radial Trajectory . . . . .	94
5.4.3	In Vivo Experiments for Projection Reconstruction Trajectory . . . . .	95
5.4.4	In Vivo Experiments for Spiral Trajectory . . . . .	98
5.5	Discussion . . . . .	98
5.6	Conclusion . . . . .	100
<b>6</b>	<b>Summary of Contribution and Future Work</b>	<b>101</b>
6.1	Summary of Contribution . . . . .	101
6.2	Future Work . . . . .	102
	<b>Appendices</b>	<b>105</b>
	<b>References</b>	<b>109</b>

# List of Figures

2.1	Spin Polarization . . . . .	6
2.2	K-space and Image . . . . .	9
2.3	Common 2D Non-Cartesian K-space Trajectories . . . . .	11
2.4	Parallel Imaging Demonstration . . . . .	13
2.5	Incoherent Sampling Demonstration . . . . .	16
3.1	Pulse Sequence Design . . . . .	22
3.2	Common K-space Trajectories for Spectroscopic Imaging . . . . .	24
3.3	Comparison of Concentric rings, EPSI and Spiral Spectroscopic Imaging . . . . .	33
3.4	$^{13}\text{C}$ Phantom Study using CRT . . . . .	36
3.5	Comparison of $^{13}\text{C}$ Phantom Study using CRT, Spiral and EPSI . . . . .	37
3.6	In Vivo Results using CRT . . . . .	39
3.7	In Vivo Comparison using CRT and Symmetric EPSI . . . . .	41
3.8	In Vivo Results using CRT and Critical EPSI . . . . .	43
3.9	G-factor Simulation . . . . .	44
3.10	In Vivo Study with Parallel Imaging using CRT . . . . .	45
4.1	Pulse Sequence for Optimized 3D UTE . . . . .	52
4.2	Illustration of The Proposed Methods . . . . .	53
4.3	Dynamic 3D Self-navigator . . . . .	62
4.4	Different Respiration Estimation Methods Accuracy . . . . .	64
4.5	Comparison of Different Respiration Estimation on Two Patients . . . . .	66
4.6	Soft-gating L1-ESPIRiT Reconstruction . . . . .	68
4.7	Respiratory Motion-resolved L1-ESPIRiT Reconstruction . . . . .	69
4.8	Comparison of Soft-gating and Respiratory Motion-resolved on A Volunteer . . . . .	71
4.9	Comparison of Soft-gating and Respiratory Motion-resolved on A Patient . . . . .	73
4.10	Two Regularization Effects on Motion-resolved Reconstruction . . . . .	76
4.11	Feasibility in in Cystic Fibrosis and Pulmonary Nodules . . . . .	78
5.1	Illustration of The Proposed Method . . . . .	85
5.2	Simulation Results with The Proposed Method . . . . .	92

5.3	Simulation on Radial, Spiral and PR Trajectories . . . . .	93
5.4	Phantom and In Vivo Results using Center-out Radial Trajectory . . .	95
5.5	In Vivo Results using PR Trajectory . . . . .	97
5.6	In Vivo Result using Spiral Trajectory . . . . .	98
Appendix 1	EPSI Reconstruction . . . . .	106
Appendix 2	Matrix Inversion in EPSI Reconstruction . . . . .	107

# List of Tables

3.1	SNR comparison of CRT, Spiral and EPSI trajectories in a $^{13}\text{C}$ Phantom . . . .	38
5.1	Pseudo-code for Auto-calibration for Delays . . . . .	87

# Chapter 1

## Introduction

Magnetic resonance imaging (MRI) is a powerful non-invasive medical imaging modality. Unlike x-ray, computed tomography (CT) or positron emission tomography (PET), MRI provides a non-ionizing radiation solution to obtain superior soft-tissue contrast at high spatial resolution. The sensitivity to parameters and flexibility of MRI provide various types of soft tissue contrast, for example, oxygenation contrast for imaging brain activity, spectral contrast for mapping metabolites, blood flow information and more.

Imaging speed remains a major challenge for many MRI applications. Non-Cartesian imaging is a promising research direction for rapid MRI. Non-Cartesian trajectories can be designed to traverse k-space efficiently within hardware limits. Moreover, undersampling acceleration schemes of parallel imaging and compressed sensing often benefit from non-Cartesian trajectories. On one hand, non-Cartesian trajectories can better utilize spatial variation of coil sensitivities to reduce noise amplification of parallel imaging reconstruction. Commonly used non-Cartesian trajectories are oversampled in the center of k-space, thus enabling the use of auto-calibration parallel imaging methods. On the other hand, non-Cartesian trajectories can be designed to have fewer coherent artifacts from undersampling, thus fit better for compressed sensing theory compared with Cartesian trajectories.

In addition to increased imaging speed, non-Cartesian trajectories provide additional

benefits, which Cartesian trajectories cannot provide. For example, center-out radial trajectory is used for ultra-short echo time (UTE) acquisitions to capture signals from very short  $T2^*$  tissues [1]. Motion induced artifacts are less pronounced in radial and projection reconstruction (PR) trajectories [2, 3]. Also, radial and PR trajectories can be used to provide self-navigation for motion correction [4, 5, 6].

Despite these benefits shown in research developments, non-Cartesian imaging methods are not commonly used in clinical practice mainly because they are sensitive to errors from MR hardware imperfections, such as gradient delays or eddy currents. Image artifacts often arise from these corruptions, thus deteriorating diagnostic value for clinical evaluations. Hence, ensuring the robustness of non-Cartesian imaging to these hardware imperfections is essential for clinical applications.

This dissertation considers two particular applications that require rapid and robust imaging methods: hyperpolarized  $^{13}\text{C}$  MR spectroscopic imaging (MRSI) and pulmonary imaging. For hyperpolarized  $^{13}\text{C}$  MRSI, this dissertation proposes using concentric rings trajectory (CRT) as the image acquisition method. For pulmonary imaging, this dissertation proposes using 3D radial based ultrashort echo time (UTE) imaging sequence, combined with a novel reconstruction framework to provide motion robust high resolution 3D images in 5-minute free-breathing scans.

Despite developments of these non-Cartesian MRI methods, hardware imperfections are sometimes unavoidable, and result in apparent image artifacts for non-Cartesian trajectories. In the end, this dissertation describes a general approach to correct non-Cartesian k-space deviation, specifically caused by gradient timing delays, by exploiting data redundancy in multichannel datasets. This method is motivated by practical gradient delay problems occurred in the implementation of spiral, center-out radial trajectories in the previously mentioned methods.

## 1.1 Outline

The structure of this dissertation is as follows:

### **Chapter 2: Principles of Magnetic Resonance Imaging**

This chapter describes the principles of nuclear magnetic resonance and the concepts behind MR imaging. Non-Cartesian imaging and accelerated imaging methods (parallel imaging and compressed sensing) are also introduced to pertain to the rest of this dissertation.

### **Chapter 3: Concentric Rings for Hyperpolarized $^{13}\text{C}$ MRSI**

In vivo detection of  $^{13}\text{C}$  labeled substrates by MR spectroscopic imaging (MRSI) allows for observation of several key metabolic pathways, with promising applications in cancer and heart disease. In vivo  $^{13}\text{C}$  imaging is made possible by hyperpolarization. The short-lived hyperpolarized MR signal necessitates the need for rapid imaging acquisitions. This chapter introduces a rapid and robust MRI technique – concentric rings trajectory (CRT) for hyperpolarized  $^{13}\text{C}$  MRSI. Quantitative comparison analyses of CRT with Cartesian and spiral counterparts are performed. The motivation for parallel imaging extension is described and the first parallel imaging in vivo experiment for hyperpolarized  $^{13}\text{C}$  is demonstrated.

### **Chapter 4: Motion Robust High Resolution Free-breathing Pulmonary Imaging**

Pulmonary imaging has been a great challenge to MRI, because of combined factors of low proton density, respiratory motion as well as rapid  $T2^*$  signal decay. This chapter describes a 3D radial based UTE method for free-breathing pulmonary imaging. Methods including robust dynamic self-navigator to estimate respiratory motion and motion-compensated reconstructions are developed. Improved results in clinical patients are presented.

### **Chapter 5: Estimation of Gradient Delays in non-Cartesian Parallel MRI**

Gradient delays in non-Cartesian MRI not only induce spurious image artifacts but also



contaminate the auto-calibration region for parallel imaging. This chapter presents a novel and general method to correct for gradient timing delays in retrospect. It is based on the low-rank property of auto-calibration data in parallel imaging. The method is described and demonstrated with center-out radial, projection reconstruction and spiral trajectories.

## **Chapter 6: Summary and Future Work**

This chapter summarizes the improvements to non-Cartesian MRI presented in this dissertation and also outlines directions of future research based on these methods.

## Chapter 2

# Principles of Magnetic Resonance Imaging

Magnetic resonance imaging is based on the quantum mechanical phenomenon known as nuclear magnetic resonance (NMR). NMR is based on the fact that protons and neutrons have an intrinsic spin angular momentum, which was first observed by research groups led by Felix Bloch [7] and Edward Purcell [8] in 1945, and later applied to medical imaging by Paul Lauterbur in 1973 [9]. Magnetic resonance phenomenon often necessitates a quantum mechanical explanation whereas classical description is sufficient for understanding magnetic resonance [10]. This chapter only considers a classical description of magnetic resonance physics, and then briefly describes how the images are formed. Moreover, sophisticated encoding methods such as non-Cartesian imaging, parallel imaging and compressed sensing are also reviewed. A more complete description can be found in many popular textbooks [11, 12] and review papers [13, 14, 15].

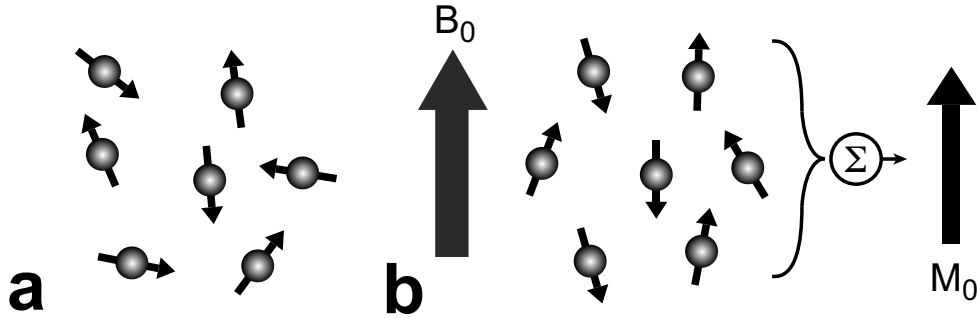


Figure 2.1: Effect of the external magnetic field on spins. (a) With no external field, the spins are randomly oriented. (b) Applying the external  $B_0$  field causes the spins to have a slight tendency to point along the direction of the field, resulting in a net magnetization,  $M_0$ .

## 2.1 Nuclear Magnetic Resonance Physics

Atoms with an odd number of protons/neutrons possess a property known as nuclear angular momentum (also known as spin). The hydrogen atom ( $^1\text{H}$ ) is most commonly used in NMR/MRI because it is the most abundant in the body. Several other atoms such as  $^{13}\text{C}$ ,  $^{31}\text{P}$  and  $^{23}\text{Na}$  also have nuclear angular momentum and therefore exhibit NMR phenomenon.

In the classical description, a strong static field  $B_0$  polarizes the spins, causing them to have a slight tendency to point along the direction of the field [10], thus generating a net magnetic moment  $M_0$  (simply referred as equilibrium magnetization) proportional to  $B_0$ .

Meanwhile, the spins resonate at a well-defined frequency, known as the Larmor frequency, which is proportional to the applied field:  $\omega_0 = \gamma B_0$ , where  $\gamma$  is gyromagnetic ratio. The spins absorb and also emit radio frequency (RF) signals at this particular resonance frequency.

The interaction of the magnetization  $\mathbf{M} = (M_x, M_y, M_z)$  with an external magnetic field  $\mathbf{B}$  ( $\mathbf{B}$  comprises the longitudinal and transverse components to the static magnetic fields) is governed by the Bloch equation:

$$\frac{d\mathbf{M}}{dt} = \mathbf{M} \times \gamma \mathbf{B} + \frac{M_0 - M_z}{T_1} + \frac{M_{xy}}{T_2}, \quad (2.1)$$

$M_{xy} = (M_x\vec{i} + M_y\vec{j})$  and  $M_z$  are defined as transverse and longitudinal magnetization, respectively. At thermal equilibrium,  $\mathbf{M} = (0, 0, M_0)$  aligns with  $\mathbf{B}$ . Applying a radio frequency excitation field  $B_1$  to the net magnetization tips  $\mathbf{M}$  and deviates it from the direction of  $\mathbf{B}$ , then precessional behaviors of the magnetization will occur.  $\mathbf{M}$  precesses about  $\mathbf{B}$  at the Larmor frequency and the transverse component  $M_{xy}$  leads to an electromotive force in a coil that is picked up as a signal.

Meanwhile, two types of relaxation mechanisms are occurring: longitudinal relaxation ( $T_1$  relaxation) and transverse relaxation ( $T_2$  relaxation). The relaxation mechanism will drive the magnetization to the equilibrium state  $\mathbf{M} = (0, 0, M_0)$ .  $T_1$  and  $T_2$  are constants specific to different materials and types of tissues.

## 2.2 Magnetic Resonance Imaging

The key components of magnetic resonance imaging are the interactions of three types of magnetic fields: (1) main homogenous, static magnetic field  $B_0$ , (2) transverse RF field  $B_1$  at Larmor frequency, and (3) spatially varying gradient field  $\mathbf{G}$ . In the presence of  $B_0$  field, the spins resonate and can be excited by RF magnetic fields  $B_1$ . Following this excitation, the precessing spins will produce RF signals, which can be detected. Spatially varying magnetic fields  $\mathbf{G}$  are used to spatially encode the transmitted and received RF signals, which allows for localization of magnetization signals.

### 2.2.1 Spatial Encoding

After the excitation,  $\mathbf{M}$  precesses about  $\mathbf{B}$  at the Larmor frequency, producing free induction decay signals, which are picked up by receiver coil. The received signal is a complex harmonic with a single frequency peak centered at the Larmor frequency.

Localization of the NMR signal  $m(x, y, z)$  is achieved with known spatially varying magnetic fields. This is most commonly introduced by applying superimposed linear magnetic

field gradients  $\mathbf{G} = (G_x, G_y, G_z)$  in the x, y, and z directions. The received signal is the contribution of all the precessing transverse magnetization of the whole volume (when ignoring relaxation):

$$\begin{aligned} S(t) &\propto \iiint m(x, y, z) \exp\left(-i\gamma \int_0^t \mathbf{G}(\tau) \cdot \mathbf{r} d\tau\right) dx dy dz \\ &\propto \iiint m(x, y, z) \exp[-i2\pi(k_x(t)x + k_y(t)y + k_z(t)z)] dx dy dz. \end{aligned} \quad (2.2)$$

where

$$\begin{aligned} k_x(t) &= \frac{\gamma}{2\pi} \int_0^t G_x(\tau) d\tau \\ k_y(t) &= \frac{\gamma}{2\pi} \int_0^t G_y(\tau) d\tau \\ k_z(t) &= \frac{\gamma}{2\pi} \int_0^t G_z(\tau) d\tau \end{aligned} \quad (2.3)$$

As Equation 2.2 shows, the acquired signal simply becomes the Fourier transform of  $m(x, y, z)$ . The spatial frequencies  $k_x, k_y, k_z$  are the time integrals of the gradient waveforms. The spatial frequency domain is usually called “k-space”. The image can be reconstructed with an inverse Fourier transform as the Fig 2.2 shows. Equation 2.2 is called *the signal equation*.

## 2.2.2 Spectral Encoding

So far, the signal equation ignores frequency shifts other than those induced by gradient encoding. In particular, chemical shifts describe subtle frequency shifts in the signal that are dependent on the chemical environment of particular compounds. They also provide the basis of NMR spectroscopy, which has been used to elucidate molecular structure.

In addition to spatial encoding, spectral encoding enables spectroscopic imaging methods that map the spatial distribution of components with different chemical shifts.

We add an additional variable to parameterize the dependence of NMR signal on the chemical shift species:  $m(x, y, z) \rightarrow m(x, y, z, f)$ . Then the signal equation becomes:

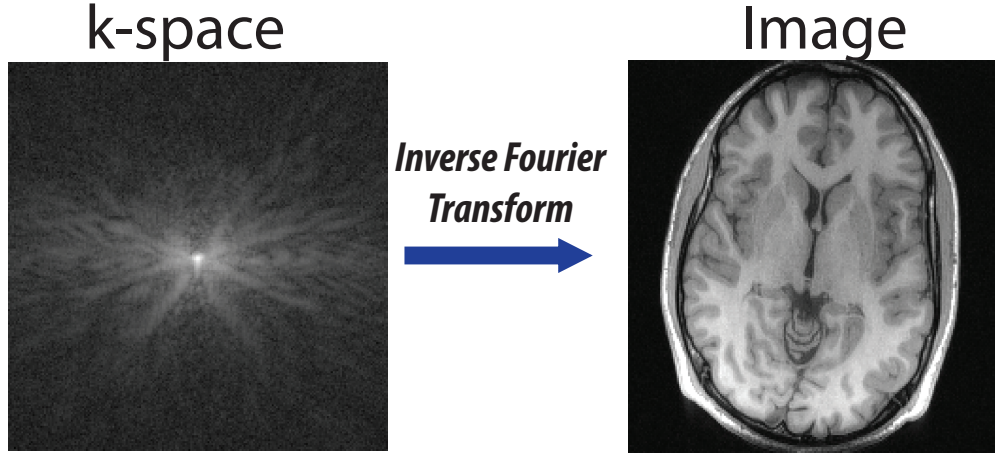


Figure 2.2: (left) acquired data (k-space) with logarithmic amplitude to enhance contrast; (right) reconstructed image via inverse Fourier transform.

$$\begin{aligned}
 S(t) &\propto \iiint\limits_{x,y,z} m(x, y, z, f) e^{-i2\pi k_x(t)x} e^{-i2\pi k_y(t)y} e^{-i2\pi k_z(t)z} e^{-i2\pi ft} dx dy dz df \\
 &\propto \iiint\limits_{x,y,z} m(x, y, z, f) e^{-i2\pi(k_x(t)x+k_y(t)y+k_z(t)z+ft)} dx dy dz df \\
 &\propto \iiint\limits_{x,y,z} m(x, y, z, f) e^{-i2\pi(k_x(t)x+k_y(t)y+k_z(t)z+k_f f)} dx dy dz df.
 \end{aligned} \tag{2.4}$$

where

$$\begin{aligned}
 k_x(t) &= \frac{\gamma}{2\pi} \int_0^t G_x(\tau) d\tau \\
 k_y(t) &= \frac{\gamma}{2\pi} \int_0^t G_y(\tau) d\tau \\
 k_z(t) &= \frac{\gamma}{2\pi} \int_0^t G_z(\tau) d\tau \\
 k_f &= t
 \end{aligned} \tag{2.5}$$

The k-space perspective of the signal equation now extends to a trajectory through the 4D Fourier transform of  $m(x, y, z, f)$  by denoting time as  $k_f$ . Equation 2.4 is called spectroscopic imaging signal equation. Magnetic resonance spectroscopic imaging can noninvasively

detect multiple small, endogenous molecular-weight metabolites, which is a promising tool for metabolic imaging.

## 2.3 Non-Cartesian Imaging

The most commonly used imaging method to acquire k-space data is sampling along rectilinear lines falling onto a Cartesian grid (top right of Fig 2.3). Reconstruction from such acquisitions is very simple: applying the inverse fast Fourier transform (FFT). In addition, reconstructions from Cartesian sampling are robust to many sources of system imperfections. For example, gradient delay translates to a benign linear phase in the image domain.

There are many other trajectories (non-equispaced encoding schemes) which do not fall into the Cartesian category, including sampling along spiral trajectories (Fig 2.3(a)), sampling along radial lines (Fig 2.3(b)), sampling along a set of concentric rings (Fig 2.3(c)), as well as a set of blades (known as PROPELLER [16] Fig 2.3(d)).

Special properties of these trajectories make them advantageous for specific applications. Spirals make efficient use of the gradient system hardware, and are used in rapid imaging applications, such as cardiac imaging [17] and fMRI [18]. PROPELLER trajectory [16] intrinsically was designed to correct motion. Radial and projection reconstruction (PR) acquisitions are less susceptible to motion artifacts than Cartesian trajectories [2], and can be significantly undersampled [19], especially for high contrast or sparse objects [17, 20, 21]. Radial/PR trajectories can also be used as self-navigation methods [4, 5, 6]. In addition, it is possible to capture fast relaxing compounds (tendons, bone, lung parenchyma) with radial or other center out (spiral, cones) trajectories [1, 22, 23].

For non-Cartesian encoding, the image reconstruction is more complicated. Since the data are acquired on a non-uniform grid, an inverse non-uniform discrete Fourier transform (NUDFT) is desired to reconstruct the underlying image. However, an exact inverse operation is not computationally efficient in practice, as it requires inversion of a large dense matrix. The most common method is to approximate the inverse NUDFT with the adjoint

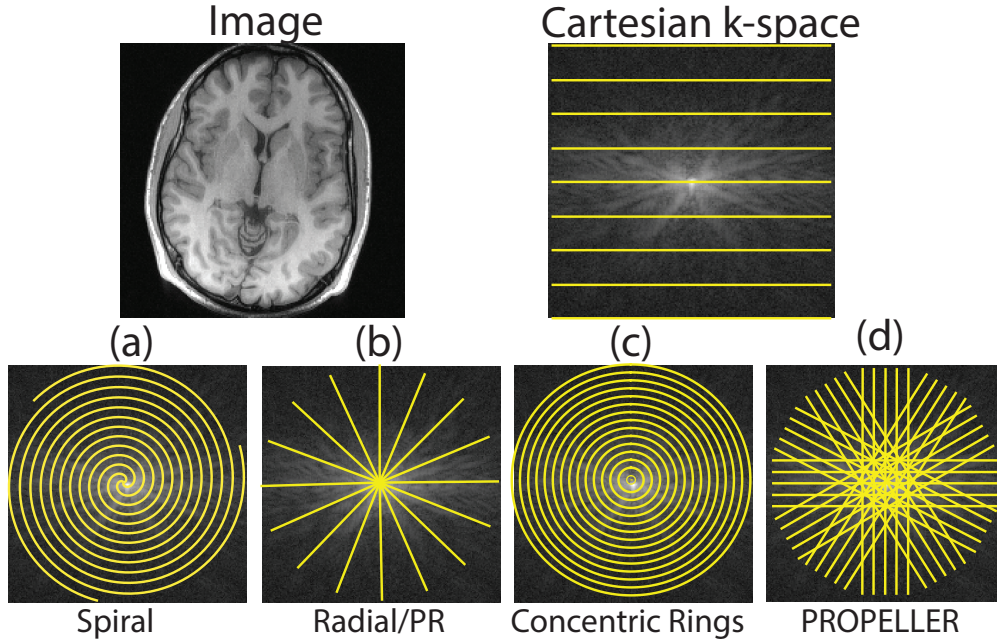


Figure 2.3: (top) Cartesian sampling of k-space and its reconstructed image; (bottom) some common 2D non-Cartesian k-space trajectories: spiral, radial/PR, concentric rings and PROPELLER.

non-uniform FFT (NUFFT) applied on density compensated data, also referred to as the gridding algorithm throughout this dissertation. The adjoint NUFFT operation is performed by convolving data with a finite kernel, sampling onto an oversampled uniform grid, performing an inverse FFT, and multiplying by a deapodization function. Adjoint NUFFT operations typically require density compensation, which compensate for the nonuniform sampling density, in order to approximate the inverse NUDFT. Alternatively, iterative reconstruction methods that use NUFFT, such as [24] can be performed without any density compensation. These methods use the forward and adjoint NUFFT operations iteratively to approximate the inverse NUDFT. More details about NUFFT can be found in [25, 26]. Throughout this dissertation, most of the reconstruction methods rely on NUFFT, combined with reconstruction of accelerated encoding, which is introduced in the following section.



## 2.4 Accelerated Encoding

Parallel imaging and compressed sensing are the two modern accelerated acquisition methods in MRI, providing scan time savings. Both methods provide acceleration through undersampling below the Nyquist rate: parallel imaging utilizes additional spatial encodings provided by multichannel coil arrays and compressed sensing exploits image sparsity. In this dissertation, I will exploit both sparsity and coil sensitivity information by solving an appropriate optimization problem.

### 2.4.1 Parallel Imaging

Parallel imaging based on local coil arrays with multiple receiver coils has been used to acquire MR imaging data with reduced scan time. These spatially localized coil arrays, reduce the recorded noise and increase the signal-to-noise ratio (SNR) [27]. Each coil element is sensitive to particular region of the entire object, so the image  $m(x, y, z)$  in the signal equation Equation 2.2 becomes  $S_j(x, y, z)m(x, y, z)$  where  $S_j(x, y, z)$  is the spatial sensitivity of the receiver element  $j$ . I call  $S_j(x, y, z)$  sensitivity maps in this dissertation.

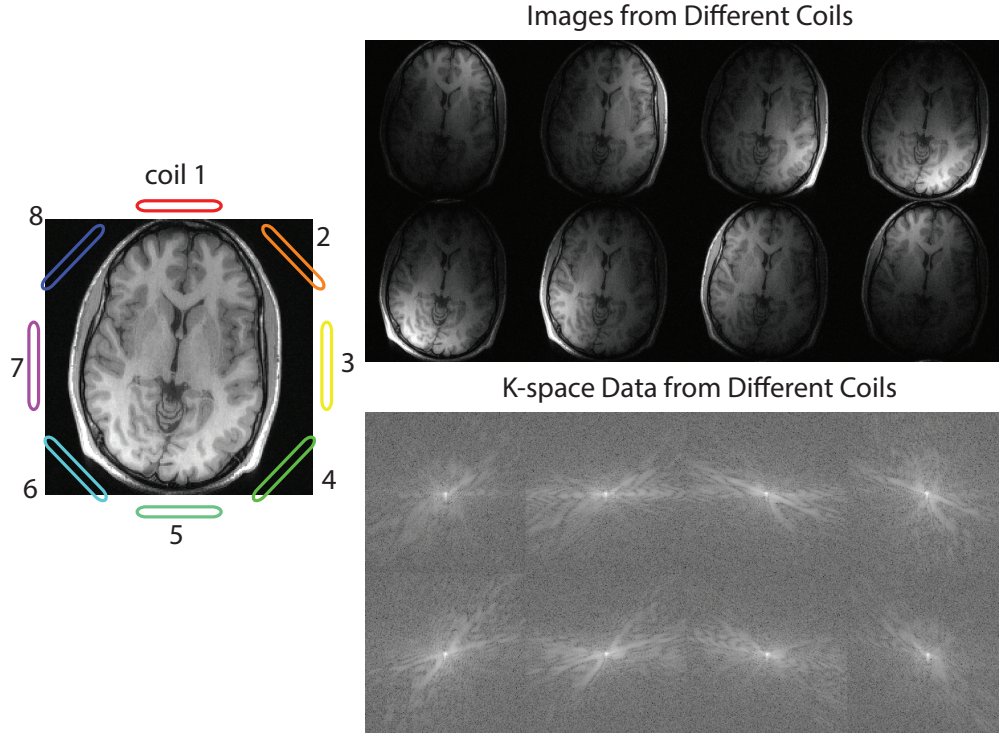


Figure 2.4: (top) Images from different receiver coils; (bottom) k-space data from different coils displayed with logarithmic scale for enhancement.

Parallel imaging achieves acquisition acceleration by acquiring a reduced amount of k-space data [13]. While undersampling below Nyquist rate in k-space induces image aliasing, multiple receiver coils provide additional encoding (as Fig 2.4 shows): in the image domain, the underlying images are superimposed with coil sensitivities, thus the acquired k-space data is correlated with coil sensitivities. In parallel imaging, the discretized signal equation can be simplified as the following:

$$y = PFSm \quad (2.6)$$

where  $y$  is the acquired k-space data,  $P$  is the undersampling operator,  $F$  is the Fourier transform operator,  $S$  represents the coil sensitivities, and  $m$  is the target image. Image  $m$  can be determined by solving the following optimization problem:

$$\operatorname{argmin}_m \|y - PFSm\|_2^2 \quad (2.7)$$

Many algorithms [28, 29, 30, 31] have been developed to resolve the image from the acquired undersampled data. Among them, SENSE [28] is a general and explicit method that is compatible with arbitrary k-space trajectories (known as CG SENSE [32] for non-Cartesian) with the knowledge of sensitivity maps. For Cartesian sampled parallel imaging, there exists closed-form solutions to resolve the images. However, for non-Cartesian parallel imaging, all voxels are coupled in the reconstruction. Hence an explicit inversion is not feasible computationally. Instead, iterative algorithms provide an efficient alternative.

Although undersampling in parallel imaging accelerates data acquisition, it sacrifices SNR. This is because SNR is proportional to the square root of the acquisition time. As the scan time is reduced, the SNR is lower compared to the fully sampled case. In addition, if we regard image reconstruction as an inverse problem, undersampling pattern could make the problem ill conditioned. That results in higher condition number, which is called geometric factor (g-factor) in MRI [28]. G-factor depends on the coil geometry, undersampling pattern, as well as the k-space trajectories. Chapter 3 elaborates on the g-factor analysis with different trajectories.

## 2.4.2 Compressed Sensing

Natural images, including medical images, are compressible by many-fold. One such example is the popular JPEG compression. Compressed sensing implicitly compresses data within the signal acquisition process by obtaining fewer so-called incoherent measurements and then reconstructing the underlying images with iterative methods.

There are three key components for the application of compressed sensing in MRI: (1) medical images are naturally compressible by sparse coding in an appropriate transform domain (*e.g.*, by wavelet transform); (2) MRI scanners naturally acquire encoded samples,

rather than direct pixel samples (*e.g.*, spatial encoding), which allows for incoherent sampling; (3) sparsity enforcing reconstruction.

In order to generate incoherent measurements, compressed sensing requires pseudo random undersampling pattern, as shown in Fig 2.5. Incoherent measurements create incoherent artifacts in the image domain, which can be resolved using sparsity enforcing reconstruction methods. To enforce sparsity in reconstruction, compressed sensing needs to add sparsity promoting regularization, such as  $\ell_1$  regularization, to the reconstruction equation (Equation 2.7):

$$\underset{m}{\operatorname{argmin}} \quad \frac{1}{2} \|y - P F m\|_2^2 + \lambda \|\Phi m\|_1 \quad (2.8)$$

Here,  $y$  is the acquired k-space data,  $P$  is the undersampling operator,  $F$  is the Fourier transform operator, and  $m$  is the target image,  $\Phi$  is a sparsifying transform. The first term of the Equation 2.8 enforces the data consistency of the measurement, and the second term constrains the transform sparsity of the underlying image.

Since the optimization problem is not linear, iterative methods such as proximal gradient descent methods are required to solve the optimization problem [33]. More details about compressed sensing in MRI application are elaborated in the work [15, 34].

### 2.4.3 Non-Cartesian Imaging with Parallel Imaging and Compressed Sensing

Compressed sensing and parallel imaging can be combined with non-Cartesian imaging for highly undersampled data acquisitions. Non-Cartesian parallel imaging offers several potential advantages over Cartesian approaches. Many non-Cartesian trajectories are fully sampled/oversampled in the center of k-space, which allows for the use of auto-calibration parallel imaging methods. Also, the g-factor can be reduced by using non-Cartesian trajectories. The better conditioning of the reconstruction is because acceleration is divided in multiple directions in non-Cartesian imaging, whereas acceleration is performed in one di-

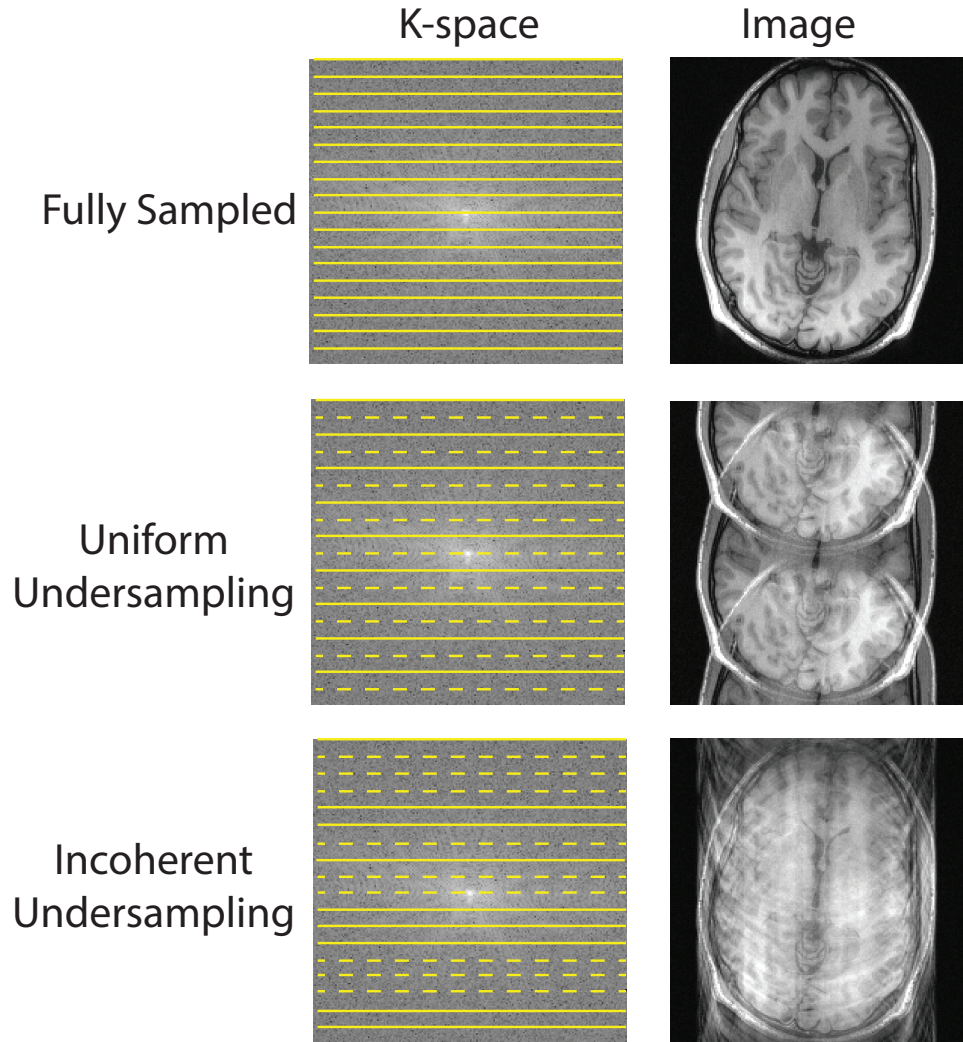


Figure 2.5: Conceptual illustration of images and k-space sampling pattern for fully sampled, uniform undersampled and incoherent undersampled scenarios.

rection (the phase encoding direction) in Cartesian imaging [14]. Non-Cartesian acquisitions can better utilize the multi-dimensional spatial variation of the coils sensitivities to improve the conditioning of reconstruction.

In some applications, especially dynamic imaging, additional acceleration beyond the number of coil arrays is necessary. Hence, the incorporation of compressed sensing to exploit image sparsity provides crucial acquisition acceleration. To incorporate compressed sensing

with non-Cartesian imaging, trajectories should be designed to induce incoherent aliasing. One such example is the golden-angle radial trajectory [35]. Similar to parallel imaging, non-Cartesian trajectories can often be designed such that undersampling induces less coherent image aliasing than Cartesian trajectories, because they can spread artifacts across multiple dimensions. Thus, non-Cartesian compressed sensing has great potential and may be even more advantageous than Cartesian for specific applications.

In this dissertation, I incorporate parallel imaging and compressed sensing into two particular applications that require rapid imaging methods: hyperpolarized  $^{13}\text{C}$  MR spectroscopic imaging (MRSI) and pulmonary imaging. In particular, Chapter 3 demonstrates parallel imaging applications in hyperpolarized  $^{13}\text{C}$  spectroscopic imaging using concentric rings trajectory and demonstrates the improved conditioning of parallel imaging with concentric rings trajectory compared to its Cartesian counterpart. Chapter 4 of this dissertation demonstrates promising parallel imaging and compressed sensing applications using 3D radial trajectory for motion resolved pulmonary imaging.

## Chapter 3

# Concentric Rings for Hyperpolarized $^{13}\text{C}$ MR Spectroscopic Imaging

### 3.1 Introduction

In contrast to anatomic MRI, which detects changes in the relaxivity or density of bulk tissue water, magnetic resonance spectroscopic imaging (MRSI) can noninvasively detect multiple small, endogenous molecular-weight metabolites within cells or extracellular spaces.

In vivo detection of  $^{13}\text{C}$  labeled substrates by MRSI allows for observation of specific enzyme-catalyzed reactions that reflect altered metabolism in cancer [36]. This was recently made possible by creating hyperpolarized nuclear spins in the liquid state suitable for injection through a process called dissolution dynamic nuclear polarization (DNP). This process greatly improves the signal sensitivity by a factor of 10,000+ [37], thereby allowing the direct monitoring of  $^{13}\text{C}$  metabolites in vivo as long as the data acquisition is fast enough to capture the short-lived signal ( $\leq 1\text{min}$ ). The first phase I clinical trial using this technology was recently performed in the Surbeck Laboratory of Advanced Imaging at UCSF, where 31 prostate cancer patients were studied using hyperpolarized  $^{13}\text{C}$  MRI. The study showed no adverse effect and demonstrated promising initial imaging results for detecting and staging

tumors [38].

Despite these advances, the short-lived effect of hyperpolarization still poses severe challenges for imaging. It is therefore necessary to develop rapid and robust imaging techniques. Furthermore, these techniques must also resolve metabolite signals at multiple resonance frequencies. Techniques have been developed that rely on fast spectroscopic sequences that exploit the most out of the system hardware [39, 40, 41, 42, 43, 44, 45, 46], imaging-based sequences with spectral separation techniques [47, 48, 49], parallel imaging using coil arrays [50, 51, 52], and exploiting structure and redundancy in the data [53, 54, 55].

Fast spectroscopic sequences are advantageous because they provide comprehensive spectral information about all metabolites. This is especially important when using multiple hyperpolarized agents [56] or agents with more complex spectra such as [1,2- $^{13}\text{C}$ ] pyruvate [57], which presents major design challenges for imaging-based sequences [47, 48, 49]. In comparison to these sequences, fast spectroscopic sequences are also more robust to  $B_0$  inhomogeneities.

Currently, both Cartesian (Echo-Planar Spectroscopic Imaging or EPSI [39, 40, 58]) and non-Cartesian (spiral [42, 43, 59] and radial [41] spectroscopic imaging) techniques have been investigated for accelerated hyperpolarized  $^{13}\text{C}$  MRSI. EPSI uses bipolar trapezoid magnetic field gradients during signal detection and offers larger k-space coverage. However it suffers from relatively long scan times due to the number of phase encodings. In addition, minor system imperfections can induce undesirable ghosting artifacts. To prevent ghosting, flyback EPSI can be used but at the expense of a more limited spectral bandwidth (SBW). This limits the number of metabolites that can be observed without aliasing. Spiral spectroscopic imaging is an alternative that provides a scan-time-efficient imaging scheme, but it is susceptible to system imperfections (such as gradient timing delay and eddy currents) [60].

To provide scan-time-efficiency and robustness to system imperfections, I propose using concentric rings trajectory (CRT) as the data acquisition method for  $^{13}\text{C}$  MRSI. It has the following advantages: I. the acquisition time is halved compared with EPSI, given the same imaging prescriptions; II. the slew rate (a hardware limitation for magnetic field gradients)



requirement is less demanding than the time-optimal spiral trajectory; III. CRT is robust to first order eddy currents and system delays; IV. this sampling trajectory results in lower g-factor noise amplification in parallel imaging than EPSI. CRT for MRI was first proposed by Wu *et al.* [61, 62]. They implemented CRT on magnetization-prepared imaging and corrected for the off-resonance blurring by retracing the central k-space. They also analyzed the unique contrast and robustness properties of CRT. Later, Kwon *et al.* [63] implemented the concentric cylinders trajectory on 3D magnetization-prepared imaging. In their study, Kwon *et al.* demonstrated the feasibility of the 3D concentric cylinder for magnetization-prepared imaging.

In another recent work, Furuyama *et al.* [64] implemented CRT in a standard PRESS based spectroscopy sequence for proton MRSI. They demonstrated feasibility in the healthy human brain *in vivo*, taking advantage of the trajectory robustness and two-fold acceleration over EPSI. Quantitative comparisons between CRT and other MRSI trajectories to evaluate resolution, spectral bandwidth and SNR efficiency, have not been reported yet. Moreover, for the hyperpolarized  $^{13}\text{C}$  MRSI application, some practical challenges and unique properties which are well-suited to CRT have not been exploited yet.

In this chapter, I demonstrated the efficacy of CRT through a quantitative comparison between CRT, EPSI and spiral MRSI, and used a  $^{13}\text{C}$  MRSI CRT sequence for  $^{13}\text{C}$  phantom and hyperpolarized  $^{13}\text{C}$  *in vivo* animal applications. I also extended the application of CRT to parallel imaging for additional acceleration and analyzed noise amplification compared with Cartesian counterpart.

## 3.2 Methods

### 3.2.1 Concentric Rings Trajectory Design for MRSI

CRT for MRSI is derived similarly as in [61, 62]. Gradients are designed for the outermost ring with respect to the spatial resolution and spectral bandwidth (SBW) and then scaled

down for the inner rings with the readout window  $T_{\text{readout}}$  kept constant. I use CRT with constant angular velocity since they are robust to timing and eddy currents delays. The radius of the outermost ring is set according to the desired spatial resolution. Maximum gradient amplitude and slew rates set an upper limit on the achievable spectral bandwidth, which is determined by the retracing period  $\Delta T$ . The number of rings  $N_{\text{ring}}$  determines the in-plane field of view (FOV), whereas the number of revolutions  $N_{\text{rev}}$  determines the spectral resolution – which is ultimately limited by  $T2^*$  decay.

The prewinders and rewinders are designed using the time-optimal gradient design by Hargreaves *et al.* [65] and implemented in Matlab (The Mathworks, Natick, MA, USA.) and the CVX [66] convex optimization toolbox. The trajectory for an axial plane is shown in Fig 3.1.

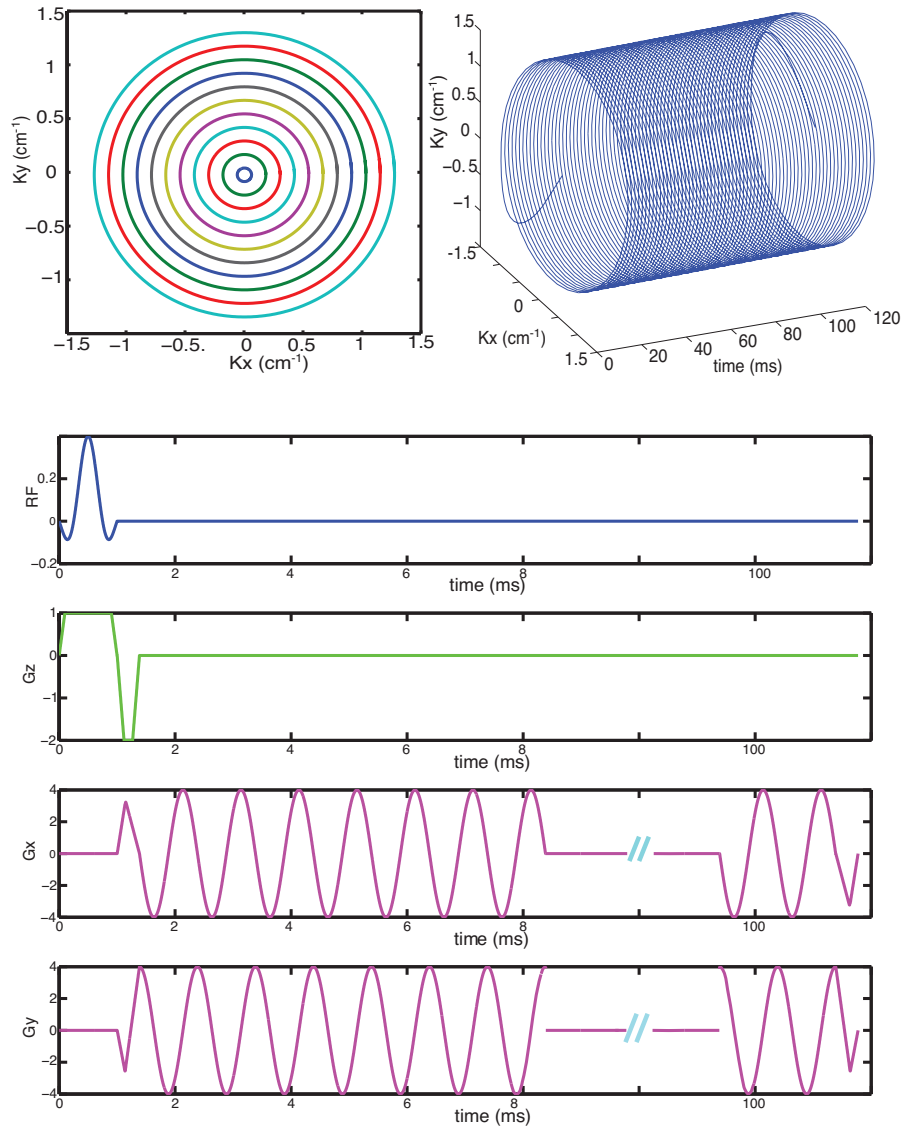


Figure 3.1: Concentric rings trajectory and sequence design: top-left shows the spatial concentric rings k-space trajectory; top-right shows the spatial-spectral k-space trajectory; bottom shows the concentric rings GRE sequence for axial images.

The constant angular velocity of rings is insensitive to some system imperfections. Timing and first-order eddy currents induced delays result in benign rotations of images [62, 63]

rather than spatial blurring.

### 3.2.2 Comparison of the Concentric Rings Trajectory with EPSI and Spiral

For MRSI sequences, especially in hyperpolarized studies, optimizing the total scan time, spectral bandwidth, and SNR is crucial for capturing the intrinsic contrast and biochemical information. A quantitative study of CRT using these key parameters was performed in order to compare against three other commonly used MRSI schemes: EPSI (both symmetric and flyback EPSI) and spiral spectroscopic trajectories. Fig 3.2 illustrates the k-space trajectories for the different methods. In symmetric EPSI, k-space is scanned in a zigzag trajectory and is collected in both directions (blue and yellow arrows in the symmetric EPSI in Fig 3.2). In the analysis I compare against a design in which the spectral bandwidth is determined by the time between scans in the same direction, such as the duration between adjacent blue arrows. This guarantees Nyquist sampling of the spectrum and is the preferred method in our institute. I refer to this approach as Nyquist-constrained symmetric EPSI [40]. However, it is possible to exploit Papoulis’s generalized sampling theory [67] and double the spectral bandwidth of the current symmetric design, as it was initially implemented in proton MRSI [68]. In this situation the spectral bandwidth is defined by the time between alternate scanning directions, such as the duration between adjacent blue and yellow arrows. This dissertation refers to this approach as “critical symmetric EPSI”. I elaborate on the reconstruction method of this approach in the Appendix section.

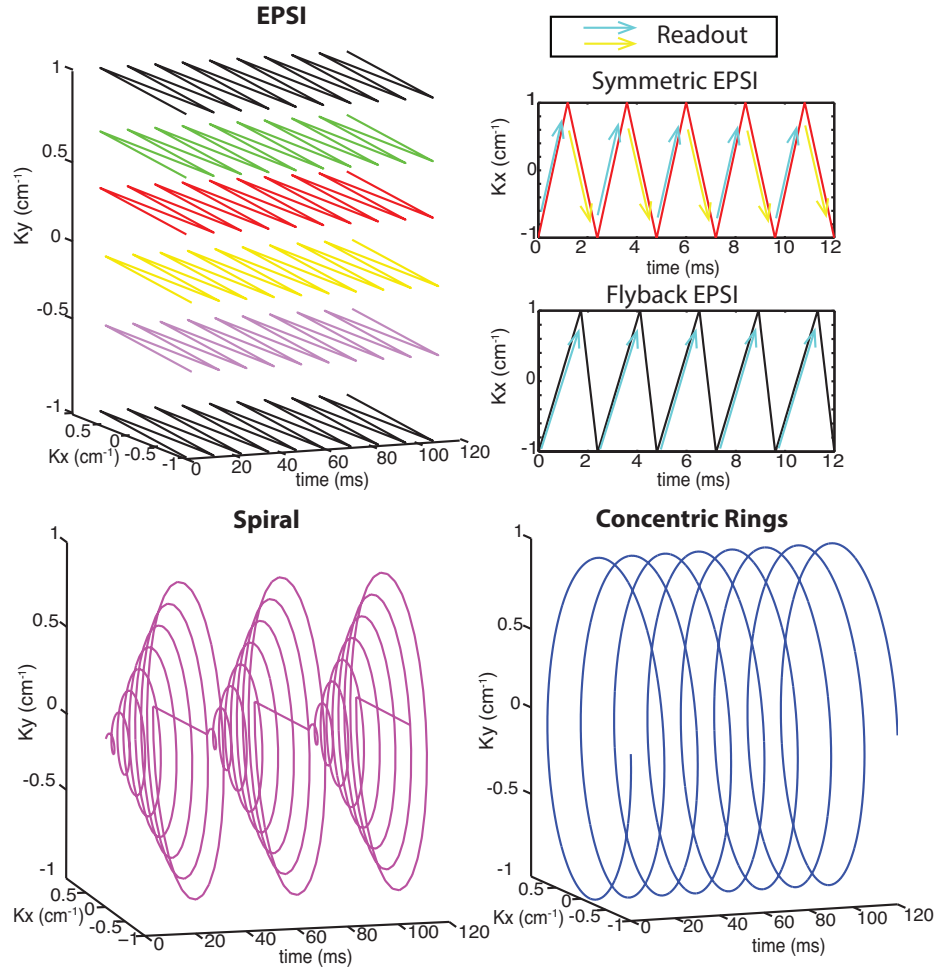


Figure 3.2: K-space trajectories of EPISI, spiral and concentric rings spectroscopic imaging; the arrows illustrates the readout directions for both symmetric EPISI and flyback EPISI; for symmetric EPISI, I use different-colored arrows to differentiate the odd/even echoes for reconstruction.

For a fair comparison, I fixed some specific prescriptions when evaluating acquisition time, SBW and SNR efficiency with respect to the spatial resolution. The parameter ranges were chosen according to typical routine hyperpolarized preclinical prescriptions for  $[1-^{13}\text{C}]$ pyruvate that were performed in our institute:  $\text{FOV} = 16 \times 16 \text{ cm}^2$  Here, I need to

mention that CRT and spiral have circular FOV while EPSI has a square FOV, so they are not exactly identical. I defined the extent of imaging support along the x and y axes to be the FOV), spectral resolution = 10 Hz (*i.e.*, the readout window  $T_{\text{readout}} = 100$  ms), spatial resolution was in the range from 0.36 cm to 1 cm. All designs assumed a gradient amplitude limit of 40 mT/m and maximum slew rate of 150 mT/m/ms.

### Acquisition Time Comparison

The acquisition time should be as short as possible to “freeze” the  $^{13}\text{C}$  signal while hyperpolarized compounds undergo metabolic conversion and before they decay back to equilibrium. In order to compare acquisition time, I fixed the SBW = 500 Hz, TR = 200 ms, spectral resolution = 10 Hz and FOV =  $16 \times 16$  cm<sup>2</sup>. The total acquisition time  $T_{\text{acquisition time}}$  is simply the product of TR, the number of phase encodings  $N_{\text{pe}}$  and the number of interleaves in time  $N_{\text{interleaves}}$ .

$$T_{\text{acquisition time}} = TR \times N_{\text{pe}} \times N_{\text{interleaves}} \quad (3.1)$$

### SNR Efficiency Comparison

In the SNR efficiency comparisons, the following parameters are fixed: SBW = 500 Hz, spectral resolution = 10 Hz and FOV =  $16 \times 16$  cm<sup>2</sup>. I considered the duty cycle and the k-space sampling uniformity effects on SNR efficiency. (I did not consider T1 effects and the number of excitations. Unlike conventional imaging, hyperpolarized  $^{13}\text{C}$  imaging often uses a progressive flip angle [69], which equalizes the magnetization for each excitation. This results in an SNR that is independent of the number of excitations and this is elaborated in the Parallel Imaging with Concentric Rings section. Since relatively small number of excitations was considered here, T1 effects could be neglected. When the acquisition is long, T1 decay during the scan will reduce the available magnetization. It is worth mentioning that spirals and rings will have the advantage over EPSI since they require fewer acquisitions.)

SNR efficiency depends on the duty cycle:

$$SNR_{\text{eff,duty}} = \sqrt{\frac{T_{\text{active time}}}{T_{\text{readout}}}}, \quad (3.2)$$

where  $T_{\text{active time}}$  is the total duration of the active readout gradients while  $T_{\text{readout}}$  is the duration of readout window.

It is also dependent on the uniformity of the sampling trajectory. Non-uniform sampling acquisitions are less SNR efficient than uniform ones. This was nicely demonstrated in [70], where the effective SNR efficiency is given by:

$$SNR_{\text{eff,uniformity}} = \frac{A_k}{\int_{\vec{k}} D(\vec{k}) d\vec{k} \int_{\vec{k}} \frac{1}{D(\vec{k})} d\vec{k}}, \quad (3.3)$$

where  $D(\vec{k})$  is the density of the corresponding sampling position, and  $A_k$  is the k-space coverage.

I defined the overall SNR efficiency to be the product of the above two formulas and computed the SNR efficiency for different trajectories.

For flyback and symmetric EPSI, it was required to use ramp sampling (as otherwise the SBW requirement was not achievable). For the spiral trajectory, I designed time-optimal spiral trajectories for different imaging resolution in order to minimize the total acquisition time, which was essential for hyperpolarized  $^{13}\text{C}$  imaging.

## Spectral Bandwidth

Spectral bandwidth (SBW) relates to the number of metabolites I can observe without spectral aliasing. For example, in hyperpolarized  $[1-^{13}\text{C}]$ pyruvate studies at 3T, 500 Hz SBW is a reasonable range to observe the pyruvate and its products,  $[1-^{13}\text{C}]$ lactate and  $[1-^{13}\text{C}]$ alanine. Here I fixed spectral resolution = 10 Hz and FOV =  $16 \times 16 \text{ cm}^2$ . SBW is determined by  $\Delta T$ , which is the retracing period (in Equation 3.4) to the same k-space position.

$$SBW = \frac{1}{\Delta T} \quad (3.4)$$

### 3.2.3 Experiment

All the phantom and in vivo studies were conducted on a 3.0 T GE clinical scanner (GE Healthcare, Waukesha, WI, USA.) with maximum gradient amplitude of 40 mT/m and maximum slew rate of 150 mT/m/ms. All the animal studies conducted were approved by the Institutional Animal Care and Use Committee (IACUC).

#### Sequence Design Parameters for Concentric Rings Trajectory

CRT was implemented into the readout window of a 2D gradient echo (GRE) slice-selective pulse sequence. The spectroscopic imaging module consisted of readout window duration  $T_{\text{readout}} = 100$  ms, corresponding to a nominal spectral resolution of  $\Delta f = 10$  Hz, and a SBW = 500 Hz, which set the duration of each revolution to  $\Delta T = 2$  ms. The achievable in-plane isotropic spatial resolution was 3.67 mm, which was limited by the slew rate and by the SBW. For the  $^{13}\text{C}$  phantom study, the flip angle (FA) was set to be constant for each excitation. In the hyperpolarized studies, a progressive flip angle technique [69] was applied in order to equalize the signal across excitations. Temporal interleaves were implemented by appropriate delay of the readout trajectory in order to increase spectral bandwidth.

#### $^{13}\text{C}$ Phantom Spectroscopic Imaging Comparison

In order to evaluate the feasibility of CRT, I carried out comparison studies between CRT, spiral, and EPSI trajectories based on the similar prescriptions. A 4-compartment phantom for Carbon-13 was used, which included 1.0 M  $^{13}\text{C}$  bicarbonate, 2.0 M  $^{13}\text{C}$  formate, 1.0 M  $[1-^{13}\text{C}]\text{lactate}$ , and 1.0 M  $[1-^{13}\text{C}]\text{alanine}$ . For localization, T2-weighted  $^1\text{H}$  anatomic MR images were acquired in sagittal, axial, and coronal views. CRT sequence was used with the basic prescriptions: FOV =  $8 \times 8$  cm<sup>2</sup>, resolution =  $3.67 \times 3.67$  mm<sup>2</sup>, TE/TR = 3.4 ms/ 5 s, SBW = 500 Hz, FA = 90 °, readout window  $T_{\text{readout}} = 100$  ms, and 11 rings were encoded. TR = 5 s was used for the full T1 relaxation of the  $^{13}\text{C}$  components in the phantom. Since



metabolites resonance range was about 700 Hz at 3.0 T, I did temporal interleaving to double the SBW from 500 Hz into 1000 Hz. The total scan time was  $1\text{min } 50\text{ s} = 5\text{ s (TR)} \times 11$  (number of phase encoding rings)  $\times 2$  (interleaves).

I designed a symmetric EPSI trajectory (Nyquist-constrained) counterpart and a time-optimal spiral spectroscopic trajectory counterpart, which were implemented in the same pulse sequence scheme with CRT. Owing to the same prescriptions of 3.67 mm resolution and SBW = 500Hz, the symmetric EPSI trajectory was designed to have 50 odd echoes and 50 even echoes, including ramp sampling. It needs twice the number of excitations as the CRT to cover the same FOV. As for spiral spectroscopic trajectory with respect of the design of  $8 \times 8\text{ cm}^2$  FOV and 3.67 mm isotropic resolution prescription, it only had 7 echoes in each TR, given the readout window duration, thus this single-shot spiral had the SBW = 68.6 Hz. In order to have comparable SBW with CRT and EPSI, spiral trajectory required multiple temporal interleaves.

The same 4-compartment phantom for Carbon-13 was used in the comparison studies. TE/TR = 3 ms/ 5 s was used for all the trajectories. The symmetric EPSI trajectory required 22 excitations and one temporal interleave to have comparable 1000 Hz SBW. For each readout, the data was separated into 50 odd echoes and 50 even echoes, and then reconstructed by 3D gridding to be two  $22 \times 22 \times 50$  matrices. The spiral trajectory required additional 14 interleaves to have 1000 Hz SBW. The raw data was 3D gridded into a  $22 \times 22 \times 50$  matrix. The total scan time was  $1\text{ min } 50\text{ s} = 5\text{ s (TR)} \times 11$  (number of phase encoding rings)  $\times 2$  (interleaves) for CRT,  $3\text{ min } 40\text{ s} = 5\text{ s (TR)} \times 22$  (number of phase encoding rings)  $\times 2$  (interleaves) for EPSI and  $1\text{ min } 15\text{ s} = 5\text{ s (TR)} \times 15$  (interleaves) for spiral.

### **Hyperpolarized $^{13}\text{C}$ in vivo Spectroscopic Imaging**

In vivo experiments were performed on normal Sprague-Dawley strain rats, with weight about 500 g. For all the rats, a tail vein catheter was placed immediately before the hy-

perpolarized MR study. Next, the isoflurane anesthetized rats were placed on a water-filled, temperature-controlled pad that was heated to approximately 37 C° and positioned inside of the coil. The respiration and heart rate of the rats were monitored during the experiments. Initially, T2-weighted <sup>1</sup>H anatomic MR images were acquired in sagittal, axial, and coronal views. The subsequent hyperpolarized <sup>13</sup>C scans were prescribed on the chosen slices. A mixture of [1-<sup>13</sup>C] pyruvic acid and the trityl radical (tris methyl sodium salt; GE Healthcare) was polarized using the HyperSense polarizer (Oxford Instruments, Oxford, UK.). After the mixture was polarized, it was rapidly dissolved into a pH-balanced Tris buffer solution, targeting a hyperpolarized 100 mmol/L pyruvate solution with a neutral pH. Next, the solution was quickly transported to the MR scanner and 2.2 mL was injected into the rat over 12 s. The imaging data acquisition was initiated 30 s after the start of the pyruvate injection to coincide with the peak lactate signal. A slice-selective pulse sequence with a progressive flip angle excitation pulse using CRT was performed using a TE/TR = 3.4/200 ms, readout window T<sub>readout</sub> = 100 ms, and 11 rings. Additional sequence prescriptions for rat studies included: FOV= 8×8 cm<sup>2</sup>, slice thickness of 10 mm, resolution = 3.67×3.67 mm<sup>2</sup>, and 500 Hz SBW. The total scan time was 2.2 s. For this study, the total scan time could be reduced by 35% by decreasing TR. I carried out in vivo comparison studies between CRT and EPSIs: both the comparison of CRT with Nyquist-constrained symmetric EPSI and the comparison between CRT and critical EPSI. TE/TR = 3.4/250 ms was used for CRT while for the EPSI counterparts, TE/TR = 3.4/200 ms was used.

### **Parallel Imaging with Concentric Rings**

Parallel imaging is favorable for hyperpolarized <sup>13</sup>C imaging because the shorter scan time reduces SNR losses due to T1 decay and metabolism during the acquisition, especially in larger, human-sized FOV 2D MRSI or 3D MRSI applications that require large numbers of encoding steps. In non-hyperpolarized imaging, undersampling of k-space in parallel imaging

reduces the acquisition time but at the trade-off of losing SNR, as Equation 3.5 shows: [28]

$$SNR_{und} = \frac{SNR_{full}}{g\sqrt{R}}. \quad (3.5)$$

$SNR_{und}$  and  $SNR_{full}$  are the undersampled and fully sampled SNR respectively, and  $R$  is the acceleration factor. The g-factor,  $g$ , is spatially variant noise enhancement that depends on the receiver coil array and sampling pattern.

However, the inherent signal of hyperpolarized  $^{13}\text{C}$  imaging is limited. With undersampling, the given amount of total magnetization can be distributed into fewer excitations where each excitation has more signal. In fact, reduced acquisition time may translate into higher image SNR due to the reduced T1 relaxation [50]. As a result, parallel imaging does not result in losing inherent signal if a progressive flip angle [69] is applied (shown in Equation 3.6). This results in an undersampled SNR as

$$SNR_{und} = \frac{SNR_{full}}{g}. \quad (3.6)$$

### Simulation of G-factor

Given the same phase-array coil sensitivity, the g-factor is determined by the sampling pattern. A Monte-Carlo technique, which is also known as pseudo replica method [71], was used to calculate g-factor maps of a simulated 8-channel phased-array coil and 4-fold undersampling with CRT and rectilinear Cartesian (*i.e.*, EPSI) trajectories. Fully encoded series of images with identical parameters were simulated. Out of this image series, an  $SNR_{full}$  map of the fully encoded image can be derived by taking the mean and the standard deviation on a pixel-by-pixel basis throughout the image series. Undersampling was achieved by uniformly skipping phase encodings for both CRT and Cartesian counterparts. Similarly, after reconstruction an  $SNR_{und}$  map of undersampled encoded image was generated and a g-factor map was computed by the Equation 3.5.

The simulated g-factor maps were  $256 \times 256$  and cropped to display circular FOV. CRT's g-factor maps were generated by using fully sampled 128 rings and undersampled 32 rings respectively, while the Cartesian (EPSI) g-factor map was generated by fully sampled 256

phase encodings and undersampled 64 phase encodings. I used conjugate gradient SENSE (CG-SENSE) [32] without regularization for the reconstruction. The number of pseudo replicas was 50 for both sampling patterns.

### **Parallel Imaging for Hyperpolarized $^{13}\text{C}$ in vivo Spectroscopic Imaging**

To evaluate the feasibility of parallel imaging using CRT, a hyperpolarized in vivo experiment was performed on normal Sprague-Dawley strain rats. An 8-channel  $^{13}\text{C}$  phased-array rat coil was constructed especially for the study with the coils distributed isotropically around the animal in the axial plane. I redesigned the CRT sequence to have a 420 Hz SBW as a tradeoff for finer spatial resolution, and 10 Hz nominal spectral resolution. A slice-selective pulse sequence with a progressive flip angle excitation pulse using CRT was performed using a TE/TR = 3.4/320 ms. Additional sequence prescriptions for this rat study included: FOV =  $8 \times 8 \text{ cm}^2$ , slice thickness of 20 mm, resolution =  $2.5 \times 2.5 \text{ mm}^2$  (using a maximum gradient amplitude of 50 mT/m and maximum slew rate of 200 mT/m/ms). CRT was prospectively undersample by 1.45 spatially, using 11 rings instead of the 16 rings required for full sampling. The inner 6 rings were fully sampled for calibration and outer 5 rings were evenly undersampled by 2. The reconstructed results were  $32 \times 32 \times 42$  (spatial + spatial + spectral) matrices.

### **Reconstruction and Data Processing**

Image reconstruction and postprocessing were carried out in Matlab. I applied density compensation to the non-Cartesian raw data, 3D gridded it into Cartesian data, and then performed an FFT. Gridding and FFT were done by using Fessler's non-uniform fast Fourier transform (NUFFT) toolbox [25] with min-max Kaiser-Bessel kernel interpolation and twice oversampling. The matrix size of the reconstructed CRT image was  $2N_{\text{ring}} \times 2N_{\text{ring}} \times N_{\text{rev}}$  after 3D gridding (2D spatial + 1D spectral). The same NUFFT reconstruction method was also applicable for symmetric EPSI (Nyquist-constrained), flyabck EPSI and spiral spec-

troscopic imaging. In the symmetric EPSI reconstruction, for each readout, the data was separated into 50 odd echoes and 50 even echoes, and then reconstructed by 3D gridding respectively, and finally average the two results.

For spectroscopic imaging data, peak heights were assessed to quantify SNR. The noise was calculated, using an area outside of the object but within the FOV, as standard deviation of the whole spectra. The same area (relatively uniform) were chosen to analyze SNR of CRT, spiral and EPSI. Median signal values among all the voxels in the selected area, along with standard deviation were used to quantify the SNR of each metabolites. Metabolites SNR were also normalized to the acquisition time to analyze SNR efficiency.

For parallel imaging simulations, non-regularized CG-SENSE [32] reconstruction and Monte-Carlo method were performed to compute the g-factor maps. For parallel imaging in vivo experiments, sensitivity maps were obtained by the auto-calibration method EPSIRiT [31] and L1-regularized SENSE was used for reconstruction.

## 3.3 Results

### 3.3.1 Theoretical Comparison of the Concentric Rings Trajectory with EPSI and Spiral

In the following, I compared CRT with EPSI and spiral MRSI trajectories in terms of resolution, acquisition time, SNR efficiency, and spectral bandwidth.

#### Acquisition Time

As shown in Fig 3.3 (top-left), since both symmetric EPSI and flyback EPSI have the same number of phase encodings and interleaves are not required, they result in the same total acquisition time for each individual resolution. Compared with EPSI, CRT requires fewer phase encodings and no interleaves, so it results in saving half of the total acquisition time given the same TR. For the spiral trajectory design, I used a time-optimal spiral in order to optimize the gradient duration and required interleaving of the spiral trajectory to fulfill

the spectral bandwidth requirement (500 Hz). Spirals are the most time efficient of all the trajectories, while CRTs are twice as fast as EPSI trajectories.

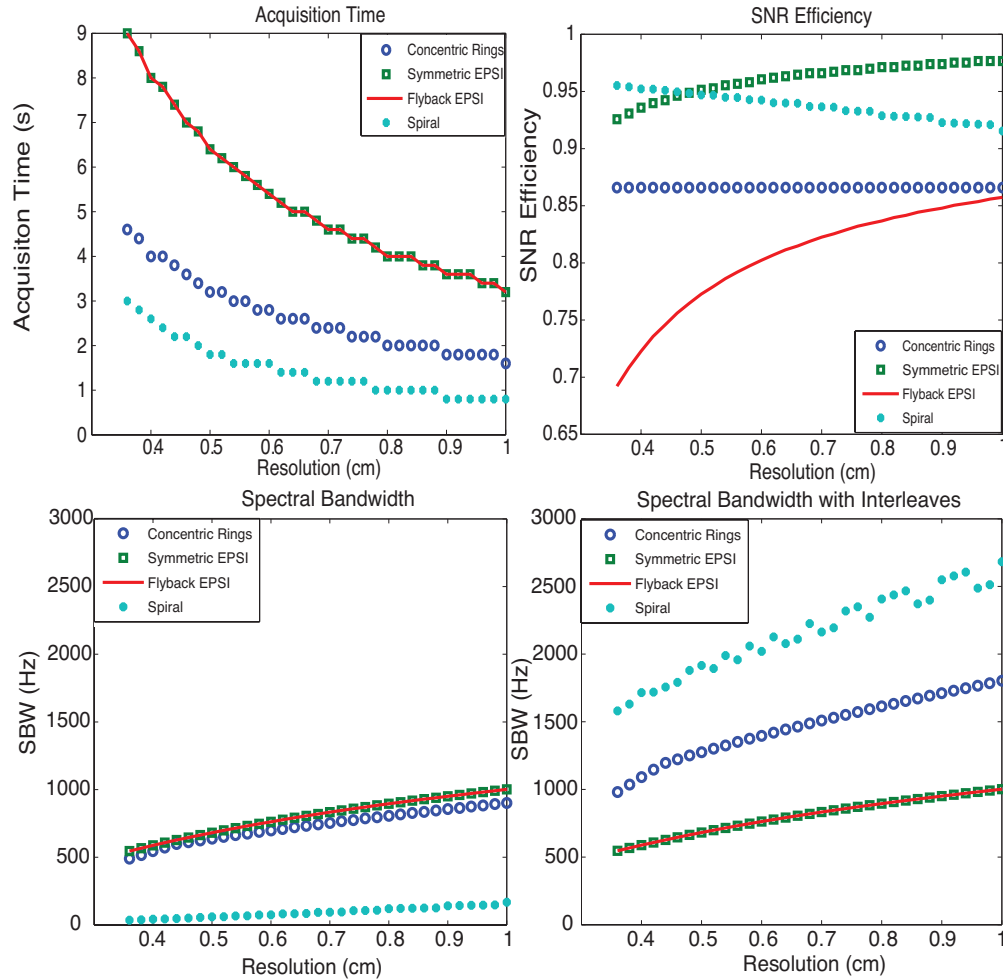


Figure 3.3: top-left shows the acquisition time; top-right shows the SNR efficiency; bottom-left and bottom-right show the SBW and SBW with spectral interleaves. CRT requires half of the total acquisition time compared with EPSI trajectories, offers about 87% SNR efficiency, and provides much wider spectral bandwidth than flyback EPSI and symmetric EPSI. Although nominally spirals are the most efficient trajectories, offering the best acquisition time and spectral bandwidth benefit while sacrificing the least SNR, they are limited by susceptibility to gradient infidelities.

### SNR Efficiency

Fig 3.3 (top-right) shows the SNR efficiency of different trajectories with various resolution

prescriptions. The SNR loss for flyback EPSI is mostly due to its low duty cycle. The finer the resolution is, the lower the duty cycle will be and SNR efficiency decreases as the flyback portion requires more time. Although the duty cycle for symmetric EPSI is 100% (including ramp sampling), the non-uniform k-space sampling resulting from the ramp part of the trapezoid waveform reduces the SNR efficiency to some extent. The SNR efficiency is very high for symmetric EPSI but not 100%. As the resolution gets coarser, the ramp portion is smaller, so the SNR efficiency is higher. For the constant slew rate spiral trajectories, the SNR efficiency decreases as the resolution becomes coarser with a fixed FOV since there is proportionally less outer k-space sampling where spirals are more uniform than inner k-space. Non-uniformity results in the most of the SNR loss of spirals while duty cycle results in a smaller fraction of the loss. Benefiting from the design of constant slew rate, the spiral trajectories provide even better SNR efficiency than flyback EPSI and CRT. CRT offers a constant SNR efficiency of  $\frac{\sqrt{3}}{2}$ , which is better than flyback EPSI with the chosen prescriptions. The loss of SNR efficiency for CRT is caused by the non-uniformity.

### **Spectral Bandwidth**

EPSI traverses a rectilinear line in k-space for each retracing period, CRT traverses a circle, while spiral traverses the whole spatial k-space in each period. Given the same traversing velocity (determined by the gradient waveforms), accordingly, the achieved SBW for EPSI, CRT, and spirals are decreasing in order, as shown in Fig 3.3 (bottom-left) without interleaves. To exploit the maximum spectral bandwidth, both symmetric EPSI and flyback EPSI result in the same waveform design thus achieving the same spectral bandwidth. They are only slightly better than CRT since flyback EPSI requires flyback time and symmetric EPSI (Nyquist-constrained) does not critically exploit the whole spectral bandwidth.

However, CRT and spiral trajectories are more scan-time-efficient compared with EPSI. If I take advantage of scan-time-efficiency by applying interleaves in temporal domain, I can increase SBW. In Fig 3.3 (bottom-right), the SBW of all trajectories was computed by accounting for the interleaves in time domain constrained for the same total acquisition time. Considering this tradeoff, spiral trajectories offer the best SBW, while CRT's spectral

bandwidth is doubled compared to EPSI.

The non-monotonicity of the spiral trajectories SBW with respect to resolution in this analysis is due to using an integer number of interleaves.

### **$^{13}\text{C}$ Phantom Spectroscopic Imaging Using CRT**

As I could tell from the 4-compartment phantom for Carbon-13 (Fig 3.4), the singlet peaks of  $^{13}\text{C}$  bicarbonate (on the top left),  $[1-^{13}\text{C}]$ lactate (on the top right) and  $[1-^{13}\text{C}]$ alanine (on the bottom left) and doublet of  $^{13}\text{C}$  formate (on the bottom right) were well resolved when using interleaved CRT with  $\text{SBW} = 1000$  Hz. The  $^{13}\text{C}$  2D image was obtained by spatially zero padding and projecting along the spectral domain, in order to display all the compartments. At this resolution, I observed that the edges of the different compartments were well resolved in  $^{13}\text{C}$  2D image and it matched well with the proton reference image.



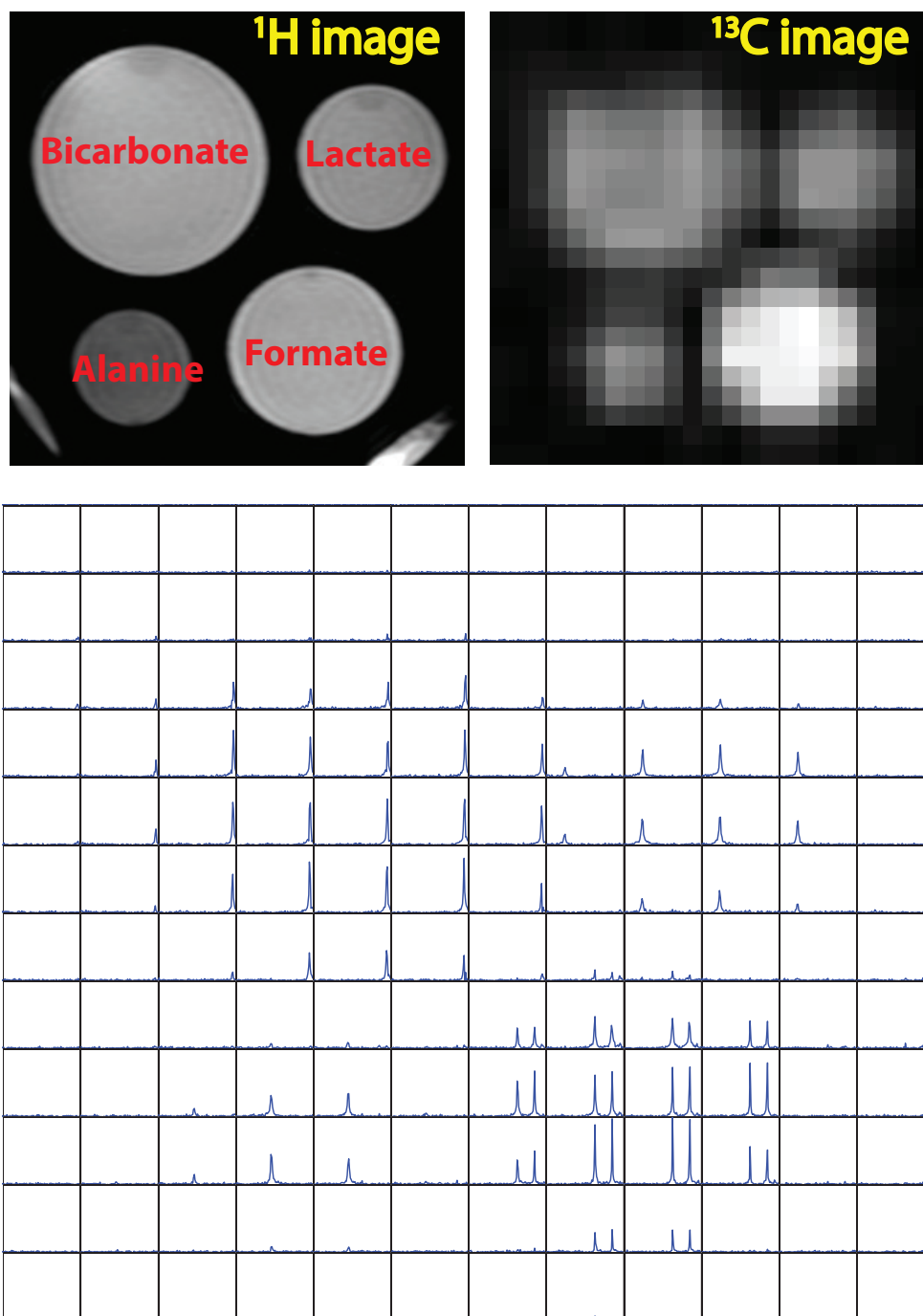


Figure 3.4: (top-left)  $^1\text{H}$  image localizer; (top-right)  $^{13}\text{C}$  2D image via projection on spectral domain; (bottom) spatial-spectral display for spectroscopic imaging. The displayed  $^{13}\text{C}$  2D image has the nominal spatial resolution of  $1.83 \times 1.83 \text{ mm}^2$  after zero padding. The reconstructed spatial-spectral (2D spatial+1D spectral) data matrix ( $22 \times 22 \times 100$ ) was cropped to  $12 \times 12 \times 100$ , and the SBW for each voxel was 1000 Hz. This was a non-hyperpolarized study, with the  $\text{TR} = 5 \text{ s}$  and total acquisition time of 1min 50 s.

### 3.3.2 Comparison of CRT, Spiral and EPSI on $^{13}\text{C}$ Phantom

Fig 3.5 shows the phantom comparison results from CRT, spiral and EPSI (from left to right). The first row in Fig 3.5 shows 2D images obtained by twice spatially zero padding and projecting along the spectral domain. While all MRSI trajectories showed very comparable image quality, I did observe a slight blurring with the spiral and EPSI trajectories (yellow arrows) compared to the CRT. For the spiral trajectory, I observed an isotropic approximately half-voxel blurring, while for EPSI I observed approximately half-voxel blurring in the readout direction (left/right). These might be the result of induced eddy currents, which could be measured and corrected for by performing trajectory measurements.

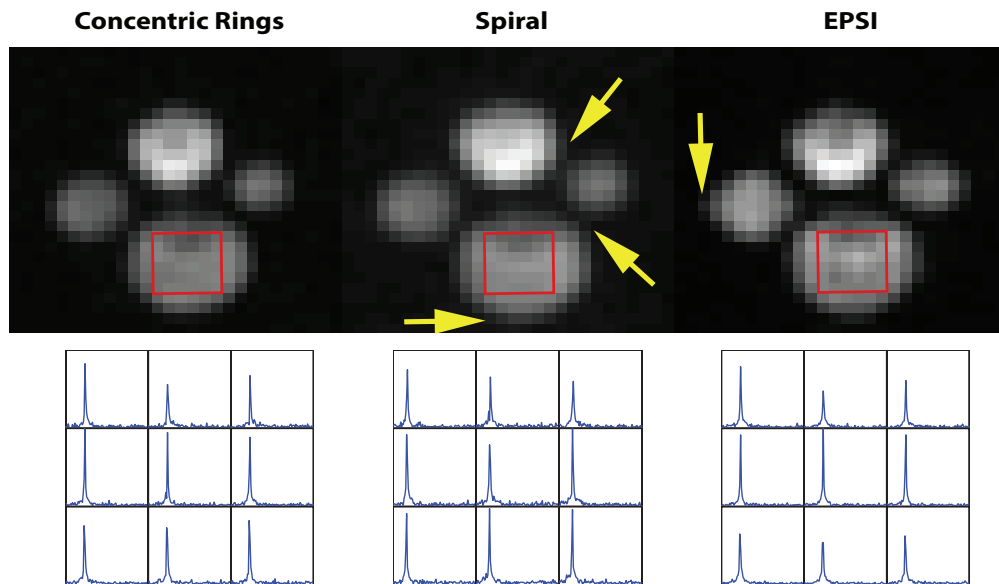


Figure 3.5: the top row (from left to right) images were obtained from CRT, Spiral and EPSI respectively. They were created from spectroscopic images via projection along the spectral domain. The displayed  $^{13}\text{C}$  2D image has a nominal spatial resolution of  $1.83 \times 1.83 \text{ mm}^2$  after zero padding and was cropped into a  $5 \times 5 \text{ cm}^2$  ROI. The arrows show the slight blurring of spiral and EPSI. The bottom row (from left to right) plots are of  $^{13}\text{C}$  bicarbonate spectra obtained from CRT, Spiral and EPSI, respectively, from the same 9 voxels.

For SNR comparison, I selected 9 voxels (in red boxes) in the  $^{13}\text{C}$  bicarbonate chamber. For comparison, these raw SNR values were normalized by the acquisition time, as shown in

Table 3.1. Spiral MRSI had a superior normalized SNR over CRT and EPSI, which coincides with the comparison plot shown in Fig 3.3. Overall, CRT provided some improvement in image quality (without using any trajectory measurements) but a reduced SNR efficiency.

Table 3.1: SNR comparison of CRT, Spiral and EPSI trajectories in a  $^{13}\text{C}$  Phantom

	CRT	Spiral	EPSI
Raw SNR	44.1297±7.3599	42.0563±6.7352	69.9937±14.1840
Scan Time	1 min 50 s	1 min 15 s	3 min 40 s
Normalized SNR	36.4389	42.0563	40.8675

### 3.3.3 Hyperpolarized $^{13}\text{C}$ In Vivo Spectroscopic Imaging with Concentric Rings

The imaging plane was chosen at the abdomen of a rat in axial view ( in Fig 3.6). The kidneys of rats showed the high uptake of pyruvate and its conversion to alanine and lactate. Spatially, the  $[1-^{13}\text{C}]$  pyruvate image (Fig.3.6b) and  $[1-^{13}\text{C}]$  lactate image (Fig.3.6c) captured the structure of the kidneys and vasculature, and metabolic conversion. Resolution of different metabolites was captured in the  $^{13}\text{C}$  spectrum with 500 Hz SBW (a selected voxel is shown in Fig.3.6d). Pyruvate and lactate images were twice zero padded to have a displayed resolution of  $1.83 \times 1.83 \text{ mm}^2$ . The total scan time was 2.2 s.

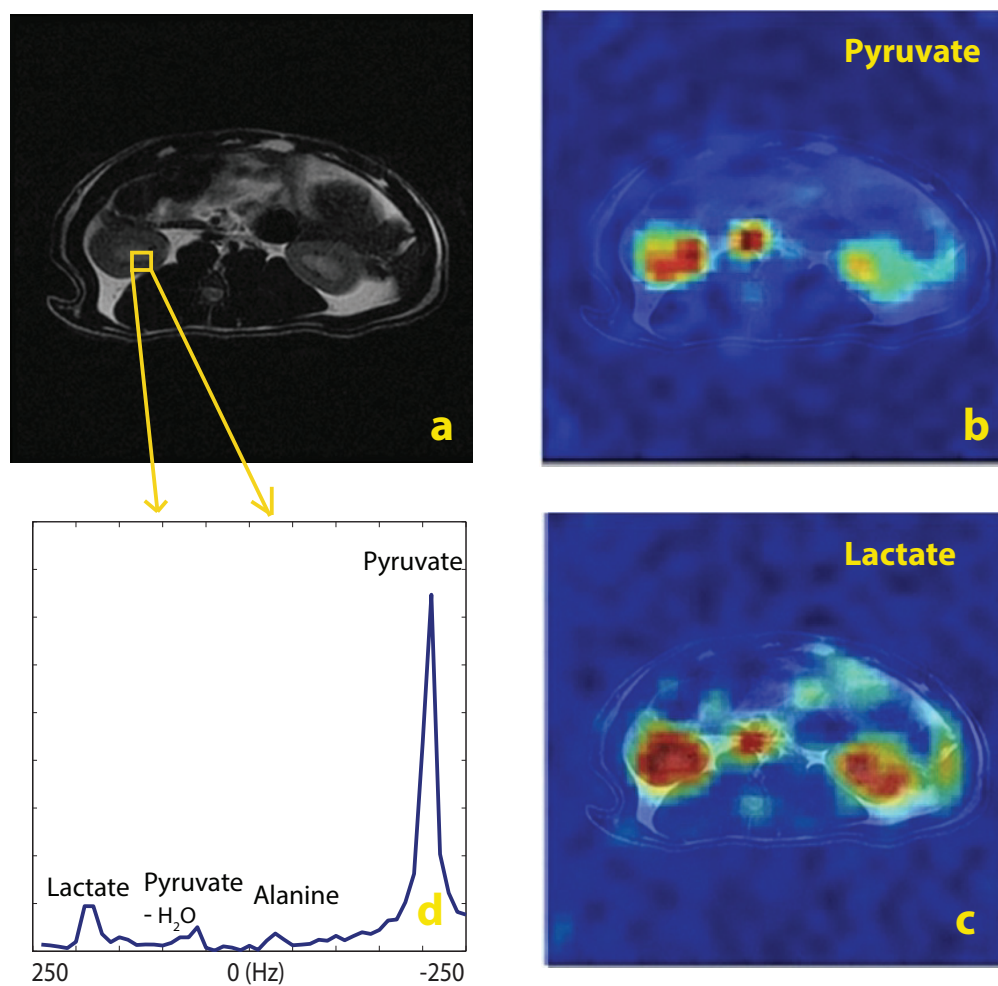


Figure 3.6: In vivo results using concentric rings in a normal rat (axial): a.  $^1\text{H}$  T2-weighted localizer; b.  $[1-^{13}\text{C}]$  pyruvate image; c.  $[1-^{13}\text{C}]$  lactate image; d. the  $^{13}\text{C}$  spectrum of a selected voxel with 500 Hz SBW. MRSI was acquired with a spatial resolution of  $3.67 \times 3.67 \text{ mm}^2$ . Pyruvate image and lactate images were twice zero padded to have a resolution of  $1.83 \times 1.83 \text{ mm}^2$ . For display purposes, the intensity of lactate image was scaled up by 7. The total scan time was 2.2 s.

### 3.3.4 Comparison between Concentric Rings and EPSI with Hyperpolarized $^{13}\text{C}$ In Vivo

CRT and a Nyquist-constrained EPSI counterpart with the same prescriptions were compared, where the total scan time for CRT was 2.75 s while it was 4.4 s for EPSI. In Fig 3.7, 2D images were obtained from the projection along the spectral domain. Both methods captured the anatomical structure and metabolic conversion with comparable quality. As the red arrows show, the through-plane flow in the major vessels resulted in ghosting replicas in the phase encoding direction for EPSI. However, pulsatile flow in CRT will manifest as low-amplitude background halos [61], which may have lead to increased background signal in CRT.

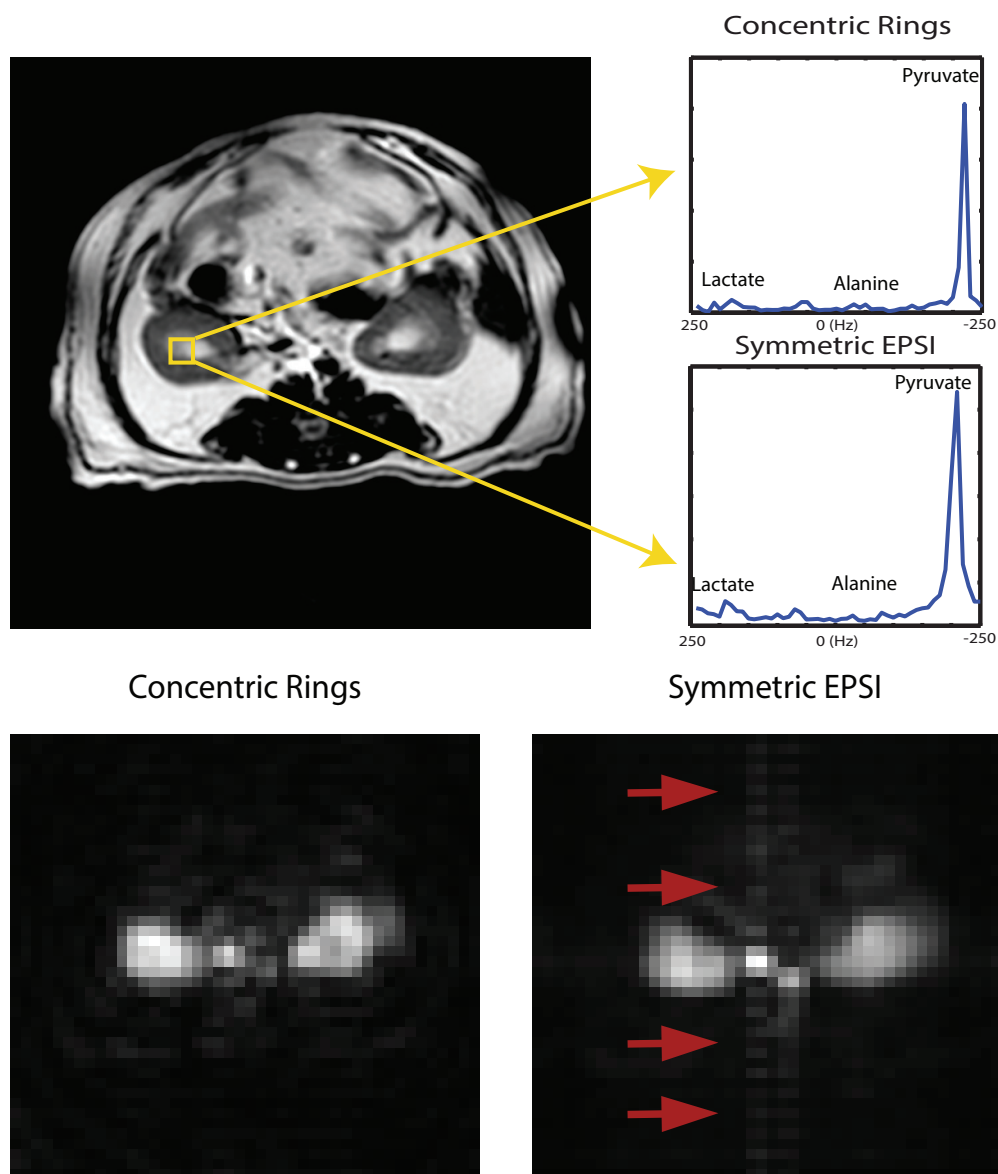


Figure 3.7: In vivo results in an axial kidney slice using concentric rings and symmetric EPSI: (top-left)  $^1\text{H}$  T2-weighted localizer; (top-right) spectrum from concentric ring trajectory and spectrum from EPSI trajectory respectively, both sequences captured the conversion of pyruvate with comparable SNR; Bottom figures show pulsatile flow effects on concentric rings and EPSI: (bottom-left) 2D image from the concentric rings and (bottom-right) 2D image from EPSI, via projection along spectral domain.

I also compared CRT and a critical EPSI counterpart with the same prescriptions, where

the total scan time for CRT was 2.2 s while it was 4.4 s for EPSI. In Fig 3.8, I extracted 2D images at  $TE = 43.4$  ms, to show the pulsatile flow effects on both CRT and EPSI. As the red arrows show, the through-plane flow in the major vessels resulted in ghosting replicas in phase encoding direction for EPSI. However, I did not observe any pulsatile flow artifacts on CRT at any echo time. Additionally, as the red arrow points out in Fig 3.8, EPSI suffered from spectral aliasing caused by gradient delays and/or eddy currents. Due to the back and forth readout directions across k-space, gradient delays or eddy currents translate into phase accrual in opposite directions, resulting in such aliasing in the spectral domain.

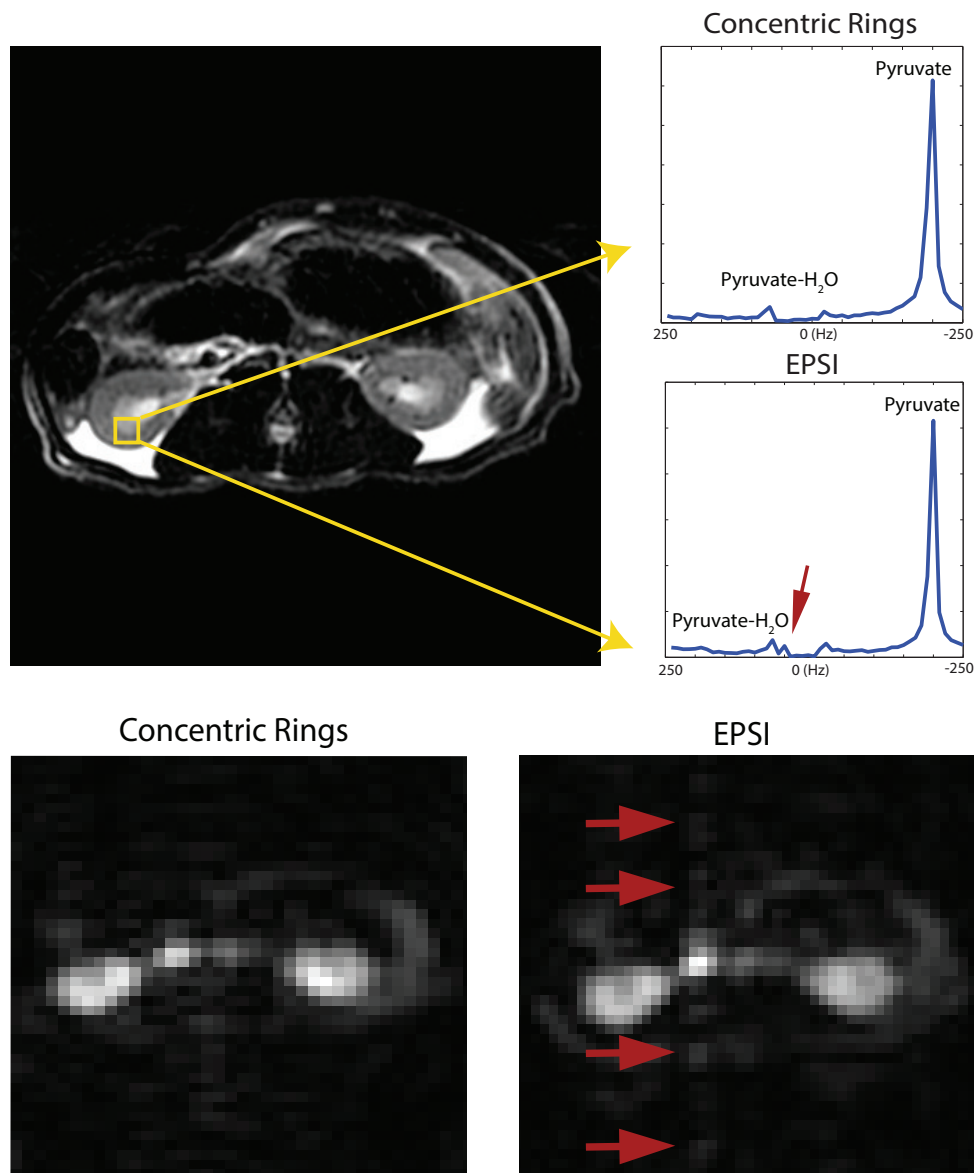


Figure 3.8: In vivo results using concentric rings and critical EPSI: Top figures show the system imperfections effects on concentric rings and critical EPSI: (top-left)  $^1\text{H}$  T2-weighted localizer; (top-right) spectrum from concentric ring trajectory and spectrum from EPSI trajectory respectively, where the red arrow points out the spectral aliasing caused by gradient delays and/or eddy currents; bottom figures show pulsatile flow effects on concentric rings and EPSI: (bottom-left) 2D image from the concentric rings and (bottom-right) 2D image from EPSI with twice zero-padding, both at  $\text{TE} = 43.4$  ms.



### 3.3.5 Parallel Imaging with the Concentric Rings

#### Simulated G-factor

As the simulated g-factor maps (in Fig 3.9) confirm, the non-rectilinear circular sampling pattern of CRT results in more incoherent noise amplification than Cartesian counterparts such as EPSI. Noise is amplified by 3-4 times at discrete locations for the Cartesian undersampling pattern due to the worse conditioning of the reconstruction problem. For CRT, the noise was more uniformly distributed spatially, resulting in a noise amplification of no more than 2.5 for this simulated 8-channel array with  $4\times$  undersampling. (In conjunction with appropriate regularization, the g-factor can be further improved.) The non-Cartesian sampling pattern of concentric rings is advantageous because it makes the noise amplification incoherent thus lowering the g-factor of the whole space.

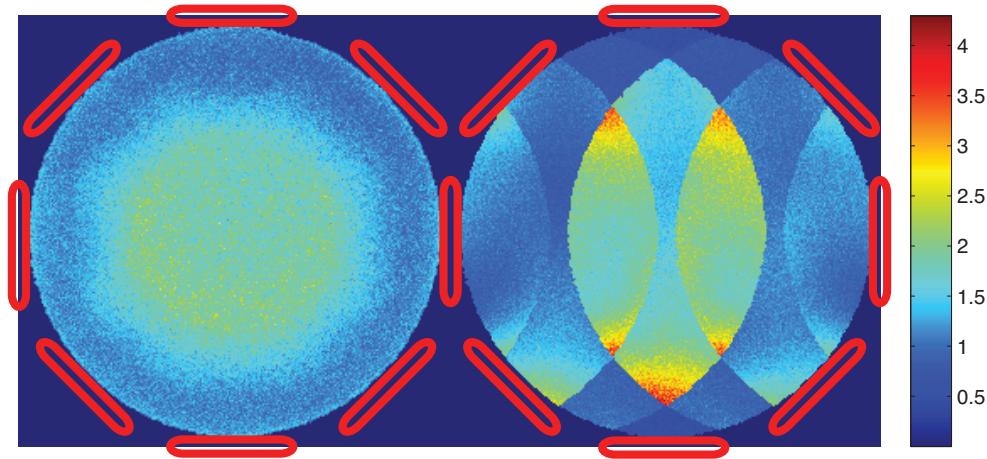


Figure 3.9: Simulated g-factor map of  $4\times$  undersampled concentric rings trajectory (on the left) and Cartesian trajectory counterpart, such as EPSI, (on the right) for a simulated 8-channel array. The isotropic non-Cartesian undersampling pattern of the concentric rings trajectory results in less coherent noise amplification than the Cartesian counterpart.

#### Parallel Imaging for Hyperpolarized $^{13}\text{C}$ in vivo Spectroscopic Imaging

An 8-channel  $^{13}\text{C}$  phased-array rat coil was constructed especially for this study with the coils

distributed isotropically around the animal in the axial plane as shown in the left of Fig 3.10. The hyperpolarized  $^{13}\text{C}$ -pyruvate in vivo spectroscopic imaging in Fig 3.10 demonstrates for the first time parallel imaging with CRT. The direct reconstruction of the prospectively undersampled data resulted in the circular aliasing artifacts (yellow arrows) in the spatial domain for each coil image (top row of Fig 3.10). These coil images were generated from the projection along the spectral domain for display. The total scan time was 3.52 s, achieved by prospective  $1.45\times$  acceleration. With a parallel imaging reconstruction, the undersampling aliasing was eliminated and good image quality was achieved, as is shown on the bottom left of Fig 3.10. The bottom right plot shows the spectrum of a selected kidney voxel, clearly showing pyruvate and its conversion to lactate.

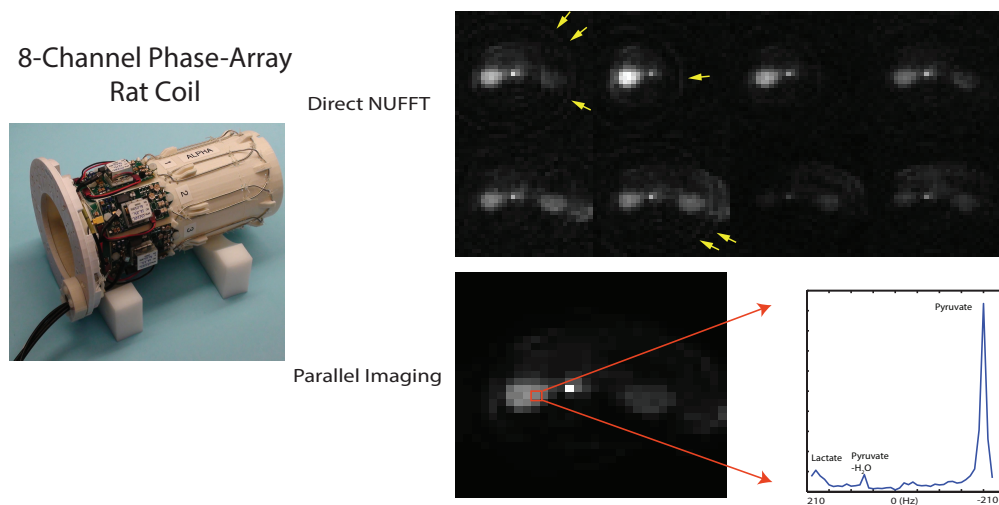


Figure 3.10: Parallel imaging in vivo results in an axial kidney slice using CRT with an 8-channel phased-array rat coil: the spectroscopic imaging CRT was spatially undersampled by 1.45, with a spatial resolution of  $2.5\times 2.5\text{ mm}^2$ ,  $8\times 8\text{ cm}^2$  FOV and 420 Hz SBW. The left of the figure shows the 8-channel phased-array rat coil. The top right part shows individual coil images of the undersampled CRT using a direct NUFFT reconstruction, where the coil images were generated by projection along the spectral domain. The 8 coils were distributed isotropically around the animal in the axial plane. The bottom right part shows the parallel imaging reconstruction result. The 2D image was obtained from projection along the spectral domain and the spectrum from a selected kidney voxel was displayed to show the resolution of various metabolites, including lactate resulting from metabolic conversion. The total scan time was 3.52 s.

### 3.4 Discussion

CRT provides a competitive alternative to existing  $^{13}\text{C}$  spectroscopic imaging acquisition methods.

The CRT sequence requires half the number of excitations compared to EPSI. This has an advantage in two-fold acquisition time savings. In addition, the T1 decay is reduced, which leads to overall higher SNR [50].

The acquisition time saving can be traded off for an increased spectral bandwidth through interleaving. I also showed that even though CRT samples k-space non-uniformly, its SNR efficiency is still  $\frac{\sqrt{3}}{2} \approx 0.87$  of uniform sampling.

I expect that the concentric rings trajectory will be more robust to system imperfections than spirals or critical symmetric EPSI. For all trajectories, any gradient timing delay or eddy currents will result in some artifacts. In spirals, these cause spatial blurring. In critical symmetric EPSI, one effect of these is odd-even echo inconsistency which results in spectral aliasing. This is analogous to ghosting artifacts in EPI [72]. For CRT, delays and first-order eddy currents result in benign image rotations [61]. More importantly, no spectral aliasing or spatial aliasing artifacts will be observed.

One of the advantages of using CRT is robustness to flow, that was also reported in [61]. Pulsatile flow is distributed in two dimensions by CRT and spiral [73]. In contrast, EPSI trajectories can suffer from significant pulsatile flow artifacts where flow results in replicas in phase encoding direction.

Combining CRT with parallel imaging for hyperpolarized  $^{13}\text{C}$  imaging is also very promising. Undersampling is achieved by acquiring fewer rings than what are necessary for in plane full-FOV. I showed in Monte Carlo simulations that with CRT the resulting g-factor due to undersampling is lower than for Cartesian undersampling. The reason is that CRT undersamples isotropically in-plane, whereas Cartesian imaging can accelerate only in the phase-encoding directions. As a result, CRT acquisitions can better utilize the multi-dimensional spatial variation of the coils sensitivities to improve the conditioning of

the reconstruction. Furthermore, hyperpolarized  $^{13}\text{C}$  imaging do not suffer from the usual  $\sqrt{R}$  loss of SNR due to subsampling. The reason is that the total magnetization can be redistributed optimally to fewer number of excitations. Hyperpolarized  $^{13}\text{C}$  parallel imaging with CRT is essential for the large FOV applications, *e.g.*, metastatic cancer imaging.

There are some possible extensions of CRT for  $^{13}\text{C}$  MRSI: (1) the shorter scan time could be amortized for dynamic MRSI to track perfusion and metabolism kinetics; (2) 3D MRSI to cover a larger volume *in vivo*; (3) variable-density undersampling designs for parallel imaging, maintaining the inner k-space fully sampled to capture the intrinsic contrast and outer k-space undersampled for resolution and acceleration; (4) compressed sensing, taking advantages of intrinsically sparse  $^{13}\text{C}$  spectra [53, 54]. These improvements could further reduce the total scan time.

I initially performed high resolution  $^1\text{H}$  MRSI studies to evaluate the CRT sequence. Through these studies, I observed some spatial and spectral blurring, which I were able to model as gradient induced phase errors. I measured this to be approximately quadratically varying with total gradient magnitude and linearly time-accumulating. Based on these measurements, I applied a quadratic phase compensation for  $^1\text{H}$  MRSI data that resulted in effective removal of the blurring effects. I eliminated the possibilities of concomitant gradients [74] and first order eddy currents, but did not determine the source of these phase errors. The blurring was only prominent in high resolution  $^1\text{H}$  MRSI data. For  $^{13}\text{C}$  data, the amount of phase observed would not result in noticeable blurring, and I observed no visible artifacts. I also observed the phase error varied between different GE 3.0 T scanners, so I suspect it is related to some gradient system compensations.

### 3.5 Conclusion

The preclinical studies have demonstrated the potential and feasibility of using concentric rings in hyperpolarized  $^{13}\text{C}$  MRSI for a two-fold acceleration over EPSI, with inherent robustness to flow artifacts, gradient system delay, and first-order eddy currents. Parallel

imaging will also benefit from this trajectory for hyperpolarized  $^{13}\text{C}$  imaging. Compared with existing methods, the CRT provides flexible and robust trade-off between acquisition time and SBW, thereby acting as an effective alternative for hyperpolarized  $^{13}\text{C}$  MRSI.

# Chapter 4

## Motion Robust High Resolution Free-breathing Pulmonary Imaging

### 4.1 Introduction

Pulmonary imaging with MRI has potential to characterize soft tissue using a wide range of available image contrasts (e.g. T1, T2, diffusion, perfusion, ventilation). Further, the use of MRI in place of CT avoids radiation dose which carries substantial risks with repeated radiation exposure [75, 76, 77, 78]. These benefits of pulmonary MRI are most relevant in pediatric diseases requiring longitudinal follow-up, such as cystic fibrosis and assessing pulmonary nodules, and could also enable imaging studies in much more widespread lung diseases such as asthma. However, achieving morphological lung MRI with comparable diagnostic value to CT is challenging due to the combined factors of short T2\*, low proton density, and respiratory motion.

A variety of pulse sequence techniques and acquisition procedures have been developed to address these challenges[79, 80, 81, 82, 83, 84, 85, 86]. Among these techniques, radial ultrashort echo time (UTE) imaging has shown significant promise for high-quality pulmonary imaging due to its ability to capture the rapidly decaying signal and its robustness to motion

[79, 85, 86]. Recently, 3D radial UTE sequences with readout optimized for SNR efficiency have been proposed [86] for free-breathing pulmonary imaging. While these modifications enhance the ability to assess lung parenchyma, appropriate motion compensation models are still necessary to resolve respiration.

For a respiratory motion compensation model to be effective, accurate motion estimation must first be obtained. External respiratory bellows can be used to estimate respiratory motion but are prone to errors. Most dominantly, the motion of the abdominal wall is often poorly coupled to actual subject motion which leads to inaccurate respiratory motion estimation [5, 86]. Motion information can be alternatively extracted directly from the acquired k-space data as a self-navigator. A common approach is to use the k-space center (DC), representing the average signal of the excitation volume, as a self-navigation signal [4, 5, 87, 88, 89, 90, 91, 92, 93, 94]. While the DC signal is sensitive to motion throughout the imaging volume, there is not a direct relationship between the amount of signal deviation and respiratory motion. Moreover, other factors like coil-related signal intensity drifts, bulk motion, and imaging gradient eddy currents can cause erroneous motion estimation. Image-based self-navigation can provide a direct measurement of motion, and recent studies have shown that this approach had significantly better image sharpness than any of the DC-based self-navigation methods [95, 96].

To account for respiratory motion when reconstructing images, a variety of methods have been proposed. One class of methods aims to explicitly solve for motion displacement and compensate it during the reconstruction. In particular, Batchelor and others [97, 98, 99] proposed generalized matrix models to incorporate arbitrary motion displacement operators into the forward reconstruction model. Methods using image registration [6, 100, 101, 102, 103, 104, 105, 106, 107] were also proposed to correct for motion by iteratively alternating between image registration and reconstruction. Additionally, Cheng and others proposed local auto-focusing methods [91, 108, 109, 110, 111] to choose the sharpest image in a local region according to a gradient entropy metric. While these methods were shown to be effective to reduce motion artifacts in many applications, errors in their underlying motion

models may introduce artifacts.

For this work, I focus on another class of reconstruction methods that implicitly exploits image correlations from different respiratory motion states. While compromising the ability to correct for motion, this class of methods is very robust to motion model errors. In particular, I focus on soft-gating [112, 113, 114, 115] and motion-resolved methods [116]. Soft-gating is a computationally efficient iterative method in which the data consistency term in the optimization is preferentially weighted based on distances from the chosen respiratory motion state. The motion-resolved method, on the other hand, divides the data into several respiratory motion states and enforces correlations between motion states in an iterative reconstruction.

The purpose of this work is to provide motion robust high resolution 3D pulmonary imaging using the following approach: I. data acquisition with an optimized 3D UTE sequence, II. motion estimation with a lower-resolution, high frame rate dynamic 3D self-navigator from the subset of acquired data with reconstruction that combines parallel imaging [32] and compressed sensing[34] with locally low-rank constraints[117, 118], III. motion compensation using a retrospective soft-gating technique to reconstruct high-resolution images at a chosen motion state, IV. a respiratory motion-resolved technique to provide images of all respiratory motion states, and V. the incorporation of L1-ESPIRiT [31], an auto-calibrating parallel imaging and compressed sensing method. I applied the proposed methods to healthy volunteers as well as subjects with cystic fibrosis and pulmonary nodules to demonstrate feasibility for clinical applications.

## 4.2 Methods

### 4.2.1 Data Acquisition

An optimized free-breathing 3D radial UTE sequence with slab excitation and a bit-reversed view ordering from Johnson et al. [86] was implemented. It incorporates variable density



readout gradients to improve SNR efficiency and slab excitation to reduce the number of encodings and artifacts from the fringe of the gradient and  $B_0$  fields. The pseudorandom view ordering determined by a bit-reversed algorithm mitigates structured artifacts enabling free-breathing pulmonary imaging. A diagram of the pulse sequence is shown in Fig 4.1. More details about the sequence design are described in [86]. Specific acquisition parameters are described in the following Experiment section.

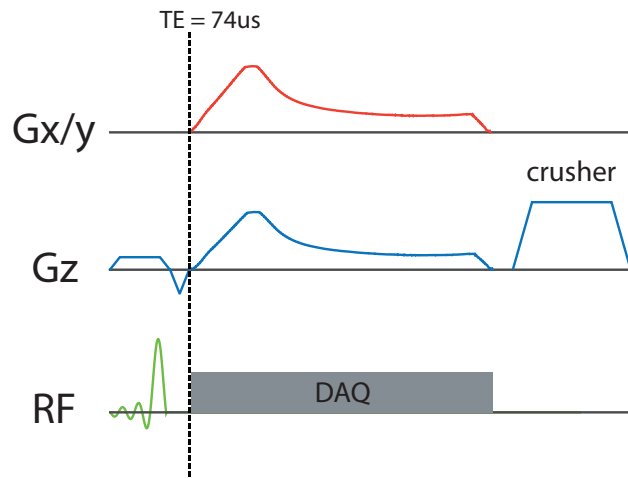


Figure 4.1: Illustration of the pulse sequence: slab excitation gradient with minimum-phase RF are adopted to reduce artifacts and provide short TE; readout gradients are designed to be variable density in order to improve SNR efficiency.

Based on this sequence, the acquired data is fed into two processing branches illustrated in Fig 4.2: the first branch is for reconstructing high frame rate, lower-resolution dynamic 3D images for self-navigation, followed by respiratory motion estimation; the second branch is for reconstructing high resolution images, compensated for motion by data from the first branch, and includes soft-gating L1-ESPIRiT and respiratory motion-resolved L1-ESPIRiT reconstructions described below.

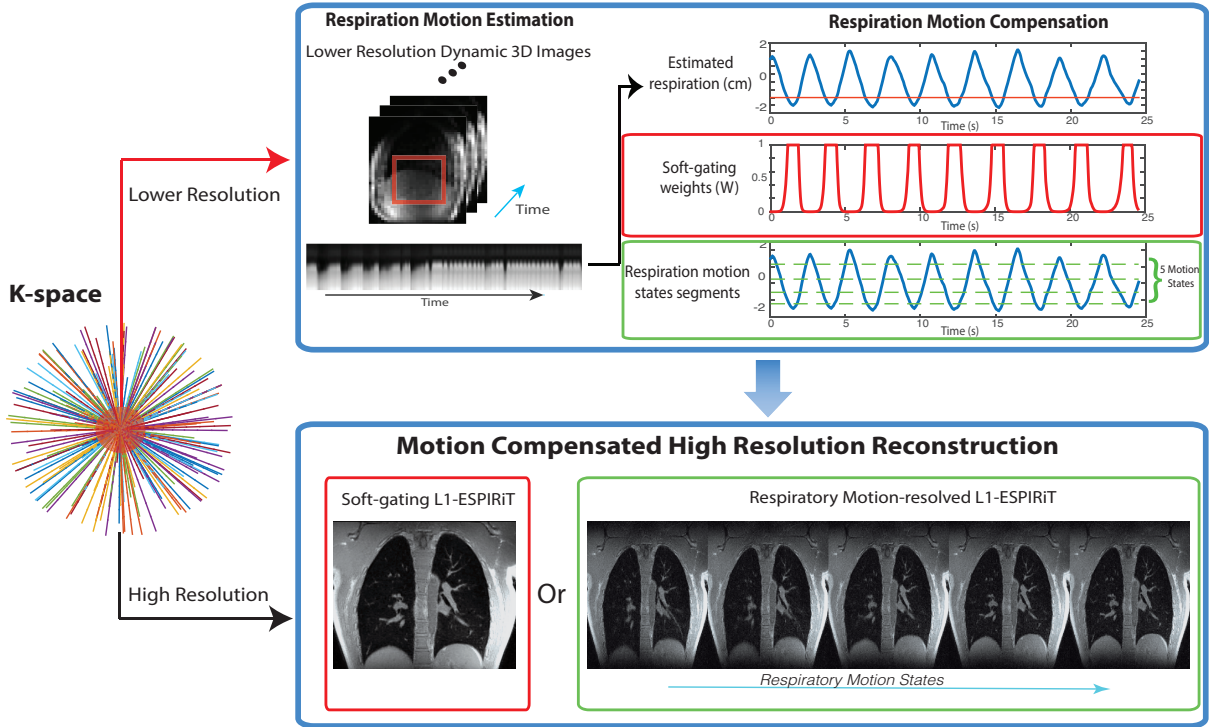


Figure 4.2: Illustration of the proposed methods: (*top branch*) Respiratory motion estimation from a dynamic 3D self-navigator, reconstructed using a central k-space region. This estimation is used to derive motion compensation information for the soft-gating and motion-resolved methods. The red line in the top respiration signal plot illustrates the soft-gating threshold. (*bottom branch*) Respiratory motion compensated reconstruction of high resolution images based on soft-gating and respiratory motion-resolved methods using the 1D motion surrogate signal derived from top branch.

## 4.2.2 Locally Low Rank Constraints for Respiration Motion Estimation

In radial acquisitions, the center of k-space is sampled repeatedly in every spoke, which can be exploited for motion estimation. Changes in the k-space center (DC) signal reflect changes in average image intensity and phase that can be used for motion estimation, and multiple coils can further provide localized information [119, 120, 88, 121, 122]. However, DC signals are susceptible to coil-related signal intensity drifts that could arise from gradient heating,

and also remain sensitive to bulk motion or the rotating of readout direction. Thus, they often lack direct correspondence with respiratory motion. Motivated by these limitations, I propose a novel image-based self-navigated method using lower-resolution dynamic 3D images to quantitatively estimate respiration motion.

### Dynamic 3D Self-Navigator using Locally Low-rank Constraints

Here I describe a new method to reconstruct high frame rate, lower-resolution dynamic 3D images from the radial UTE central k-space data for motion estimation by exploiting spatiotemporal correlations with locally low-rank constraints. The 3D UTE acquisition uses a pseudo-random view ordering such that every subset of contiguously acquired radial profiles covers k-space with a relatively uniform angular distribution, which enables resolving lower-resolution dynamic images. However, to achieve sufficient temporal resolution ( $\geq 2$  Hz) and acceptable spatial resolution ( $\leq 1$  cm) to visualize respiratory motion, it requires more than 200-fold undersampling for every frame with respect to the Nyquist criterion. This is far beyond the maximum undersampling factor of typical parallel imaging and compressed sensing methods. Therefore, I propose to iteratively solve for lower-resolution navigation images from consecutive subsets of data by exploiting spatiotemporal correlations with locally low-rank (LLR) [117, 118] constraints. These constraints provide additional data consistency to resolve aliased lower-resolution images. I formulate the problem in a parallel imaging and compressed sensing manner shown in Equation 4.1:

$$\operatorname{argmin}_{M_{\text{r}}} \frac{1}{2} \|DSM_{\text{r}} - y_{\text{r}}\|_2^2 + \lambda \sum_{i \in \Omega} \|L_i M_{\text{r}}\|_* \quad (4.1)$$

Here, the first term enforces data consistency where  $M_{\text{r}}$  represents dynamic lower-resolution images (3D spatial+1D temporal size:  $n_x \times n_y \times n_z \times n_t$ ),  $y_{\text{r}}$  are acquired data corresponding central region of radial k-space measurements,  $S$  represents the sensitivity maps (which can be estimated by ESPIRiT), and  $D$  is the multi-channel non-uniform Fourier Transform (3D radial) operator. The second term enforces LLR constraint, where the dynamic images  $M_{\text{r}}$  can be partitioned into a set  $\Omega$  of small image blocks (size:  $b_x \times b_y \times b_z \times n_t$ ),

$L_i$  is the operator that takes the block  $i$  of the image to form its Casorati matrix with an appropriate block size, and  $\lambda$  is a weighting factor to balance the constraints. This optimization problem in Equation 4.1 was solved by a fast iterative shrinkage-thresholding algorithm (FISTA)[123] with singular value thresholding (SVT) and randomized block shifting [124].

### 4.2.3 Motion Compensated Reconstruction

At their core, the motion compensated reconstructions use parallel imaging and compressed sensing to exploit the coil sensitivities and image transform sparsity for recovering both unacquired and corrupted k-space samples. This enables a clinically-feasible 5 minute scan, which typically has more than 8-fold undersampling with respect to the Nyquist criterion when motion is ignored. I propose two motion compensation strategies, soft-gating and respiratory motion-resolved, and incorporate them into a L1-ESPIRiT reconstruction framework.

#### General Reconstruction Framework - L1-ESPIRiT

I use L1-ESPIRiT, a combined parallel imaging and compressed sensing approach, as the basic reconstruction framework:

$$\underset{m}{\operatorname{argmin}} \quad \frac{1}{2} \|DSm - y\|_2^2 + \lambda \|\Phi m\|_1 \quad (4.2)$$

Here,  $m$  is the desired image (3D spatial size:  $N_x \times N_y \times N_z$ ),  $y$  is the acquired non-Cartesian data,  $S$  are the ESPIRiT sensitivity maps calculated from the oversampled central part of k-space,  $D$  is the non-Cartesian Fourier Transform (3D Radial) operator and  $\Phi$  is the 3D Daubechies wavelet transform. The first term in Equation 4.2 is a data consistency term that minimizes the difference between the acquired data  $y$  and the reconstructed image  $m$  through the acquisition model. The second term enforces sparsity by minimizing the L1-norm of the wavelet coefficients of  $m$ ,  $\lambda$  is the regularization parameter.

### Soft-gating L1-ESPIRiT Reconstruction

A common approach to correct for respiratory motion is gating, which selects a single motion state by rejecting data from the other states. This type of gating, which I refer to here as hard-gating, results in a relatively low scan efficiency. Alternatively, Johnson et al. [112], Cheng et al. [113] and also Forman et al. [114] proposed a simple and retrospective approach called soft-gating, where all data is used but with weighting based on the estimated amount of respiratory motion. The concept of soft-gating is illustrated in the top branch of Fig 4.2. The weights effectively take account for motion induced data inconsistency. I use the soft-gating approach by modifying the basic image reconstruction model (Equation 4.2) to incorporate appropriate weights  $W$ :

$$\operatorname{argmin}_m \frac{1}{2} \|W(DSm - y)\|_2^2 + \lambda \|\Phi m\|_1 \quad (4.3)$$

Here,  $W$  is a diagonal matrix containing the soft-gating weights, which are applied to the data consistency term. Let  $w[n]$  be the vector representing the diagonal entries of  $W$ . A different weight  $w[n]$  is estimated for each radial spoke  $n$ , ranging between 0 to 1:

$$w[n] = \begin{cases} e^{\alpha(d[n] - \text{threshold})}, & \text{if } d[n] > \text{threshold} \\ 1, & \text{otherwise} \end{cases} \quad (4.4)$$

where  $d[n]$  represents the estimated respiratory motion with respect to the end of expiration for each spoke, threshold is a threshold of the respiratory motion, and  $\alpha$  is a scaling factor. For data experiencing more respiratory motion corruption, their weights are smaller and thus they contribute less to the data consistency term in Equation 4.3.

Soft-gating parameters were experimentally tuned and then fixed for the rest of the study: the threshold was set as 25% of the maximum respiratory position and  $\alpha$  was set to  $3/\max(d[n])$ . We solved the optimization in Equation 4.3 using FISTA[123].

## Respiratory Motion-resolved L1-ESPIRiT Reconstruction

Another approach we propose to use for pulmonary imaging is a respiratory motion-resolved reconstruction. We take a similar approach as XD-GRASP proposed by Feng et al. [116]: sorting the free-breathing data into an extra respiratory motion-states dimension and constraining sparsity along the motion-states dimension by compressed sensing. The respiratory motion-resolved approach modifies the basic image reconstruction model (Equation 4.2) by extending the desired image to be 4D (3D spatial + 1D motion-states), and enforces sparsity along the motion-states dimension:

$$\operatorname{argmin}_M \frac{1}{2} \|DSM - y\|_2^2 + \lambda_1 \|\Phi M\|_1 + \lambda_2 \|M\|_{TV} \quad (4.5)$$

Here,  $M$  is the desired respiratory motion-resolved images (3D spatial + 1D motion-states),  $y$  is the acquired non-Cartesian data reformatted into different motion states according to estimated respiration signal,  $S$  is the ESPIRiT sensitivity maps, and  $D$  is the non-Cartesian Fourier (3D Radial) operator in the first term that enforces data consistency. The second term enforces spatial sparsity by minimizing the L1-norm of the wavelet coefficients of  $M$ . The wavelet transform operator is represented by  $\Phi$ . The third term enforces motion-state sparsity by minimizing the total variation (TV) norm along the extra respiratory motion dimension.  $\lambda_1$  and  $\lambda_2$  are the regularization weights for wavelet-domain sparsity and motion-state sparsity respectively. We solved the optimization in Equation 4.5 using the alternating direction method of multipliers (ADMM)

## Evaluation of Dynamic 3D Self-Navigator

For the dynamic 3D self-navigator, the beginning 16 % of the data along the readout was used to reconstruct lower-resolution images and estimate sensitivity maps. This results in 7.5 mm apparent isotropic spatial resolution. Lower-resolution 3D self-navigators were reconstructed on an  $80 \times 80 \times 80$  matrix of each frame with a temporal window width of 100 spokes, which yields an apparent temporal resolution of  $\approx 300$  ms (depends on TR value).

Effectively, every frame has the acceleration factor of 200 with respect to Nyquist criterion. We partitioned the images with the block size of  $8 \times 8 \times 8$ , and applied locally low-rank constraints on the temporal domain, using regularization of  $\lambda = 0.0005$ . For comparison, we performed a direct 3D gridding reconstruction on the same data of every temporal frame.

We compared dynamic 3D self-navigation with DC-based self-navigating and respiratory bellows navigation on a group of eight clinical patients with mixed patterns of breathing. Motion estimates from the dynamic 3D self-navigator were obtained by measuring the superior/inferior (SI) translation motion of the diaphragm by calculating cross correlations on a region-of-interest (ROI) in image domain. For DC-based self-navigation, we applied a low-pass (0.5 Hz cut-off frequency ) filter on the k-space center to extract the 1D respiration motion surrogate. An additional median filter was applied to the raw data. Finally, the asymmetric least-squares smoothing method [125] was performed to get rid of signal intensity drifts.

Pearson correlation coefficient analysis between different respiratory motion estimation methods for each subject was performed, in order to determine the agreement between various respiratory motion signals. The motion estimation accuracy was further investigated by reconstructing images with the proposed soft-gating L1-ESPIRiT method. The soft-gating compensation used the same parameters across different motion estimations, including similar effective undersampling factors (which is defined by summing up the weighting values with respect to data size). The image quality was assessed by image sharpness along lung-liver interfaces with the maximum of the first derivative (MD) [96], normalized by the MD value of dynamic 3D self-navigator reconstructed images. Median filter was applied before taking the derivative to mitigate the noise sensitivity. 10 slices were chosen to compute mean and standard deviation for each case.

## Evaluation of Motion Compensated Reconstruction

Soft-gating L1-ESPIRiT was evaluated by first extracting the respiratory motion signals from the acquired data by the proposed 3D dynamic self-navigator ( $80 \times 80 \times 80 \times 1000$  matrix). Then, we used 3D Daubechies wavelet basis with regularization values of  $\lambda = 0.01$  in the soft-gating L1-ESPIRiT reconstruction. The results were compared with gridding reconstruction with and without respiratory motion hard-gating.

For respiratory motion-resolved reconstruction algorithms, the same respiratory navigation signals were used. We divided the data equivalently into 5 motion states (each state has the same number of radial spokes). Regularization values of  $\lambda_1 = 0.01$  and  $\lambda_2 = 0.02$  were empirically tuned and used for reconstruction. [126].

### 4.2.4 Experiments

The proposed methods were applied on two healthy volunteers, nine clinical patients (including 8 cystic fibrosis (CF) patients). All the in vivo studies conducted were approved by my Institutional Review Board (IRB). Image reconstruction and post-processing were carried out by the Berkeley Advanced Reconstruction Toolbox (BART) [127], including gridding and ESPIRiT calibration. In the spirit of reproducible research, I provide both MATLAB (MathWorks, Natick, MA) and Python (PSF, Wilmington, DE) demonstration code ([https://github.com/jiangwenwen1231/FB\\_UTE\\_Recon](https://github.com/jiangwenwen1231/FB_UTE_Recon)) and a software package to reproduce some of the results described in this article. The software can be downloaded from: <https://github.com/mrirecon/bart>.

All of the in vivo 3D UTE scans shared the following relevant parameters: prescribed field of view (FOV) =  $32 \times 32 \times 32$  cm<sup>3</sup>, flip angle =  $4^\circ$ , 1.25 mm isotropic resolution, sampling bandwidth =  $\pm 250$  kHz, readout duration = 1 ms. Gradients were designed to create a maximum shift of  $\pm 125$  kHz across the prescribed FOV. The total scan time was between 5 min 7 s to 5 min 14 s, which results in undersampling ratio  $\approx 8$  with respect to Nyquist criterion when motion is ignored. TE was in the range of  $70 \sim 80$   $\mu$ s and TR was in



the range of 2.932~4.1 ms.

Free-breathing scans were performed on all the subjects with slight different scan details: healthy volunteers were performed on 3T clinical scanners (GE Healthcare, Waukesha, WI) with an 8-channel cardiac coil and 20-channel torso coil arrays; CF patients studies were performed on 1.5T and 3T (GE Healthcare, Waukesha, WI) clinical scanners, an 8-channel cardiac coil and 18-channel torso coil were used as receiver arrays, respectively; the patient with pulmonary nodules was scanned on a 3T PET/MR scanner (GE Healthcare, Waukesha, WI) with a 18-channel torso coil. Respiration bellows belts were in place during all the scans.

## 4.3 Results

### 4.3.1 Evaluation of Dynamic 3D Self-Navigator

Dynamic lower-resolution images have strong streaking artifacts when only the gridding operation was applied, as seen in Fig 4.3, due to a high level of undersampling ( $\sim 200$ -fold) of every frame. It is extremely challenging to estimate motion information from these corrupted images. When parallel imaging and compressed sensing with LLR constraints were applied, the incoherent aliasing artifacts were significantly reduced by the local sparsity constraint. The Supporting Video 1 shows the comparison of gridding and LLR images over time.

To demonstrate the dynamics captured by the dynamic 3D self-navigator, I selected cross lines perpendicular to the diaphragm, front chest wall, at the apex of the lung, as well as within the heart for two subjects with cystic fibrosis, in which complex breathing patterns were observed. In both case 1 and case 2 in Fig 4.3, the dynamic 3D navigators were capable of displaying the full chest motion pattern well, including lung-liver interface displacement, chest wall expanding, as well as movement of pulmonary vessels within the lung. Both subjects had a mixture of deep and shallow breathing patterns with variable rates. I also observed cardiac motion in case 2 on top of respiratory motion as the green line and box show in Fig 4.3. (The full dynamics of cardiac motion is beyond the scope of this work.)

The Supporting Video 2 and Supporting Video 3 clearly illustrate the full respiratory motion captured by the LLR reconstruction on two CF patients with complex breathing patterns.

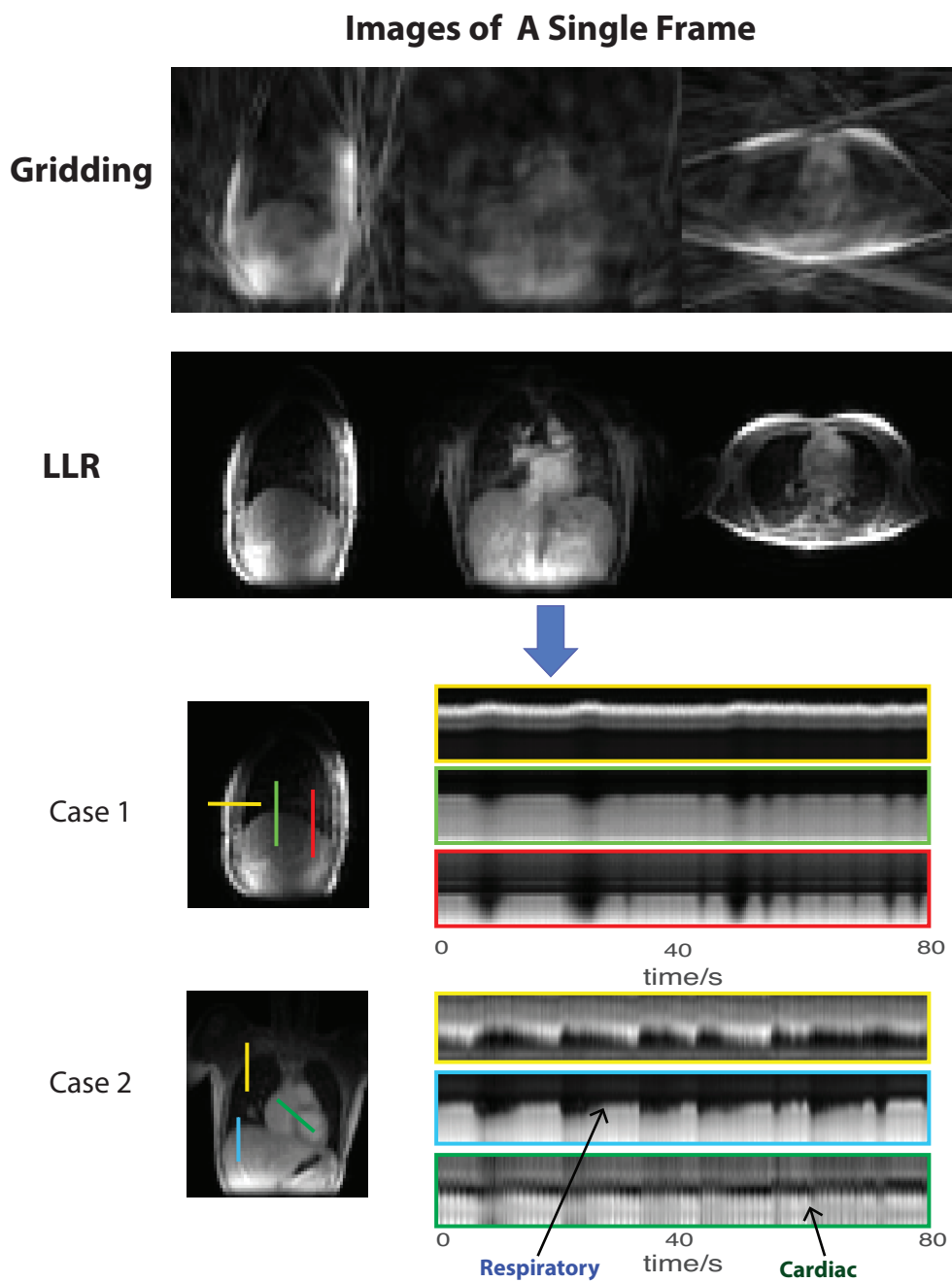


Figure 4.3: Dynamic 3D self-navigator: (top) Comparison of gridding and locally low-rank constrained lower-resolution images as navigators (Please see Supporting Video 1 ); (bottom) Motion measured by the LLR dynamic 3D self-navigator for two subjects with CF in which complex breathing patterns were observed. The cross lines of particular positions over time show multiple directions of chest motion. (Please see Supporting Videos 2 and 3 of these two cases.)

For all the clinical patients, I compared the respiration estimation from the dynamic 3D self-navigator, a DC-based self-navigator, and respiratory bellows belt-based navigation with Pearson correlation coefficient analysis. For the subjects (Case 4,7,8) with regular breathing pattern, respiratory bellow and DC-based self-navigation usually showed good agreement with dynamic 3D navigator based motion estimation. However, there was substantial disagreement for subjects with irregular breathing patterns (Case 1,2,5,6) as shown in the correlation coefficient table of Fig 4.4. I also quantitatively compared the image sharpness of soft-gating L1-ESPIRiT reconstructed images with the metric of maximum derivative. Overall, dynamic 3D self-navigator based reconstructed images provide the best image sharpness. For subjects with regular breathing pattern, different respiration navigation resulted in similar image sharpness (Case 4,7,8). For subjects with irregular breathing pattern (Case 1,2,5,6), dynamic 3D self-navigator based image provide significant better image sharpness than both DC-based self-navigation and respiratory bellow based images.

I show two exemplifications to illustrate different motion estimation signals and corresponding reconstructed images. Fig 4.5 examines the two challenging cases of cystic fibrosis patients who had mildly irregular breathing and strongly irregular breathing, respectively. The Supporting Video 4 shows the breathing pattern of all the clinical patients evaluated in the Fig 4.4.

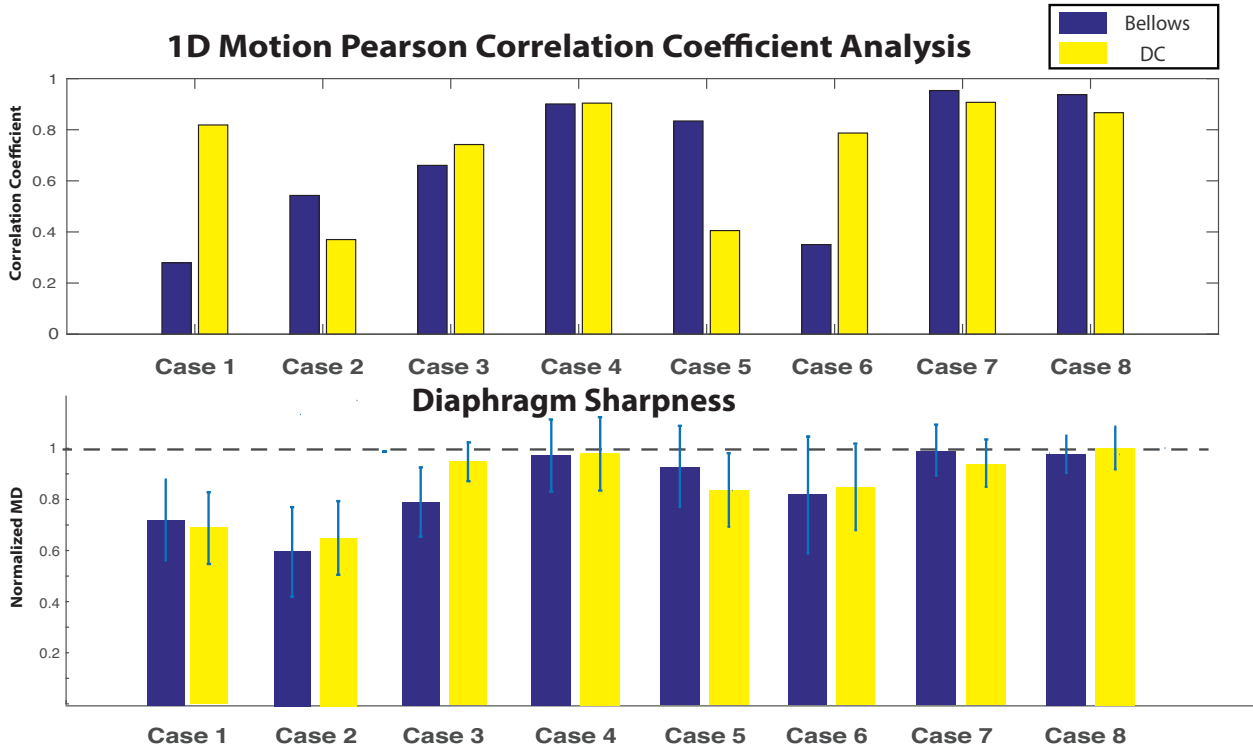


Figure 4.4: (Top) Pearson correlation coefficients between the dynamic 3D self-navigator signal and respiratory bellow signal (blue), and between dynamic 3D self-navigator signal and DC-based self-navigation signal (yellow) among 8 cystic fibrosis patients; (Bottom) Comparison of different respiration estimation methods in 8 cystic fibrosis patients in terms of diaphragm sharpness marked by maximum derivative (MD) method. The values are normalized by the sharpness value of dynamic 3D self-navigator reconstruction.

Case 1, shown in the top of Fig 4.5, had mildly irregular breathing, with periods of regular motion but also some deep/shallow inhalation. Both DC-based self-navigation and dynamic 3D navigator were able to delineate the deep and shallow inhalation ( $\approx 50$  s and 150 s, like shown in shading areas of interest) while the respiratory belt failed to capture this variation. The motion estimation accuracy was evaluated qualitatively by applying a soft-gating L1-ESPIRiT reconstruction in the right column of Fig 4.5. As the yellow arrows show, the sharpness of the small vessels was slightly deteriorated with respiratory belt navigation and DC-based self-navigation, while the dynamic 3D self-navigator most clearly depicts these

fine structures and improves the conspicuity of the small vessels. Although the DC-based self-navigation appeared to correctly capture deep and shallow inhalation has correlated well with dynamic 3D navigator (also indicated in Fig 4.4 with correlation coefficient), the blurred vessels in the reconstructed images indicate some inaccuracies. Also, quantitatively the sharpness of the lung-liver interfaces were analyzed in Fig 4.4. Both belt navigation and DC-based self-navigation resulted in lower sharpness values compared with 3D self-navigator. The 3D self-navigator video are included in the Supporting Video 2.

Case 2, shown in the bottom of Fig 4.5, had a strongly irregular breathing pattern. Differences in the motion estimation results are largely due to the fact that respiratory belt and DC-based self-navigation cannot capture the bulk displacement of the lung and the diaphragm that occurred during this study. During several abrupt movements ( $\approx 20$  s, 70 s and 160 s, like shown in shading areas of interest), the respiration belt failed to match the actual displacement of diaphragm. I suspect this patient was coughing during the first minute of the scan. As the reconstructed images show in Fig 4.5, images reconstructed utilizing DC-based self-navigation and respiratory belt had low vessel conspicuity and substantial blurring observed at the dome of the liver. This suggests both the DC and bellows signals did not accurately represent chest wall and diaphragm motion. The dynamic 3D navigator gating greatly improves the image quality in this case, sharply recovering fine vascular structures within the lung. The significant lower MD values from belt navigation and DC-based navigation of Case 2 in Fig 4.4 also reinforces the analysis. I provide the Supporting Video 3 showing the dynamic 3D navigator for this patient during the 5-minute scan.

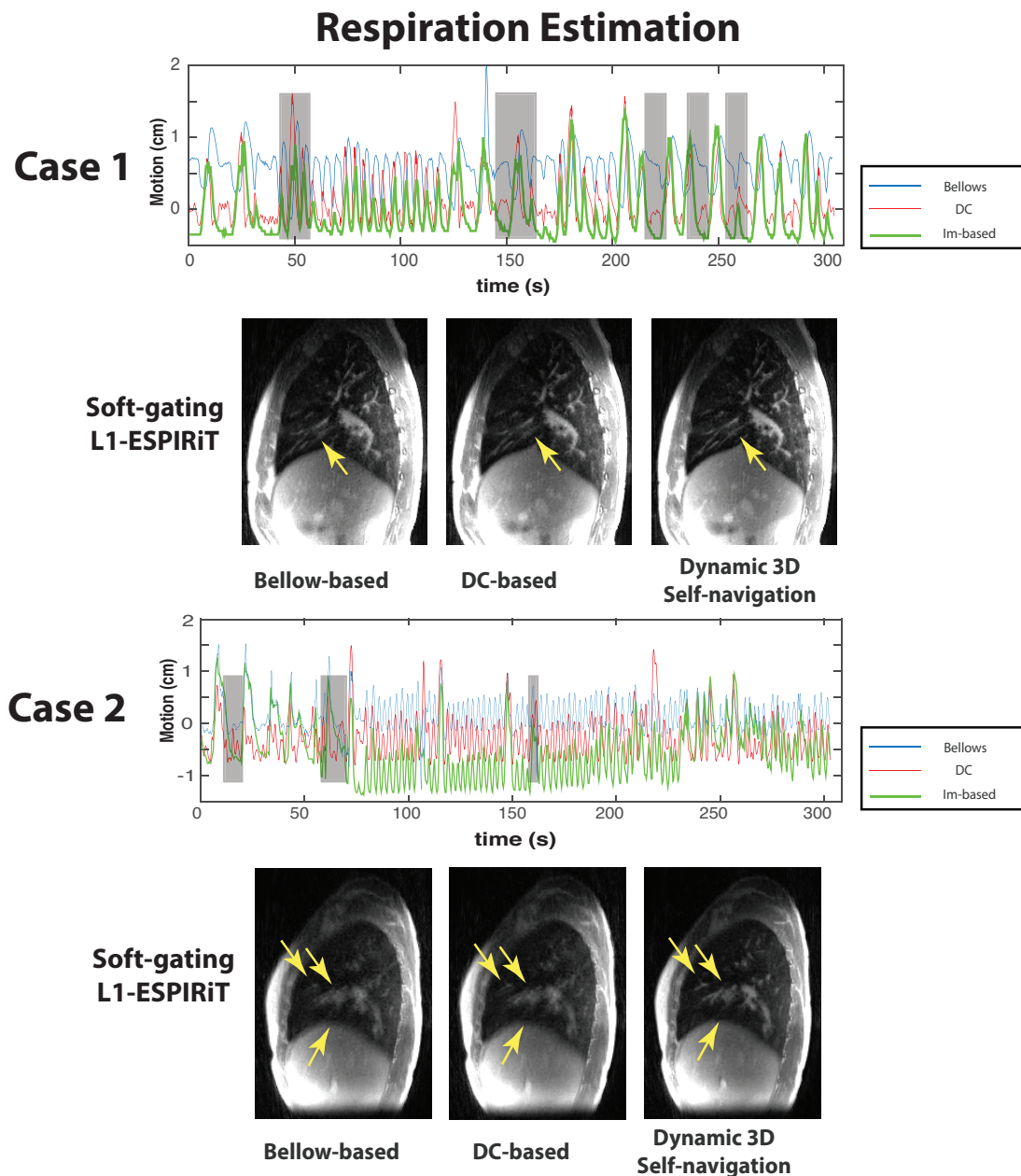


Figure 4.5: Comparison of different respiration estimation methods in **CF patient case 1 with a mildly irregular breathing pattern** and **CF patient case 2 with a strongly irregular breathing pattern**: (top) respiration motion estimated by the respiratory bellows belt; (middle) respiration motion derived from the center of k-space (DC); (bottom) respiration SI motion derived from the dynamic 3D navigator. A comparison of soft-gating L1-ESPIRiT reconstructions based on corresponding respiration estimation is shown on the right. These reconstructions are based on a soft weighting window centered at the end of expiration. The arrows indicate vessels with varying conspicuity based on different respiration estimations. Note that the only dynamic 3D self-navigation signal is quantitative whereas the DC based and bellows are not.

### 4.3.2 Evaluation of Motion Compensated Image Reconstruction

Fig 4.6 shows a comparison of non-gated gridding (left) and gated gridding (middle) reconstructions with the soft-gating L1-ESPIRiT reconstruction (right) in a healthy volunteer and a cystic fibrosis patient. The zoomed-in red boxes show that the fine pulmonary structures are delineated well with soft-gating L1-ESPIRiT. Red arrows point out where vessels and fine structures were blurred out by the respiratory motion when the non-gated reconstruction was used, while gating motion compensation was able to visualize the fine structures and diaphragm. For the gated gridding reconstruction, although the structures are sharper, the undersampling results in streaking artifacts (yellow arrows) and also diffuse aliasing artifacts that are noise-like in appearance. These were removed when soft-gating L1-ESPIRiT was applied. Overall, soft-gating L1-ESPIRiT reconstruction also provides better apparent SNR, since it removes the both streaking and noise-like artifacts while enforcing sparsity in the image wavelet domain.



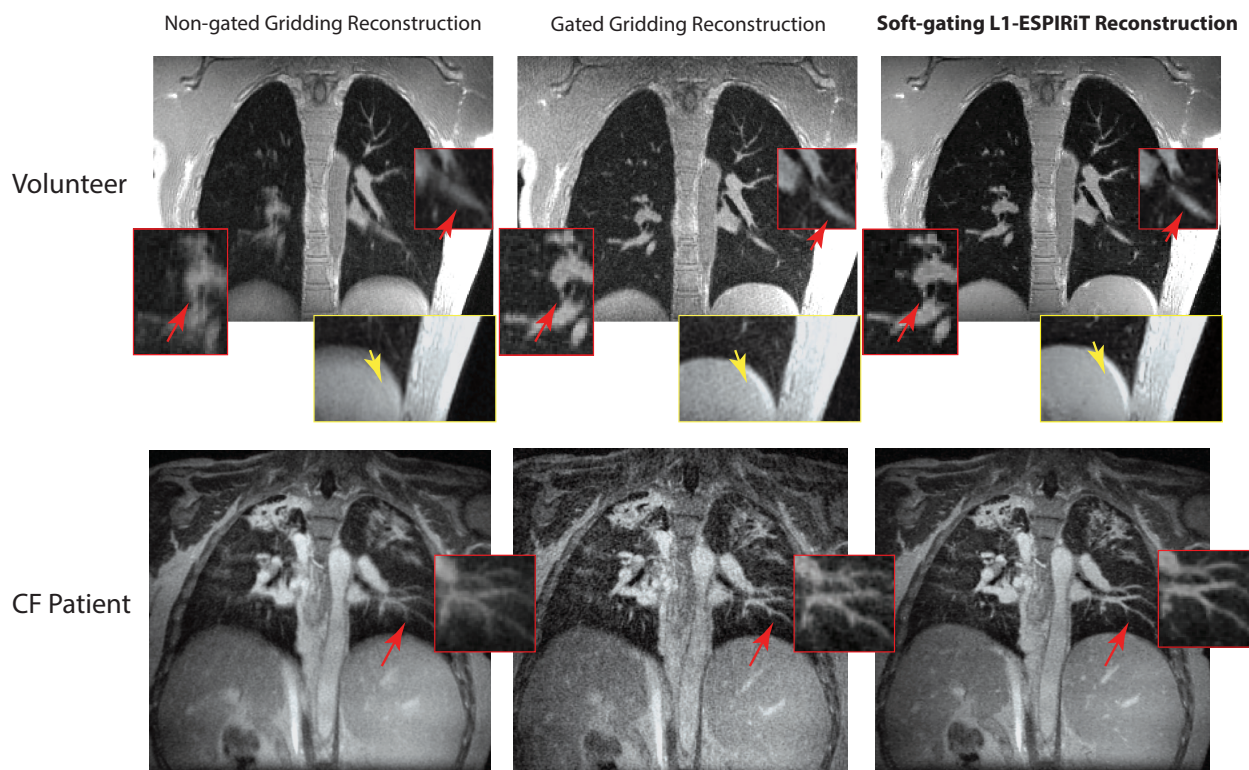


Figure 4.6: Comparison of soft-gating L1-ESPIRiT reconstruction with non-gated and gated gridding reconstructions showing a single coronal slice from a healthy volunteer (top row) and a cystic fibrosis patient (bottom row). Red boxes are zoomed-in views of fine structures, and the yellow boxes show how well the diaphragm and streaking artifacts were resolved.

Fig 4.7 shows the respiratory motion-resolved images of all the respiratory motion-states (from left to right) from the same volunteer as Fig 4.6. They clearly depict respiratory motion without suffering from undersampling-induced aliasing. See the Supporting Video 5 for an animated version of the respiratory motion-resolved images.

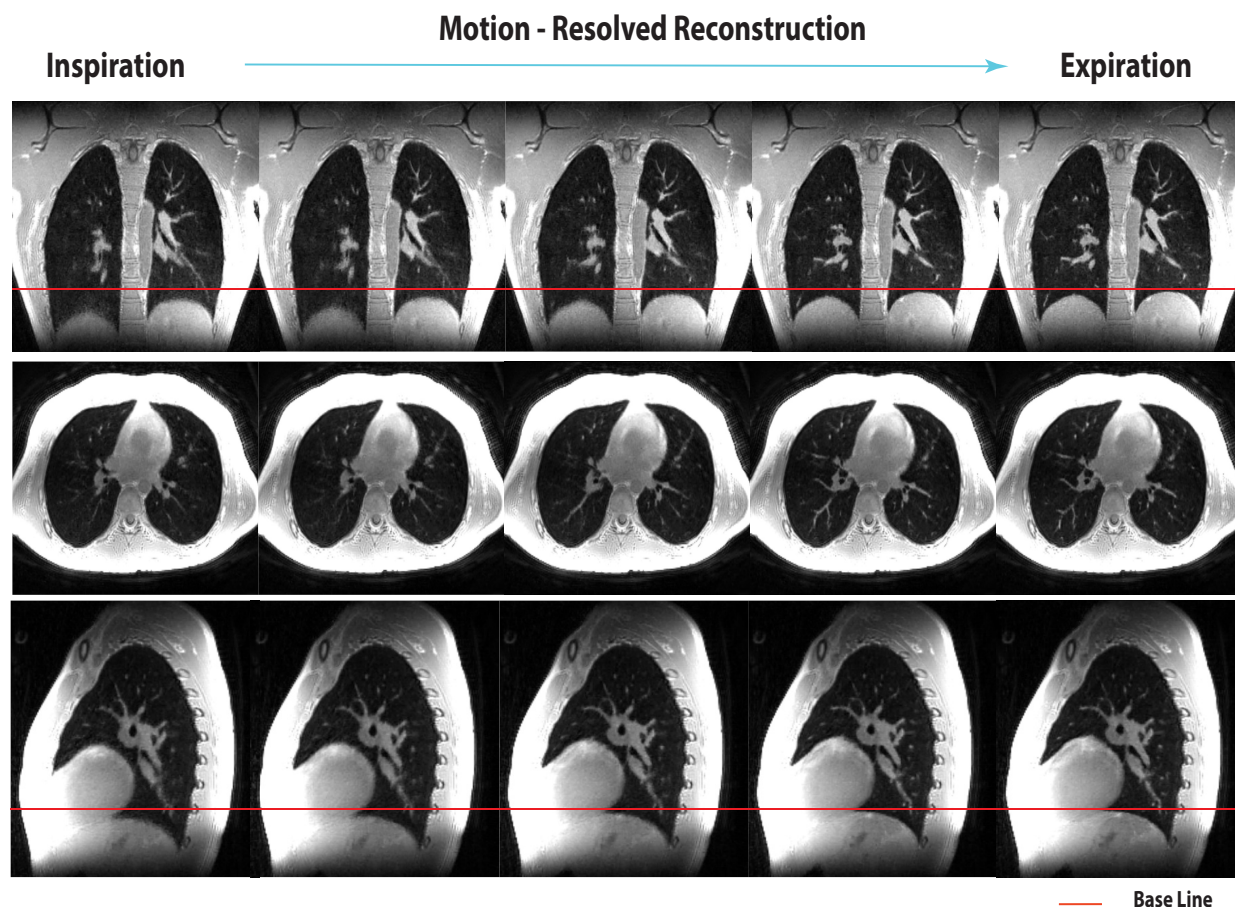


Figure 4.7: Respiratory motion-resolved L1-ESPIRiT reconstruction (images of different motion states are displayed from left to right). Please see the Supporting Video 5 for animated version of this result. The red line denotes the location of the diaphragm at end expiration.

Fig 4.8 shows a side-by-side comparison of the soft-gating and respiratory motion-resolved reconstructions on the same volunteer. Both soft-gating and respiratory motion-resolved techniques were able to significantly reduce motion blurring and artifacts due to under-sampling. The two reconstructions have similar apparent image quality. While respiratory motion-resolved imaging provides all the motion states that could be valuable for dynamic evaluations (e.g. ventilation, air trapping), the soft-gating reconstruction is computationally more efficient. In this comparison carried out on a machine equipped with a four-

socket Intel Xeon E7-8870 with a total of 144 cores at 2.10GHz, my implementation of the motion-resolved L1-ESPIRiT reconstruction takes 156GB memory and 5 hours with the parallelized implementation, while soft-gating reconstruction takes 43GB and 2 hours on the same dataset.

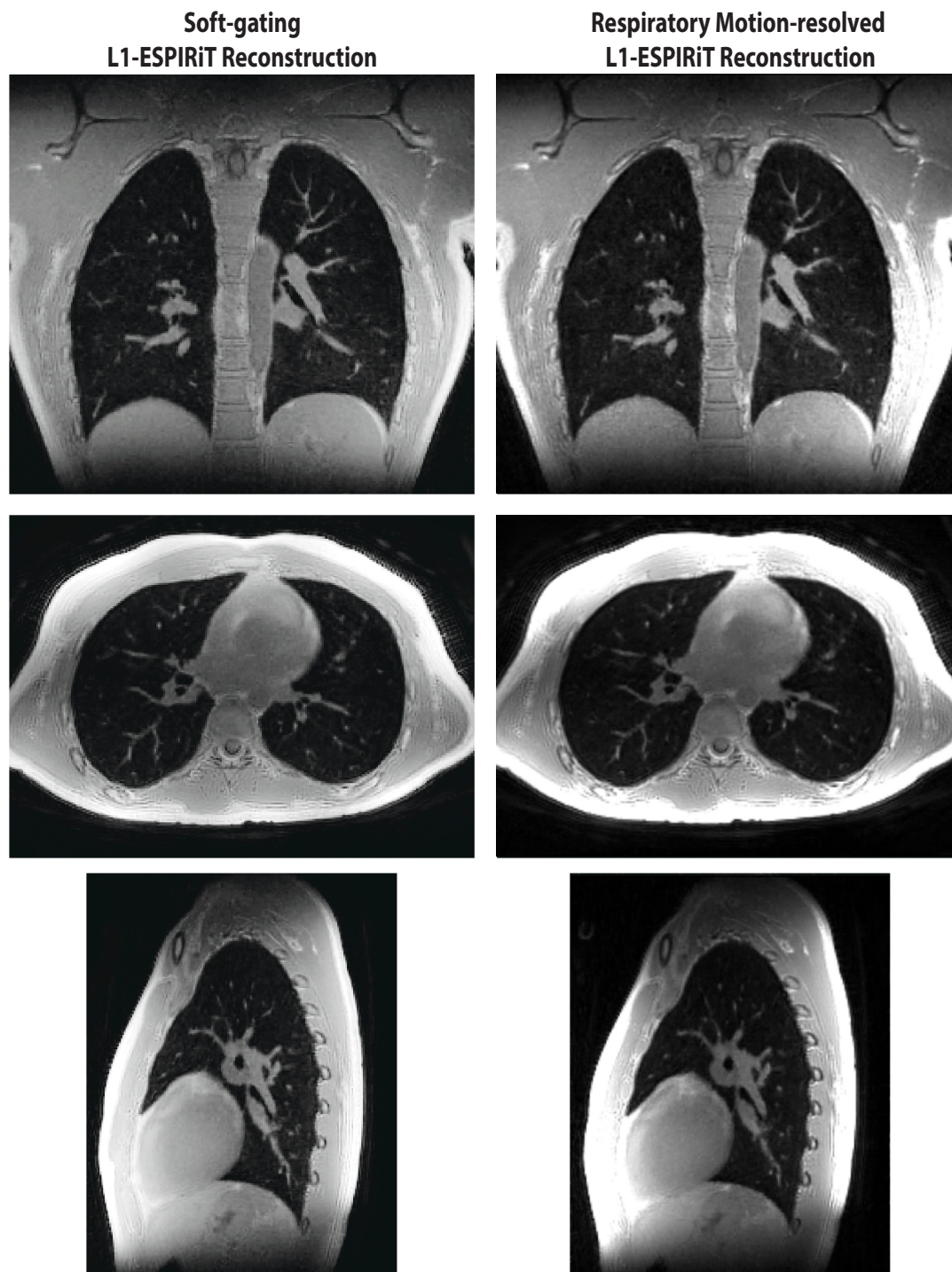


Figure 4.8: Comparison of soft-gating and respiratory motion-resolved L1-ESPIRiT reconstructions at end-expiration in a healthy volunteer.

To illustrate the performance of the motion compensated reconstructions in a subject with irregular breathing, Fig 4.9 shows a side-by-side comparison of the soft-gating and respiratory motion-resolved reconstructions for the CF patient Case 2 (same with Fig 4.5). This subject had a strongly irregular breathing pattern and respiration drifts. Although the soft-gating technique was able to significantly reduce motion blurring and recover most of the vascular structures conspicuity within the lung, it resulted in blurring of some features (e.g. diaphragm and vessels, shown with yellow arrows). Due to the large variation of the respiratory motion and drifts, especially during inspiration state, I kept 60% of the data as shown in Fig 4.9 and then segmented the remaining data equally into 5 motion states to perform respiratory motion-resolved reconstruction. This respiratory motion-resolved reconstruction was able to delineate the small pulmonary vessels and sharp diaphragm, without deteriorating image quality. This is because each respiratory motion state represents smaller motion range compared with the soft-gating technique's single motion state.

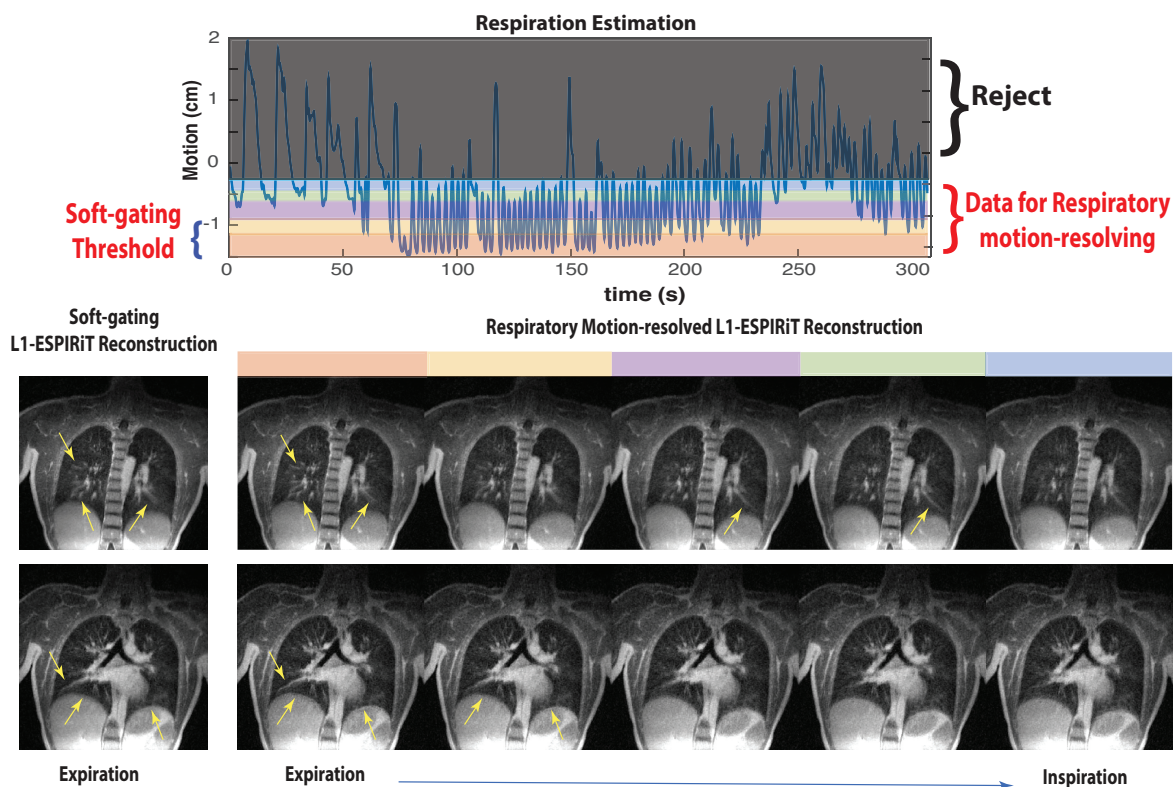


Figure 4.9: Comparison of soft-gating L1-ESPIRiT at end-expiration and respiratory motion-resolved L1-ESPIRiT reconstruction in a CF patient with strongly irregular breathing and respiration drifts (also shown in Fig 4.5 and Supporting Video 3). Due to the large variation of the respiratory motion and drifts, I kept 60% of the data as shown above and then performed respiratory motion-resolved L1-ESPIRiT reconstruction on the remaining data. Yellow arrows point out the features that still suffered from blurring artifacts with soft-gating, while the respiratory motion-resolved method was able to delineate the small pulmonary vessels and provide a sharp diaphragm.

## 4.4 Discussion

In this work, I present a motion robust method for high-resolution 3D pulmonary MRI. It is based on an optimized 3D UTE sequence and a free-breathing 5-minute acquisition. The proposed methods include dynamic 3D images for self-navigation and motion estimation along with soft-gating L1-ESPIRiT and respiratory motion-resolved L1-ESPIRiT for robust motion compensated image reconstruction. With the proposed techniques, I have demonstrated many pulmonary structures are well delineated with good SNR, and overall improved image quality compared with traditional reconstructions.

### 4.4.1 Dynamic 3D Self-navigator

The proposed lower-resolution dynamic 3D self-navigator utilizes locally low-rank constraints to reconstruct dynamic images from highly undersampled data. The resulting images can be used to robustly extract volumetric motion information of the entire chest. For patients with regular breathing patterns, I found that self-navigation based on DC signals provided similar gating quality compared with dynamic 3D navigator self-navigation. However, for patients with any irregular breathing or bulk motion, the dynamic 3D navigator was necessary to estimate the true motion. Being able to compensate for irregular breathing with the proposed method is critical for clinical pulmonary imaging applications, as these patients are more likely to have difficulty breathing regularly.

With the proposed lower-resolution dynamic 3D navigator, I only use it to estimate superior/inferior translation of the diaphragm. However, there is unexplored abundant motion information that could be estimated. With more comprehensive motion information, I could integrate the proposed 3D navigator with a more explicit motion compensation model. In this sense, the dynamic 3D navigator is not limited to respiratory motion estimation and can also be applied to cardiac motion estimation as suggested in Fig 4.3.

The lower-resolution 3D images may also provide additional diagnostic information about respiratory mechanics, including ventilation and air trapping [128].

In addition, the proposed 3D navigator is not limited to 3D radial trajectory with bit-reversed pseudo-random ordering that was used in this study. It is easily translatable to other pseudo-random ordering schemes, like multi-dimensional golden angle ordering or other 3D trajectories, like 3D cones or radial-cones[110, 129, 130, 131].

#### 4.4.2 Soft-gating versus Respiratory Motion-resolved Method

The respiratory motion-resolved approach provides 4D results (3D spatial + motion-states), allowing comprehensive evaluations of pulmonary function such as ventilation and air trapping. Its primary limitation is that it is computationally expensive. In terms of the selection of the two regularization parameters:  $\lambda_1$  and  $\lambda_2$ , Fig 4.10 shows motion-resolved reconstruction results for six representative regularization combinations. Both  $\lambda_1$  of the Wavelet sparsity and  $\lambda_2$  of the motion states sparsity help to suppress undersampling aliasing artifacts.  $\lambda_1$  promotes 3D spatial sparsity, effectively removing aliasing artifacts (shown in the top row of Fig 4.10). Usage of additional sparsity constraint along the additional respiratory-state dimension improved the removal of undersampling artifacts (shown in the second row of Fig 4.10 ). Nonregularized case (  $\lambda_2 = 0$  ) resulted in residual aliasing artifacts (the first figure in the second row), while very high values of  $\lambda_2$  introduced blurring over respiratory motion states (the last figure in the second row). In practice, the way I tune for the appropriate parameters is to set  $\lambda_2$  to be zero and choose appropriate spatial sparsity  $\lambda_1$  first. Then adding  $\lambda_2$  to improve the undersampling aliasing removal but keep motion states fidelity.

In the comparison of Fig 4.8, the respiratory motion-resolved method resulted in a slightly lower apparent SNR by subjective visual inspection than soft-gating method for the volunteer study. That might be because the effective data sampling efficiency (about 40%, which is given by summing up the weighting values with respect to data size) of soft-gating is higher than a single state (20%) in the respiratory motion-resolved method. It could also be related to regularization parameter, which is different in the two reconstructions. Since the respiratory-motion resolved reconstruction has additional temporal constraints, it is hard to



make a fair comparison.

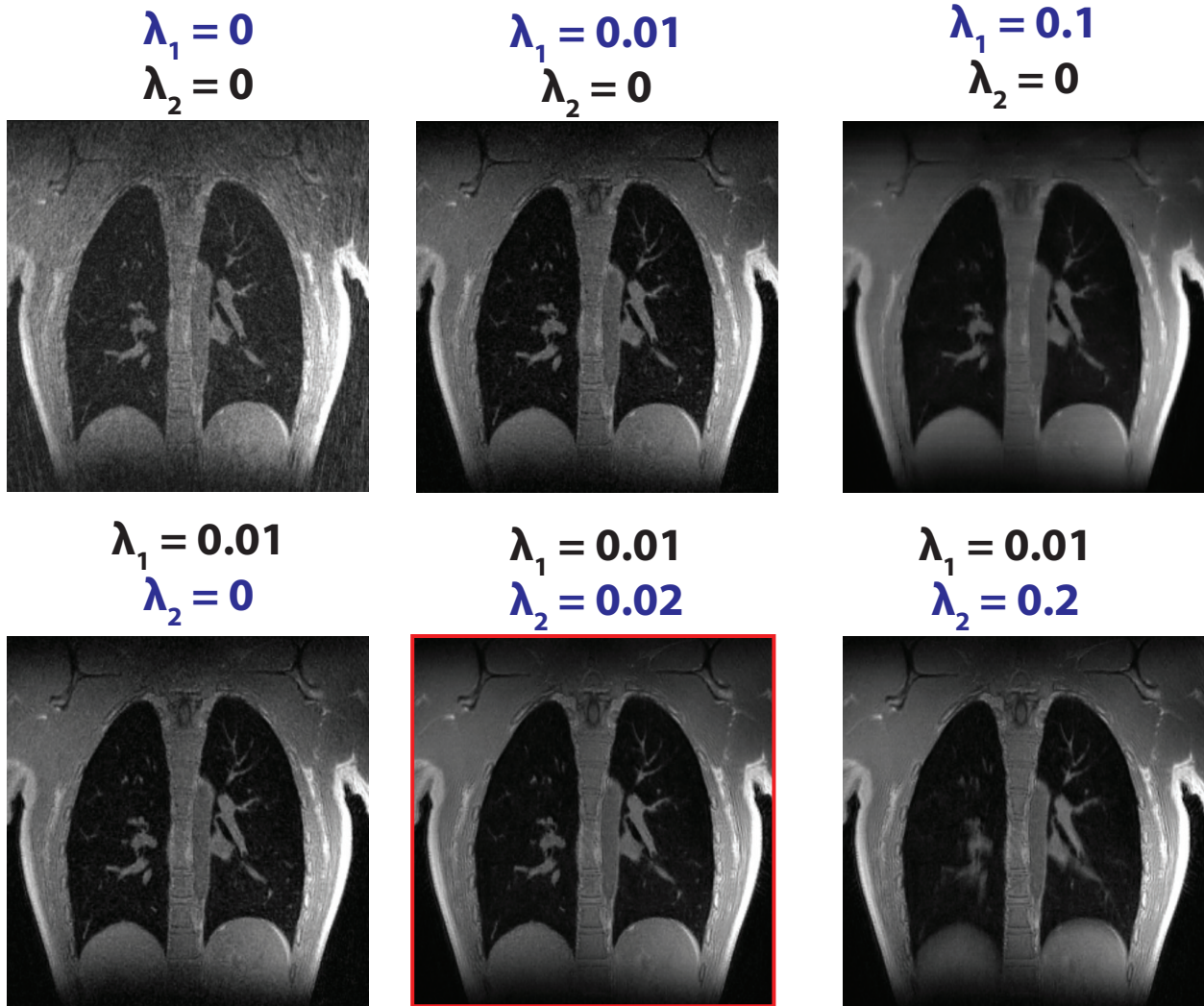


Figure 4.10: Respiratory motion-resolved reconstruction results for representative regularization parameters combinations on a healthy volunteer.  $\lambda_1$  (Wavelet sparsity) promotes 3D spatial sparsity, effectively removing aliasing artifacts (shown in the top row). Usage of additional sparsity constraint along the additional respiratory-state dimension ( $\lambda_2$ ) improved the removal of undersampling artifacts (shown in the second row). Very high values of  $\lambda_2$  introduces blurring over respiratory motion states (shown in the last figure of the second row).

When relatively more time is spent in a single respiration motion state, as often occurs at end expiration, the soft-gating reconstruction is a practical choice to provide a high-quality image of that motion state, with reduced computational requirements. In some cases with irregular breathing patterns or drifts, motion blurring may still remain for soft-gating respiratory when the data below the threshold has experienced a large motion range. The motion-resolved reconstruction could provide improved results when each motion state data experiences less motion if they are carefully chosen. Both methods benefit from the quantitative and accurate estimation of the respiratory motion from the dynamic 3D self-navigator.

#### 4.4.3 Feasibility in in Cystic Fibrosis and Pulmonary Nodules

I also evaluated feasibility of the pathologies of cystic fibrosis and pulmonary nodules. Top row of Fig 4.11 shows exemplary pathologies in cystic fibrosis that were well visualized when using the soft-gating L1-ESPIRiT reconstruction. The left case shows atelectasis along the major fissure as the red arrow shows, and the middle and right cases show bronchiectasis. The middle case also shows mucus plugging, shown in the red circle. The air trapping is seen in the left lower lobe in the right case as the red arrow shows. These demonstrate the potential of the proposed approach to depict clinically relevant imaging features in the lung. Bottom row of Fig 4.11 shows clinical examples of a 3 mm, 5 mm and 1 cm pulmonary nodules (green circles) when using the soft-gating L1-ESPIRiT reconstruction. The 3 mm nodule was an incidental finding from a volunteer study. This approach is able to depict a range of nodule sizes, shapes, and contrast as shown in these examples.

The above results were preliminary results. Future clinical studies will be needed to evaluate the efficacy of the proposed method to these pathologies thoroughly.

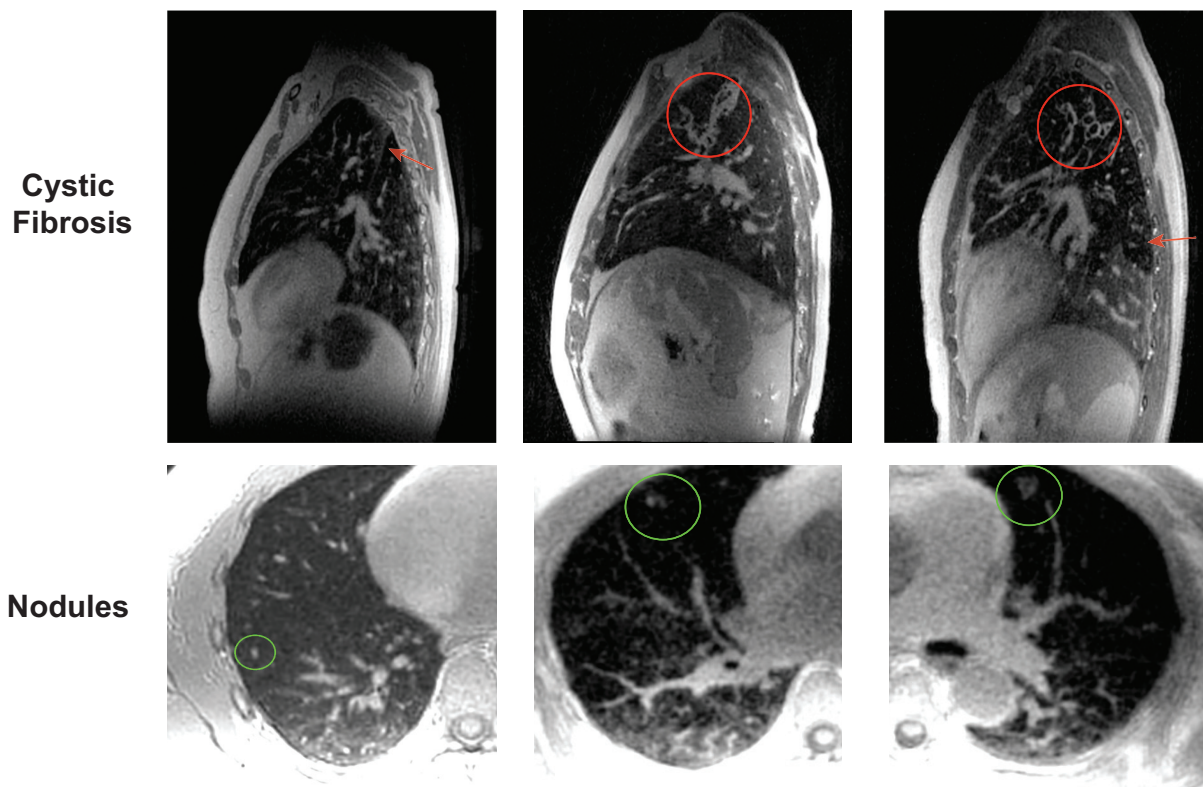


Figure 4.11: Top: soft-gating L1-ESPIRiT reconstruction in cystic fibrosis patients at end expiration: atelectasis (in the left case) along the major fissure, bronchiectasis and mucus plugging (in the middle case), bronchiectasis and air trapping (in the right case). Bottom: soft-gating L1-ESPIRiT reconstruction showing 3 mm, 5 mm and 1 cm pulmonary nodules in different subjects.

## 4.5 Conclusion

In this work, I have achieved motion robust high resolution 3D pulmonary imaging with MRI. I developed a method based on five-minute free-breathing scan using an optimized 3D radial UTE sequence and a dynamic 3D self-navigator for motion estimation, combined with state-of-the-art motion compensated reconstructions. This method was able to effectively eliminate motion artifacts even in the presence of strongly irregular breathing patterns, and reconstruct aliasing artifact-free images from highly undersampled data.

# Chapter 5

## Estimation of Gradient Delays in non-Cartesian Parallel MRI

### 5.1 Introduction

Non-Cartesian imaging is susceptible to gradient fidelity errors, such as those due to gradient delays and eddy currents. The gradient timing errors usually result in spurious geometric image distortions. Moreover, misaligned k-space data corrupts the k-space data which is used for parallel imaging auto-calibration.

These gradient errors can be corrected by separate calibration measurements of physical gradient timing delays [132, 133] or more sophisticated measurements of actual gradient waveforms [134, 135, 136]. This requires an additional acquisition that depends on the experimental SNR. In addition, these methods assume that the errors are consistent between calibration and acquisition, which may not be an accurate assumption due to phenomena such as gradient coupling or patient motion [137]. Magnetic field monitoring is another kind of measurement approach that uses NMR probes placed around the imaging volume in the scanner [138, 139]. The main disadvantage of this method is that it requires specialized hardware.

There have been efforts to correct for gradient errors retrospectively without additional calibration measurements or hardware [137, 140, 141, 142, 143]. Recently, a number of promising works [137, 142, 143] have shown that promoting self-consistency inherent in neighboring multichannel k-space measurements can correct for trajectory errors, without separate trajectory calibration scans. There are two GRAPPA operator [144] based methods [137, 142] for correcting radial trajectory errors. Deshmane *et al.* proposed a GROG method [137] maximizing DC signals and Wech *et al.* proposed the SCITA method [142] maximizing mutual accordance of data. However, both of these methods cannot be readily extended beyond radial trajectories, as they have to specify the shift directions. Ianni *et al.* further proposed a more general approach, TrACR [143], to jointly estimate trajectory errors and images. This method is based on SENSE and SPIRiT parallel imaging reconstructions, and requires additional delay-free calibration Cartesian images to obtain either accurate sensitivity maps or accurate SPIRiT kernels.

In this work, I propose a gradient delay estimation method that is general to non-Cartesian trajectories with multichannel datasets. Unlike previous methods, it does not require prior GRAPPA/SPIRiT calibration or any prior direction specifications. I make use of the observation that uncorrupted multichannel data inherently lives in low dimensional subspace [29, 30, 31, 145] and data corruption induces inconsistencies that violate this property. Hence, I solve directly for the gradient delay corrections that result in consistent low-dimensional calibration data.

The proposed method is based on a calibrationless parallel imaging method – SAKE [145] – which is exploiting the low dimensional subspace property of the calibration data. This property has also been used to correct EPI ghosting [146]. I formulate the joint estimation problem as a low-rank constrained problem, using a Gauss-Newton method to solve for the gradient delay values and auto-calibration data.

## 5.2 Theory

### 5.2.1 Low Rank Property in Parallel Imaging

Parallel imaging reconstruction is enabled by the correlations between multichannel k-space data due to sensitivity maps. The correlations within multichannel k-space data can be exploited by constructing a block-Hankel matrix from a calibration region [145]. Typically, a fully sampled region in the center of k-space, the auto-calibration (AC) region, is used to perform the calibration. By sliding a window throughout the AC data, I can construct a calibration matrix, denoted  $A = HFx$ , where  $H$  is the block-Hankel structured operator,  $x$  is the multichannel low resolution image of auto-calibration region, and  $F$  is the multichannel Fourier transform operator of the auto-calibration region. The columns of  $A$  are shifted blocks of the AC area shown in Fig 5.1, leading to a matrix structure known as block-Hankel. Under the reasonable assumption that coil sensitivities are smooth in space with compact k-space support, it has been shown that a calibration matrix  $A$  has low rank as well analyzed in SAKE [145].

SAKE seeks to reconstruct a full k-space from undersampled, multichannel dataset using a structured low-rank matrix completion method, formulated in Equation 5.1.

$$\begin{aligned}
 & \text{minimize} && \|Dx - y\|_2^2 \\
 & \text{subject to} && A = HFx \\
 & && \text{rank}(A) = k
 \end{aligned} \tag{5.1}$$

where  $D$  is the undersampled multichannel Fourier transform operator.

Instead, I try to exploit this low-rank property of the auto-calibration matrix to estimate gradient delays of non-Cartesian data. The basic idea behind the proposed method is to find the gradient delay that maximizes the self-consistency of neighboring k-space points in multichannel datasets.

## 5.2.2 Solve for Gradient Timing Delays with Low Rank Constraints

For non-Cartesian imaging, gradient delays usually cause inconsistent deviations in k-space between encodings. My hypothesis is that this inconsistent trajectory deviation results in a calibration matrix with a higher rank. Motivated by this hypothesis, I formulate solving for gradient delays into an optimization problem with low-rank constraints. Upper bound on the rank of the structured matrix is well analyzed by [145], thus can be regarded as a known parameter beforehand.

For simplicity, I assume the central k-space data is fully sampled, so I can ignore under-sampling effect. This assumption holds for most non-Cartesian trajectories, such as radial, spiral, even with overall undersampling for parallel imaging. Further discussion of under-sampling effect on the proposed method is described in the Discussion section. In addition, I assume timing delays for the gradient axes are independent but the same across all encodings in a single scan.

### Notation

$\Delta(\vec{t})$  : estimated delays on different axes

$x_i$  : low resolution image of auto-calibration region from  $i$ th coil

$y_{ij}$  : cropped k-space data for calibration from coil  $i$ , non-Cartesian encoding  $j$

$D_j$  : multichannel non-uniform fast Fourier transform (NUFFT) operator at encoding  $j$ , parameterized by  $\Delta(\vec{t})$

$F$  : multichannel fast Fourier transform operator (FFT)

$H$  : linear operator that constructs a block-Hankel structured calibration matrix from corresponding k-space data

$N_c$  : the total number of coils

$N_p$  : the total number of encodings (e.g. projections for radial, interleaves for spirals)

$k$  : the rank of the data matrix, known a priori [145], which is bounded by block size and



coil bandwidth

### Problem description

The proposed method can be described by reformulating the Equation 5.1 into the following format:

$$\begin{aligned}
 & \underset{\Delta(\vec{t}), x}{\text{minimize}} && \sum_{j=1}^{N_p} \sum_{i=1}^{N_c} \|D_j(\vec{t} + \Delta(\vec{t}))x_i - y_{ij}\|_2^2 \\
 & \text{subject to} && A = HFx \\
 & && \text{rank}(A) \leq k
 \end{aligned} \tag{5.2}$$

### Algorithms

In every iteration, I performed alternating minimizations between data consistency and low-rank projection (illustrated in Fig 5.1).

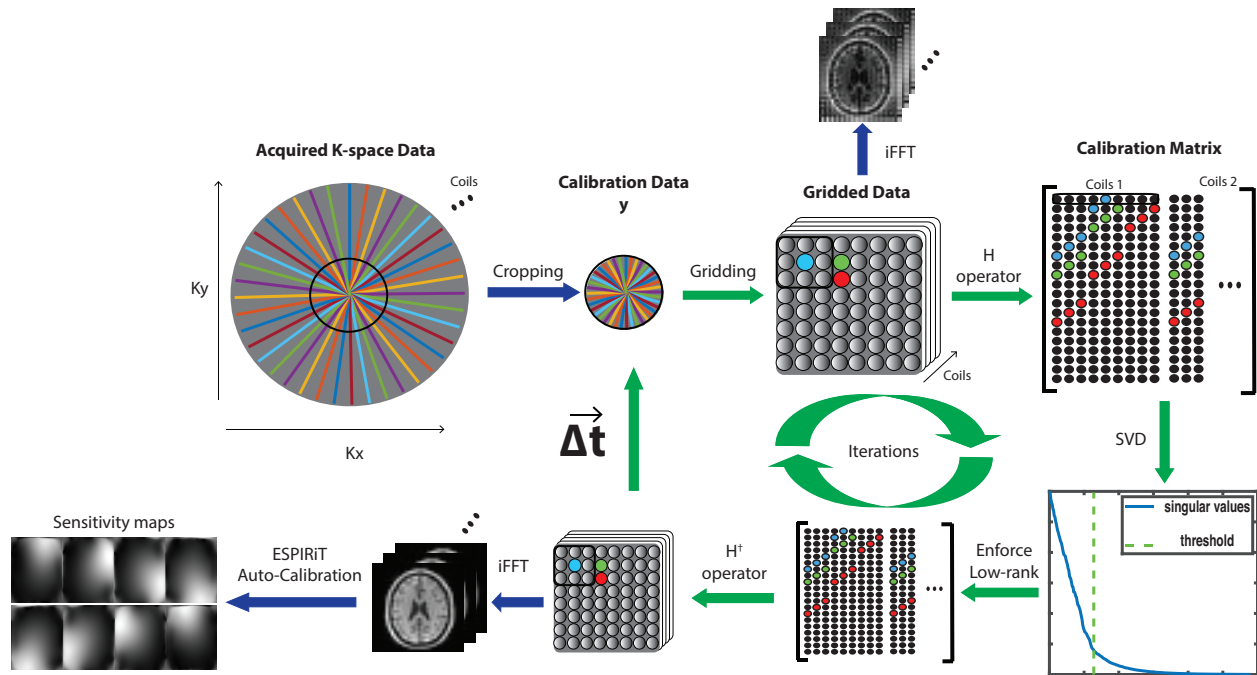


Figure 5.1: Illustration of the proposed method: the gradient delay is estimated iteratively using the AC region. In each iteration, the non-Cartesian data is gridded and then formed into a block-Hankel structured calibration matrix ( $H$ ). Low-rank constraints are applied on the calibration matrix. It is then reformatted to Cartesian data followed by the operation that transforms Cartesian data into non-Cartesian data. In the last step, the Gauss-Newton algorithm is applied to calculate the delay values for each axis.

Firstly, I fix the gradient delay  $\Delta(\vec{t})$  and solve for the coil images  $x_i$ ,

$$\begin{aligned}
& \underset{x}{\text{minimize}} && \sum_{j=1}^{N_p} \sum_{i=1}^{N_c} \|D_j(\vec{t} + \Delta(\vec{t}))x_i - y_{ij}\|_2^2 \\
& \text{subject to} && A = HFx \\
& && \text{rank}(A) \leq k
\end{aligned} \tag{5.3}$$

A low-rank projection method is used to approximate the solution of  $x$ , which is performed by hard-thresholding singular values of the data matrix:

$$\begin{aligned}
A &= HFD^\dagger(\vec{t} + \Delta(\vec{t}))y \\
U\Sigma V^T &= \text{SVD}(A) \quad \% \text{ perform SVD} \\
A &= U_{\|\Sigma_k\|} V_{\|\|}^T \quad \% \text{ hard threshold singular values} \\
x &= F^\dagger H^\dagger(A)
\end{aligned}$$

where  $\dagger$  denotes the pseudo inverse operator.

After solving for  $x$ ,  $\Delta(\vec{t})$  is approximately solved by using Gauss-Newton's method with a first-order approximation:

$$\underset{\Delta(\vec{t})}{\text{minimize}} \quad \sum_{j=1}^{N_p} \sum_{i=1}^{N_c} \|D_j(\vec{t} + \Delta(\vec{t}))x_i - y_{ij}\|_2^2 \tag{5.4}$$

Concretely, the following first order approximation expansion of the NUFFT operator  $D$  is used in Gauss-Newton's method :

$$\begin{aligned}
D_j(\vec{t} + \Delta(\vec{t})) &\approx D_j(\vec{t}) + \Delta(\vec{t}) \cdot \nabla \vec{D}_j \\
&= D_j(\vec{t}) + \begin{bmatrix} \Delta(t_x) & \Delta(t_y) \end{bmatrix} \begin{bmatrix} \frac{\partial D}{\partial t_x} \\ \frac{\partial D}{\partial t_y} \end{bmatrix}
\end{aligned} \tag{5.5}$$

The gradient of the NUFFT operator  $\nabla \vec{D}$  in Equation 5.5 can be calculated by using the derivative property of Fourier transform [147], that is, applying a linear ramp filter in image domain and then performing the forward NUFFT operation. Equation 5.5 describes the 2D

scenario to solve gradient timing delays on the x and y axes, and it can easily extended into a 3D scenario.

This approximation results in the following closed form to solve for  $\Delta(\vec{t})$ :

$$\underset{\Delta(\vec{t})}{\text{minimize}} \quad \sum_{j=1}^{N_p} \sum_{i=1}^{N_c} \left\| \left( D_j(\vec{t}) + \Delta(\vec{t}) \cdot \nabla \vec{D}_j \right) x_i - y_{ij} \right\|_2^2 \quad (5.6)$$

$$\Delta(\vec{t}) = \begin{bmatrix} \Delta(t_x) \\ \Delta(t_y) \end{bmatrix} = \text{Re} \left[ \frac{(\nabla \vec{D}_j x_i)^T \cdot (y_{ij} - D_j x_i)}{(\nabla \vec{D}_j x_i)^T (\nabla \vec{D}_j x_i)} \right] \quad (5.7)$$

The gradient time delays  $\Delta(\vec{t})$  can then be used to update k-space coordinates  $k_x$  and  $k_y$  for the next iteration. If the k-space analytic expression is not known, then interpolation can be used to update the k-space coordinates in practice. The pseudo code is as follows in Table 5.1:

Table 5.1: Pseudo-code for Auto-calibration for Delays

Inputs :	$y$ : cropped k-space data for calibration region from all coils $D/D^\dagger$ : forward and pseudo inverse NUFFT operators $F/F^\dagger$ : forward and inverse FFT operators $H/H^\dagger$ : linear operator that constructs a block-Hankel structured calibration matrix, from corresponding k-space data, and its pseudo inverse operator
Outputs:	$\Delta(\vec{t})$ : estimated delays at different axes $x$ : multichannel image from auto-calibration region
Initiation: $\Delta(\vec{t}) = [0, 0]^T$ while (increment $\geq$ tolerance) { $A = HFD^\dagger(\vec{t} + \Delta(\vec{t}))y$ $U\Sigma V^T = SVD(A)$ $A = U_{\parallel} \Sigma_k V_{\parallel}^T$ $x = F^\dagger H^\dagger A$ $\Delta(\vec{t}) = \text{Re} \left[ \frac{(\nabla \vec{D} x)^T \cdot (y_{ij} - D x)}{(\nabla \vec{D} x)^T (\nabla \vec{D} x)} \right]$ With $\Delta(\vec{t})$ , update k-space trajectory and hence the $D$ operator. }	

## 5.3 Methods

**Reconstruction and Data Processing** Image reconstruction and post-processing were carried out by Berkeley Advanced Reconstruction Toolbox (BART), including non-uniform fast Fourier Transform (NUFFT), and ESPIRiT calibration. All reconstructions and simulations were performed on a laptop equipped with an Intel Core i7 CPU (2 GHz, Santa Clara, CA) with 8GB RAM. Studies were conducted on a 7.0 T GE clinical scanner (GE Healthcare, Waukesha, WI, USA.) with 32-channel head coil and 3.0 T clinical scanner (Philips Healthcare, Best, Netherlands) with 16-channel torso coil. Spiral dataset was acquired from RTHawk real-time environment (HeartVista, Inc., Menlo Park, CA) with 8-channel head coil on a 1.5 T GE clinical scanner (GE Healthcare, Waukesha, WI, USA). All the volunteer studies conducted were approved by the IRB.

In the spirit of reproducible research, I provide a MATLAB demonstration code to reproduce some of the results described in this article <https://github.com/jiangwenwen1231/DelayRecon>.

### 5.3.1 Simulation Validation

To validate the algorithm, simulations on a  $256 \times 256$  brain image with 8-channel simulated sensitivity profiles were performed, both of which can be downloaded from ISMRM 2015 Sunrise Course on The Image Reconstruction Pipeline: <http://gadgetron.sf.net/sunrise>. The simulation was performed using 2D center-out radial (trapezoid waveforms with ramp up sampling), projection reconstruction (PR) trajectory (full-spoke) and multi-shot time-optimal spiral [148] trajectory. The center-out radial trajectory comprised 804 radial spokes, each containing 256 readout points. PR trajectory included 402 projections and each projection has 380 readout points. Spiral trajectory comprised 60 interleaves, each with 1182 readout points. Gaussian white noise was added. To validate the proposed method, I artificially created delays in x and y gradient axes individually, each ranging from ranging from -2

to 2 samples, to generate corrupted k-space data. Here I denote the positive gradient delay as the time delay from the start of ADC window to the start of readout part of played-out gradient waveform.

Images were reconstructed with the nominal trajectory as well as the corrected coordinates estimated by the proposed method. In addition, the estimated delays were compared to the ground truth. The sensitivity maps were computed by ESPIRiT [31].

For different trajectories, the study was repeated for white matter SNR values of 50, 25, and 5 in order to validate the robustness of the proposed method against noise. Each experiment was repeated 10 times to compute the mean and standard deviation of the estimated delay values.

The auto-calibration region was  $36 \times 36$  and block size was  $6 \times 6$ . The rank threshold was chosen to be 64. From non-Cartesian data to the gridded data step, I used iterative gridding based operations to avoid density compensation inaccuracy. The algorithm was stopped after reaching a increment shift size of 0.001 sample.

### 5.3.2 Phantom and In Vivo Experiments for Center-out Radial Trajectory

In order to evaluate the performance of the proposed method, I performed a 2D RF-spoiled radial FLASH sequence scan on a sphere phantom first and then in vivo using the same acquisition. A slice-selective pulse was used for excitation and trapezoid waveforms was played out on the readout gradients, which were x and y axes in the experiments. Then, I introduced different delay combinations on x and y gradient axes, ranging from  $-8 \mu\text{s}$  to  $8 \mu\text{s}$ . The following prescribed parameters were used: flip angle =  $4^\circ$ , FOV =  $20 \times 20 \text{ cm}^2$ , in-plane resolution =  $1 \times 1 \text{ mm}^2$ , TE/TR = 3.4 ms/ 2 s, readout bandwidth =  $\pm 125 \text{ kHz}$  ( $4 \mu\text{s}/\text{sample}$ ), and 628 spokes were acquired. The total scan time was 2 min 56 s. There were 15 samples on the ramp for trapezoid waveforms for this resolution. Since there were samples along the ramp part of trapezoid waveforms, the gradient timing delay induced trajectory

deviations were not simply trajectory shifts.

The auto-calibration region was  $36 \times 36$  and block size was  $6 \times 6$ . The rank threshold was chosen to be 64. Only 200 spokes were used for delays estimation since the center of k-space is oversampled and it was computationally more efficient to use fewer spokes. The algorithm was stopped after reaching a increment shift size of 0.001 sample.

### 5.3.3 In Vivo Experiments for Projection Reconstruction Trajectory and Spiral Trajectory

I also performed a free-breathing abdominal scan using 3D “stack of stars” trajectory (PR in two dimensions with 1 dimension of phase encoding) on a healthy volunteer. The following prescribed parameters were used: flip angle =  $10^\circ$ , FOV =  $32 \times 32 \text{ cm}^2$ , in-plane resolution =  $1 \times 1 \text{ mm}^2$ , slice thickness = 3 mm, TE/TR = 1.2 ms/ 5.12 ms, readout bandwidth =  $\pm 250 \text{ kHz}$  ( $2 \mu\text{s}/\text{sample}$ ), and 600 projections were acquired per phase encode step. The proposed method was applied on each axial slice after Fourier transform in the phase encode using similar parameter setting with the above examples. 200 projections were used to estimate gradient delays as they fully covered the auto-calibration k-space.

Spiral dataset was acquired from RTHawk 2D real-time environment. Variable density spiral with three interleaves was used. Each spiral has 3396 readout points and readout bandwidth =  $\pm 125 \text{ kHz}$  ( $4 \mu\text{s}/\text{sample}$ ). The delay estimation was performed on fully sampled auto-calibration data. After that, I used ESPIRiT [31] to compute sensitivity maps from correct auto-calibration data and applied CG SENSE [32] to reconstruct the images.

## 5.4 Results

### 5.4.1 Simulation Validation

Fig 5.2 shows numerical simulation results for a center-out radial trajectory with the true delay of 1 sample in x-axis and 2 samples in y-axis: top row of shows the sum of squares of the individual coil images and the estimated sensitivity maps from the calibration region; The middle row depicts the reconstructed sum of squares of coil images using the uncorrected coordinates and the corresponding sensitivity maps, where the image was distorted and the sensitivity maps were corrupted; the bottom row demonstrates the reconstructed image and resulting sensitivity maps corrected by the proposed method. The gradient delay artifacts visible near the scalp and artificial enhancement in the middle of the brain images (yellow arrows) were effectively eliminated by the proposed method (bottom row). The sensitivity maps in the presence of gradients delays also show incorrect contours (red arrows) corresponding to the skull that will corrupt parallel imaging reconstructions. These were corrected by the proposed method. Quantitatively, the estimated delay values of [0.9989 2.0014] in [x,y] are almost perfectly aligned with the ground truth  $\Delta(\vec{t}) = [1 \ 2]$ .



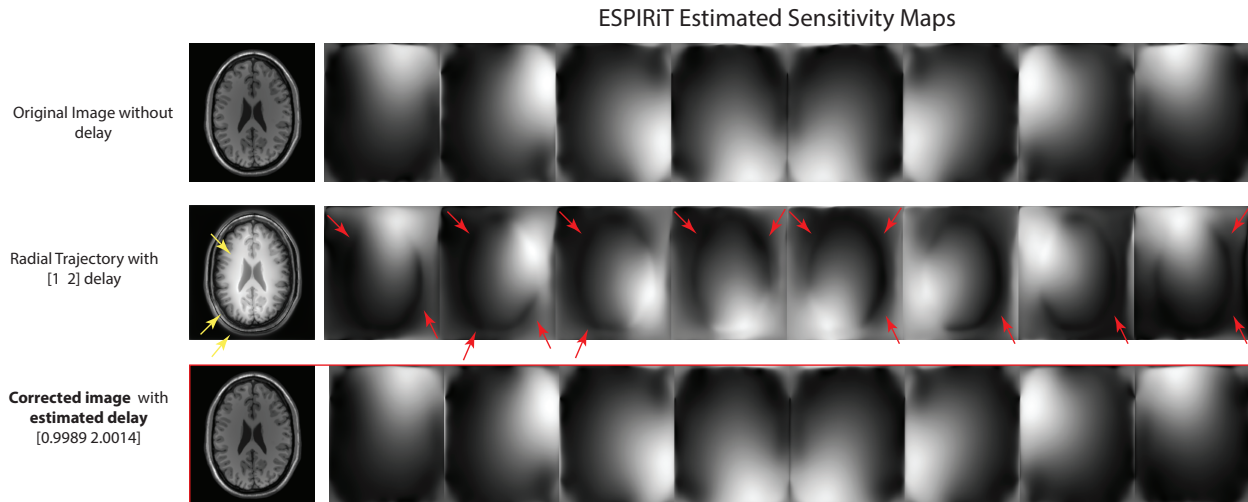


Figure 5.2: Simulation results with the proposed method: with gradient delays the image is distorted as the yellow arrows show; the sensitivity maps are corrupted as the brain edges are voided as the red arrows show (in the middle row). The proposed method is able to remove the artifacts, restore image quality and sensitivity maps; the delay estimation is accurate compared with ground truth.

Fig 5.3 shows the different artifact appearance for various trajectories and delays. As the yellow arrows indicate, artifacts can appear as erroneously enhanced contrast or void contrast, edge signal leakage for a center-out radial trajectory, rotation or edge signal leakage for a spiral trajectory, and streaking artifacts for a PR trajectory. All of these artifacts and distortions indicated in Fig 5.3 were effectively eliminated and contrast was restored by the proposed method, considerably improving the image quality. The table in Fig 5.3 presents the estimated delay values in different delay scenarios for different trajectories. The estimated delay values for different trajectories have a very good agreement with the ground truth.

SNR was computed from signal to noise ratio of a white matter region in the red box in Fig 5.3. From the table, I can see that the proposed method can estimate the gradient delay values with very high accuracy compared with ground truth for white matter SNRs of 50, 25, and 5. As SNR decreases, the estimation errors (mean and standard deviation) increase. Even for very low SNR value of 5, the proposed method still effectively estimated delay

values. The estimation errors are all less than 0.01 samples for radial and spiral trajectories and less than 0.05 samples for projection reconstruction trajectory.

In terms of convergence rate, the algorithms stopped around 50 iterations at the tolerance of 0.001 sample among all the simulation cases.

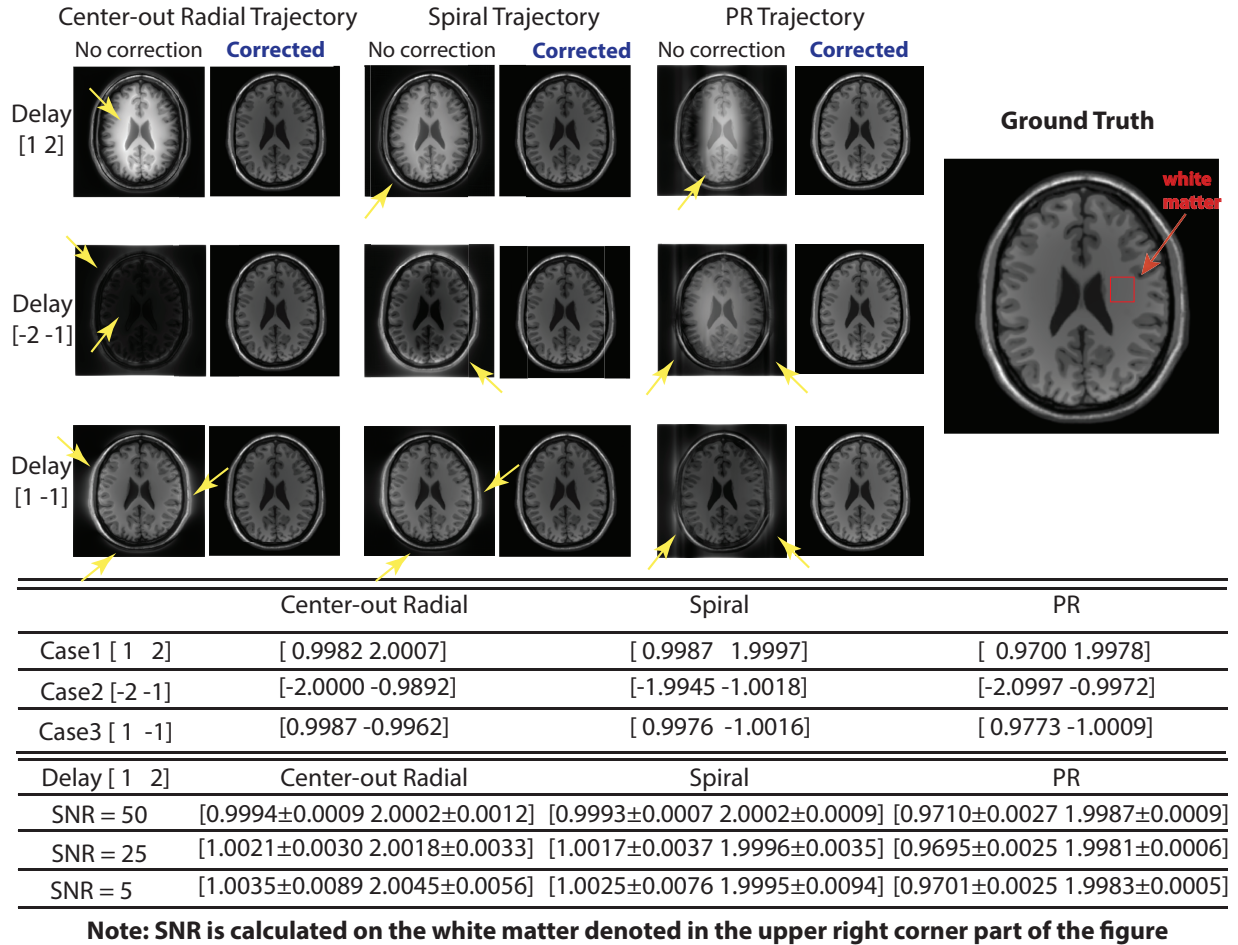


Figure 5.3: Simulation results with gradient delays for radial, spiral and PR trajectories: All artifacts indicated by arrows were effectively eliminated and contrast was restored by the proposed method, considerably improving the image quality. Quantitative analysis of the gradient delay estimation accuracy is listed in the top of the table. Noise sensitivity of the proposed method was evaluated with SNR = 5, 25, 50, as measured in the indicated white matter ROI. Even for SNR = 5, the proposed method still provides high estimation accuracy compared with the ground truth.

## 5.4.2 Phantom and In Vivo Experiments for Center-out Radial Trajectory

In center-out 2D radial trajectory experiments, I introduced a range of gradient delays ranging from  $-8 \mu\text{s}$  to  $8 \mu\text{s}$  on each axis compared to the scanner's calibrated gradient timings. Fig 5.4 shows a representative result with an introduced delay of  $-4 \mu\text{s}$  delay in the x-gradient and  $8 \mu\text{s}$  delay in the y-gradient for the phantom study, and  $4 \mu\text{s}$  delay in x-gradient and  $8 \mu\text{s}$  delay in y-gradient for the in vivo study. The sum of squares of the individual coil images reconstructed with nominal trajectory (on the left), corrected trajectory with system calibrated delays (in the middle) and estimated delays (in the right) in Fig 5.4. The results are displayed in the same window level for comparison. The contrast was restored and artifacts were removed by both the the proposed method and system calibration. The visible difference between the two corrected images is marginal. The delays estimated by the proposed method deviated by  $0.7\text{-}0.8 \mu\text{s}$  from the the system calibrations, which was consistent across the range of introduced gradient delays both in phantoms and in vivo.

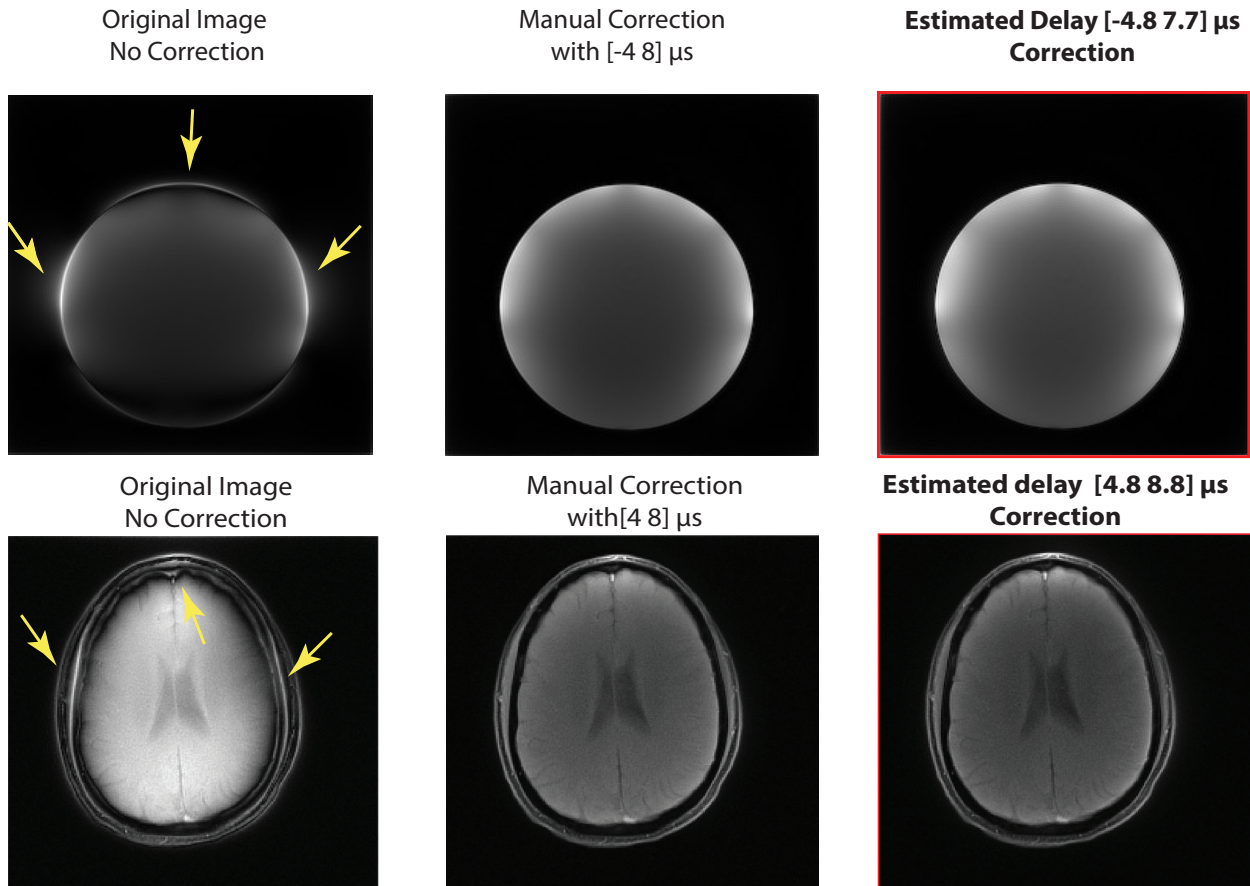


Figure 5.4: Phantom and in vivo results using center-out radial trajectory with the proposed method: Gradient delays induced artifacts are highlighted with yellow arrows in the left row. The contrast was restored and artifacts were removed by both the the proposed method and system calibration. The visible difference between the two corrected images is marginal.

### 5.4.3 In Vivo Experiments for Projection Reconstruction Trajectory

The proposed method was applied to different slices of a 3D stack of stars PR dataset acquired using the scanner's calibrated gradient timings. The streaking artifacts of each slice, which are clearly visible (on the left column) in Fig 5.5 and also appear in the simulation results in Fig 5.3, are greatly reduced after the correction with the proposed method (on the right),

resulting in a clearly improved image quality. The estimated delays were quite consistent from slice to slice, with minor differences ( $0.4 \mu\text{s}$ ) observed between abdominal and chest slices. This difference maybe related varying amplitudes of respiratory motion.

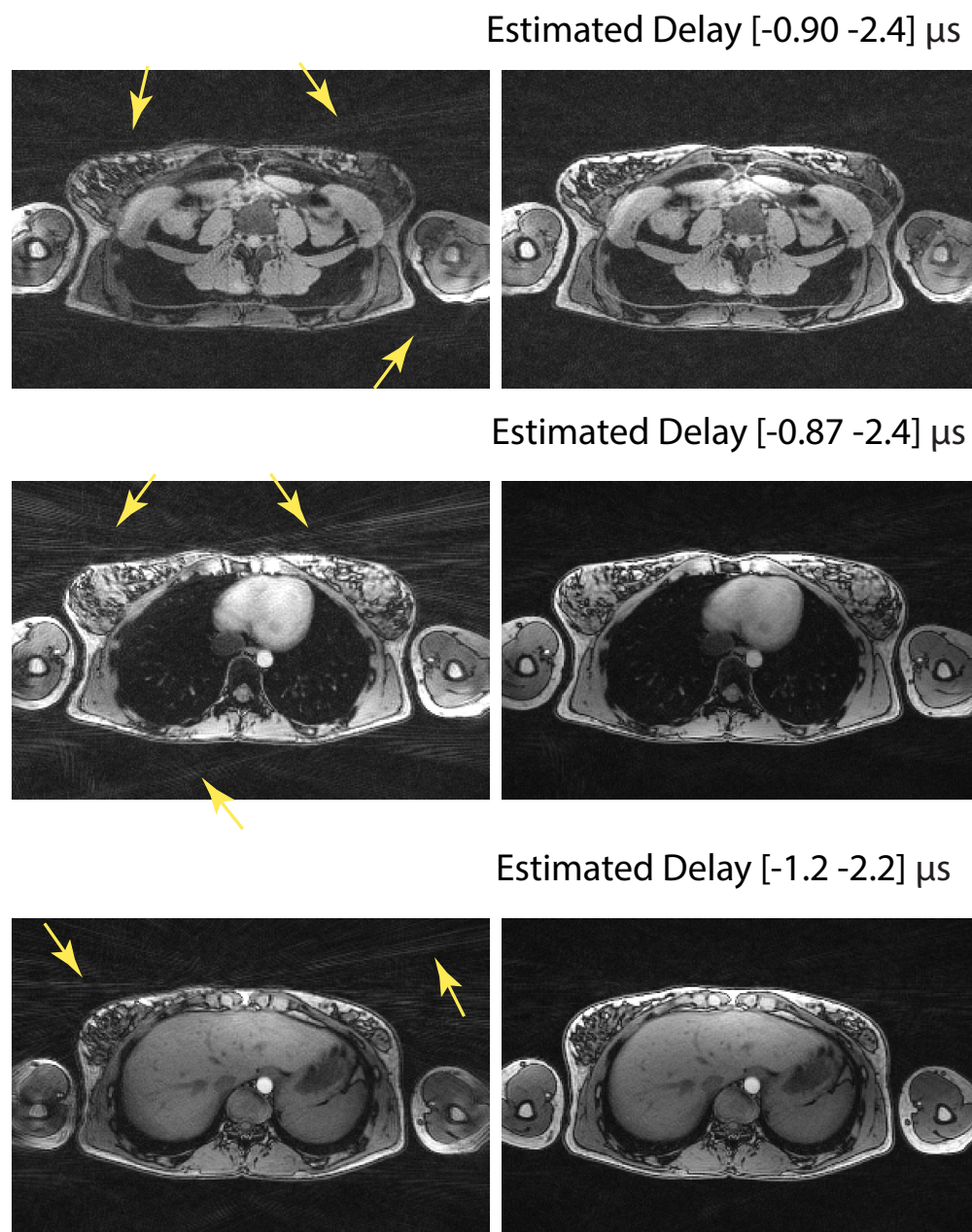


Figure 5.5: In vivo result using projection reconstruction trajectory: three different slices are displayed to show different anatomy from the same scan. The streaking artifacts are largely reduced for all the slices with the proposed method, resulting a clearly improved image quality.

#### 5.4.4 In Vivo Experiments for Spiral Trajectory

The proposed method was evaluated on various spiral datasets. Here, the representative results is shown in Fig 5.6. Edge leaking was suppressed (red arrows) and the small vessel (red circle) was made visible by the proposed method. Overall, the image quality was improved after applying the proposed method.

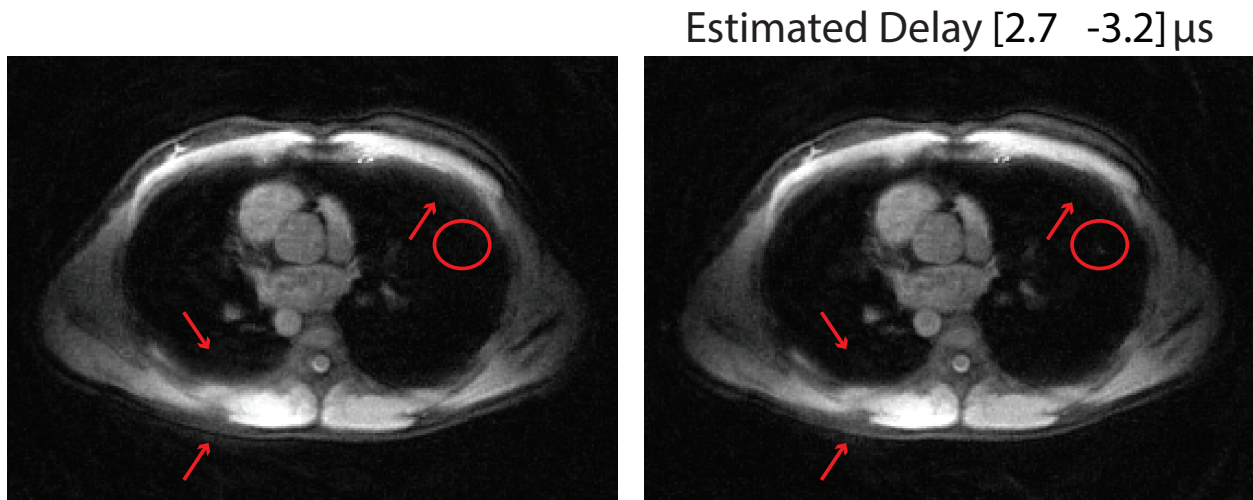


Figure 5.6: Real-time in vivo result using spiral trajectory: the proposed method results in improved image quality. The blurring edges are better delineated as red arrows show and small vessel structure is now visible as red circle shows.

## 5.5 Discussion

This work demonstrates a method to correct for gradient timing errors in center-out radial, projection reconstruction and spiral k-space trajectories, with results showing clearly improved image quality. It also provides accurate auto-calibration data for parallel imaging. This method iteratively enforces a low-rank property in the calibration region and estimates timing delays on individual gradient axes.

One advantage of the proposed method is that when sub-sample delays cannot be readily corrected for in the pulse sequence, the proposed method can provide more precise estimate

of the gradient delays.

The proposed method attempts to correct for gradient delays. The delays can originate from physical delays in the gradient and data acquisition components. Short-term linear eddy currents can also be approximated as a gradient delay. The proposed method can correct for delays from either source. A more detailed model could formulate the correction problem as eddy current estimation and solve for the corresponding eddy current parameters (e.g. time-constants and amplitude). But for some k-space trajectories (e.g. center-out radial), long term linear eddy currents might result in higher data correlation, in which case the low-rank model is not suitable for long-term eddy current correction. The proposed method is effective when the trajectory errors create more inconsistency (equivalently, higher rank) of the auto-calibration region. My conjecture is that the proposed method can better resolve gradient delays if k-space center is crossed in many different directions.

In this dissertation, I applied the proposed method when the center of k-space was fully-sampled or oversampled. However, if there is enough redundancy from multichannel coils, then undersampling in the calibration region to some extent is also tolerable. For example, in the center-out radial trajectory simulation, with 8 channel coils and calibration size of  $36 \times 36$ , I could still estimate delay values with less than 0.01 sample errors even with 40 spokes, which is equivalent to undersampling ratio of 2.8 with respect to Nyquist criterion.

The maximum delays that can be corrected by the proposed method depend on k-space trajectories, and how much redundancy the data can provide by the multichannel coils. As long as the delays do not result in a substantial chunk of missing data in the calibration region (which is beyond the limits of what parallel imaging can reconstruct), the proposed method can still correct for the delays.

From the simulation studies, even for very low SNR of 5, the proposed method was still able to correct for gradient timing delays with decent accuracy for different trajectories. Thus, high noise levels do not prohibit the application of the proposed method.

I note that for the proposed method, it is essential to use iterative method to approximate the pseudo inverse NUFFT operation, rather than the conventional gridding with density



compensation. This is because if I use density compensation from the nominal trajectory, then the resulting gradient timing delay estimation is not accurate. Alternatively, I would need to update density compensation for each iteration, which is computationally intensive. Instead, I used an iterative method with gridding [24] for each iteration to approximate the pseudo inverse NUFFT. Since I only perform the operations in the auto-calibration region, the computation burden is not heavy. All the examples presented in this dissertation were computed within one minute for a MATLAB implementation. This could be further sped up by using a high performance programming language.

The proposed method is essentially a low-rank matrix completion with alternating minimization, and does not assume convexity of the minimization problem. It is possible that the algorithm converges to a local minimum instead of a global minimum. Furthermore, the impacts of motion and chemical shifts on the performance of the proposed need to be investigated.

## 5.6 Conclusion

This chapter proposes a simple and robust method based on low-rank model and does not need any additional measurement scans. It determines the gradient timing delays and simultaneously yields corrected k-space auto calibration region signals for parallel imaging.

# Chapter 6

## Summary of Contribution and Future Work

This dissertation presented non-Cartesian MRI methods focused on advanced applications of metabolic imaging with hyperpolarized  $^{13}\text{C}$  MRSI and pulmonary imaging. In addition, a general solution to gradient delay errors for non-Cartesian imaging with multichannel datasets was developed and evaluated on commonly used non-Cartesian imaging strategies. Potential directions for future works are described at the end of this chapter.

### 6.1 Summary of Contribution

#### Design and Development of Concentric Rings for Hyperpolarized $^{13}\text{C}$ MR Spectroscopic Imaging

I presented theoretical and experimental results describing the quantitative tradeoff (in terms of robustness, acquisition time, SNR efficiency, and spectral bandwidth) between concentric rings, EPSI and spiral trajectories described in Chapter 3. Using concentric rings trajectory allows for robust and flexible implementations for  $^{13}\text{C}$  spectroscopic imaging and results in excellent speed, bandwidth, and resolution performance for hyperpolarized  $^{13}\text{C}$  MRSI.

### **Motion Robust High Resolution Free-breathing Pulmonary Imaging**

I developed a novel and robust dynamic self-navigator method using locally low rank constraint. Using the dynamic self-navigator enables accurate estimation of the respiratory motion. I demonstrated two motion compensation methods and compared their efficacy. Overall, I described a complete and robust framework that integrates essential requirements for pulmonary MR imaging. Quantitative evaluation on more than 10 clinical patients shows that the proposed method yields improved image quality.

### **Estimation of Gradient Delays in non-Cartesian Parallel MRI**

I developed an algorithm to estimate gradient delays for non-Cartesian imaging with multi-channel datasets. I verified the proposed method in simulation on different trajectories and various SNR levels. I also applied the proposed method on experimental non-Cartesian applications for the center-out radial, projection reconstruction and spiral trajectories. Overall, I proposed a simple and effective method to correct for gradient timing errors in non-Cartesian MR imaging without any calibration scans, based on multichannel datasets.

## **6.2 Future Work**

This dissertation primarily presented methodological developments and preliminary results. The potential future work involves extension of current technical methods and exploring more clinical applications.

### **Dynamic 3D Self-Navigator**

I proposed a lower-resolution dynamic 3D navigator and used it to estimate superior/inferior translation of the diaphragm in this dissertation. However, this 3D dynamic navigator offers abundant motion information which remains unexplored. With extracting more comprehensive motion information, the proposed navigator can be integrated with a more explicit

motion compensation model, such as warping and motion vector field. The temporal resolution is not limited to the 300 ms (100 spokes) used in Chapter 4. Preliminary results have shown that the temporal resolution of the dynamic 3D navigator can be increased to 150 ms by using 50 spokes. Thus it should be possible to apply this dynamic 3D self-navigator to cardiac imaging applications or bulk motion estimation. More clinical works are necessary to validate these suggested applications.

### **Multi-scale Low Rank Model**

The locally low-rank model is parameterized by block sizes and regularization parameters. It is hard to find a single set of parameters to describe different types of motion. In this sense, the current locally low-rank model is extendable to multi-scale low-rank model [149] to capture motion at different scales, *e.g.* respiratory motion, cardiac motion, contrast motion and bulk motion from the same reconstruction. More technical work is necessary to evaluate this model.

### **High Spatial Resolution Dynamic Imaging with Locally Low Rank Constraints**

Locally low-rank constraints were used to reconstruct dynamic 3D navigators at the spatial resolution of 7.5 mm in Chapter 4. However, it is possible to use all the data along each spoke to achieve full resolution (*e.g.* 1.25 mm) dynamic images. In this sense, the dynamic images will provide both anatomical and dynamic information for evaluation. I have been able to improve the spatial resolution to 3 mm (still with 300 ms temporal resolution) on clinical patients and have been able to see small structures dynamically. It is possible that 3 mm spatial resolution dynamic images are sufficient to assess functional information for pulmonary applications. This is a promising direction to explore. However, the computation is very expensive. The full resolution dynamic imaging memory cost could be as high as terra bytes. This computation problem is not addressed in this dissertation. More works are needed to optimize the computation, such as parallel computing power through graphic-

processing-units (GPU) and distributed systems.

### **Estimate Eddy Current**

As mentioned in the Discussion section of Chapter 5, it is possible to correct for eddy currents with low-rank constraints on the calibration region. The basic assumption is that the eddy currents induced trajectory deviation will result in data inconsistency of the calibration region, thus inducing higher rank. However, in some scenarios like center-out radial or spiral trajectories, eddy currents might not introduce higher rank thus the basic assumption does not hold. Then, the proposed method is not able to estimate the eddy current errors. But it is still possible to use low-rank model to correct for eddy currents errors in projection reconstruction trajectory or other non-Cartesian trajectories where this basic assumption holds.

# Appendices

## Critical Symmetric EPSI Reconstruction

Currently, the Nyquist-constrained symmetric EPSI reconstruction is to separate the odd and even numbered retracing lines, perform the inverse Fourier transform separately and average the separate signals for better SNR [40]. But this kind of design and reconstruction over-prescribes the SBW, while not critically using up the sampling limits. Papoulis's generalized sampling theory [67] asserts that in some cases aliasing artifact-free signals can be reconstructed even if the Nyquist criterion is violated in some regions of the Fourier domain.

As is explicitly demonstrated in [68, 150], critical symmetric EPSI reconstruction can be regarded as a matrix inversion problem that even if the Nyquist criterion is violated in some regions of the spectral domain, but at the cost of noise amplification.

In Fig Appendix 1, we demonstrate the symmetric EPSI reconstruction algorithm. Here we only plot the  $K_x$ - $t$  joint domain since  $K_y$  (phase encoding direction) is uniform. Basically, the critical design of symmetric EPSI trajectory is to make sure the temporary sampling rate at  $K_x = 0$  fulfills Nyquist rate of the required spectral bandwidth (as the black star in Fig Appendix 1). Regarding to the non-uniform samples, each  $Kx_i$ 's non-uniformity is different, with different delay  $\Delta t_i$ . We separate the odd/even retracing lines based on the labels. For odd or even lines respectively, they are uniformly sampled but at the rate of  $2/SBW$ . We apply 1D inverse Fourier Transform in temporary domain to odd and even numbered retracing lines separately. The difference between odd and even lines reconstruction is the

linear phase combination (due to the delay in the sampling domain). Then, we apply the matrix inversion to recover the full spectra as shown in the following equation.

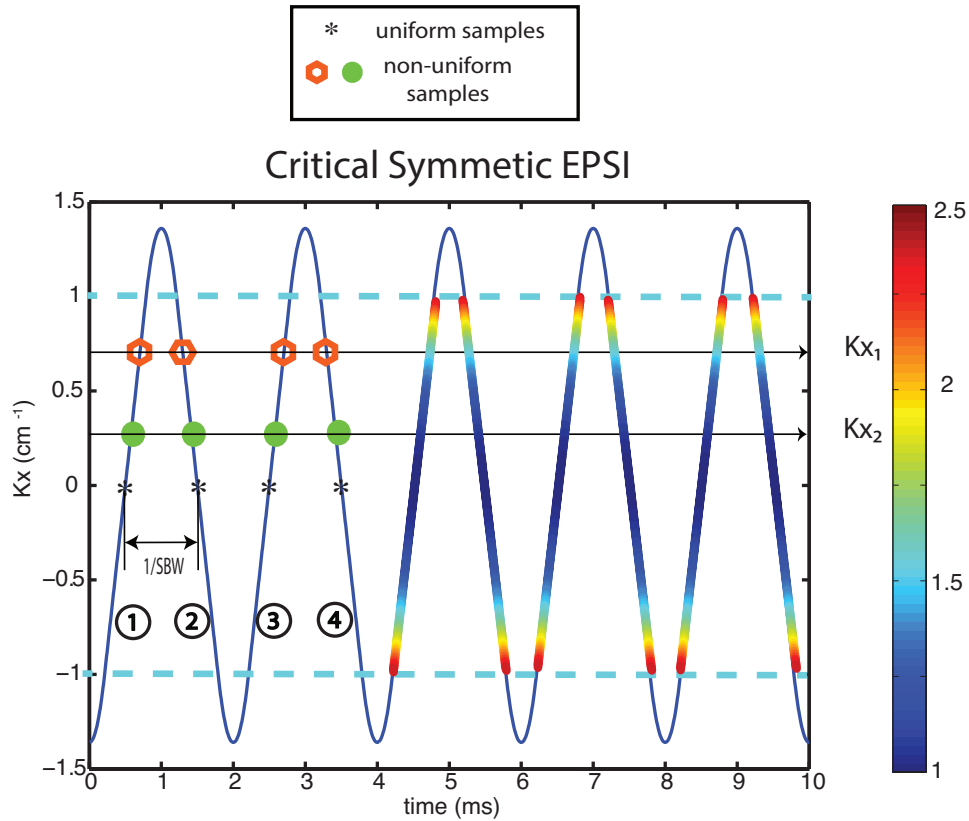


Figure Appendix 1: The area between the light blue dashed lines is the k-space used for the reconstruction; red and green samples are non-uniform  $Kx_i$  samples in temporal domain. With the above method described, the SBW could be doubled but at the cost of noise amplification. The colorbar indicated the noise amplification at different  $Kx_i$ .

The noise amplification is resulting from inverting the matrix  $\begin{pmatrix} 1 & 1 \\ 1 & e^{i\Delta t_i * SBW \pi} \end{pmatrix}$ , and it is shown in Fig Appendix 1 by color bar (as neatly explained in [150]).

For example, I consider a single k-space point at the  $Kx_1$  as Fig Appendix 2.

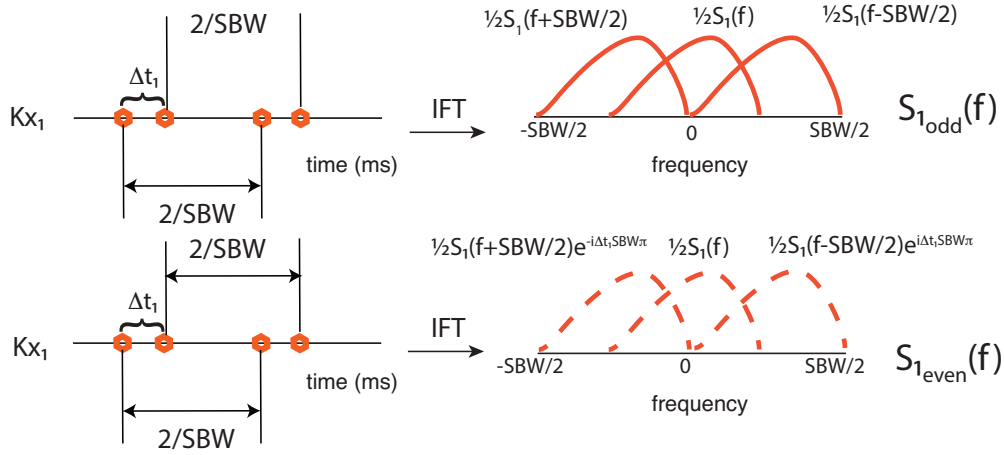


Figure Appendix 2: At  $Kx_1$ , I separate odd and even numbered samples out of their retracing lines and perform 1DFT respectively. Then I will see the spectral replica resulting from both odd and even echoes reconstruction. But there is a phase shift between the odd and even samples, which determines the inversion matrix.

The time interval between the odd and even data points ( $\Delta t_1$ ) is not equal to the interval between the even and the odd points ( $T - \Delta t_1$ ) and is dependent on  $Kx_1$ ; However, the time between odd(or even) points,  $T$  (*i.e.*, the prescribed  $2/SBW$ ), is a constant and independent on  $Kx_1$ . The interval  $0 \leq f \leq SBW/2$  spectrum  $S_1(f)$  can be recovered by the matrix inversion of the following equation:

$$\begin{pmatrix} 1 & 1 \\ 1 & e^{i\Delta t_1 * SBW\pi} \end{pmatrix} \begin{pmatrix} S_1(f) \\ S_1(f - SBW/2) \end{pmatrix} = \begin{pmatrix} S_{1\_odd}(f) \\ S_{1\_even}(f) \end{pmatrix}$$

The interval  $-SBW/2 \leq f \leq 0$  spectrum  $S_1(f)$  can be recovered by the matrix inversion of the similar equation:

$$\begin{pmatrix} 1 & 1 \\ 1 & e^{-i\Delta t_1 * SBW\pi} \end{pmatrix} \begin{pmatrix} S_1(f) \\ S_1(f + SBW/2) \end{pmatrix} = \begin{pmatrix} S_{1\_odd}(f) \\ S_{1\_even}(f) \end{pmatrix}$$

Due to the different delay  $\Delta t_i$ , the linear phase compensation is different for  $Kx_i$ . After I apply the appropriate phase compensation to all the  $Kx_i$ , 2D inverse Fourier Transform is applied on  $Kx$ - $Ky$  domain to reconstruct the whole spatial-spectral signal.



With this reconstruction method, I could exploit the intrinsic SBW by a factor of two with current Nyquist-constrained symmetric EPSI waveforms. So the SBW analyses from Fig 3.3 could be doubled for symmetric EPSI. However, I have to notice that the noise amplification of the matrix inversion could be large depending on the non-uniformity of delay  $\Delta t_i$  at different  $Kx_i$ . At larger  $Kx$ , that is for higher resolution, the condition worsens and the penalty is the higher sensitivity to noise. The overall noise amplification is the summation of the noise amplification at all the  $Kx$  coordinates as the plot shows. The finer the resolution, the larger noise amplification is. In addition, the precise coordinates of sampled data are important for image reconstruction using the this technique.

## References

- [1] Damian J. Tyler et al. “Magnetic resonance imaging with ultrashort TE (UTE) PULSE sequences: Technical considerations”. In: *Journal of Magnetic Resonance Imaging* 25.2 (2007), pp. 279–289. ISSN: 1522-2586. DOI: 10.1002/jmri.20851. URL: <http://dx.doi.org/10.1002/jmri.20851>.
- [2] G. H. Glover and J. M. Pauly. “Projection Reconstruction Techniques for Reduction of Motion Effects in MRI”. In: *Magnetic Resonance in Medicine* 28.2 (1992), pp. 275–289. ISSN: 1522-2594. DOI: 10.1002/mrm.1910280209. URL: <http://dx.doi.org/10.1002/mrm.1910280209>.
- [3] Jan-Ray Liao et al. “Reduction of motion artifacts in cine MRI using variable-density spiral trajectories”. In: *Magnetic Resonance in Medicine* 37.4 (1997), pp. 569–575. ISSN: 1522-2594. DOI: 10.1002/mrm.1910370416. URL: <http://dx.doi.org/10.1002/mrm.1910370416>.
- [4] Andrew C Larson et al. “Self-Gated Cardiac Cine MRI”. In: *Magnetic Resonance in Medicine* 51.1 (Jan. 2004), pp. 93–102. DOI: 10.1002/mrm.10664. URL: <http://www.ncbi.nlm.nih.gov/pmc/articles/PMC2396326/>.
- [5] Anja C. S. Brau and Jean H. Brittain. “Generalized self-navigated motion detection technique: Preliminary investigation in abdominal imaging”. In: *Magnetic Resonance in Medicine* 55.2 (2006), pp. 263–270. ISSN: 1522-2594. DOI: 10.1002/mrm.20785. URL: <http://dx.doi.org/10.1002/mrm.20785>.
- [6] Peter Kellman et al. “High Spatial and Temporal Resolution Cardiac Cine MRI from Retrospective Reconstruction of Data Acquired in Real Time Using Motion Correction and Resorting”. In: *Magnetic Resonance in Medicine* 62.6 (2009), pp. 1557–1564. ISSN: 1522-2594. DOI: 10.1002/mrm.22153. URL: <http://dx.doi.org/10.1002/mrm.22153>.

- [7] F. Bloch". "Nuclear Induction". In: *Physical Review* 69.3-4 (1946), pp. 127–127. DOI: 10.1103/PhysRev.69.127.
- [8] E. M. Purcell". "Resonance Absorption by Nuclear Magnetic Moments in a Solid". In: *Physical Review* 69.1-2 (1946), pp. 37–38. DOI: 10.1103/PhysRev.69.37.
- [9] P. C. LAUTERBUR. "Image Formation by Induced Local Interactions: Examples Employing Nuclear Magnetic Resonance". In: *Nature* 242.5394 (Mar. 1973), pp. 190–191. URL: <http://dx.doi.org/10.1038/242190a0>.
- [10] Lars G. Hanson. "Is quantum mechanics necessary for understanding magnetic resonance?" In: *Concepts in Magnetic Resonance Part A* 32A.5 (2008), pp. 329–340. ISSN: 1552-5023. DOI: 10.1002/cmr.a.20123. URL: <http://dx.doi.org/10.1002/cmr.a.20123>.
- [11] Dwight G. Nishimura. *Principles of magnetic resonance imaging*. Stanford: Stanford University, 2010, p. 238.
- [12] Kevin F. King Ph.D. Matt A. Bernstein Ph.D. and Xiaohong Joe Zhou. *Handbook of MRI pulse sequences*. New York: Elsevier Academic Press, 2004, p. 1017.
- [13] Anagha Deshmane et al. "Parallel MR imaging". In: *Journal of Magnetic Resonance Imaging* 36.1 (2012), pp. 55–72. DOI: 10.1002/jmri.23639. URL: <http://dx.doi.org/10.1002/jmri.23639>.
- [14] Katherine L. Wright et al. "Non-Cartesian parallel imaging reconstruction". In: *Journal of Magnetic Resonance Imaging* 40.5 (2014), pp. 1022–1040. ISSN: 1522-2586. DOI: 10.1002/jmri.24521. URL: <http://dx.doi.org/10.1002/jmri.24521>.
- [15] M. Lustig et al. "Compressed Sensing MRI". In: *IEEE Signal Processing Magazine* 25.2 (2008), pp. 72–82. ISSN: 1053-5888. DOI: 10.1109/MSP.2007.914728.

- [16] James G. Pipe. “Motion correction with PROPELLER MRI: Application to head motion and free-breathing cardiac imaging”. In: *Magnetic Resonance in Medicine* 42.5 (1999), pp. 963–969. ISSN: 1522-2594. DOI: 10.1002/(SICI)1522-2594(199911)42:5<963::AID-MRM17>3.0.CO;2-L. URL: [http://dx.doi.org/10.1002/\(SICI\)1522-2594\(199911\)42:5<963::AID-MRM17>3.0.CO;2-L](http://dx.doi.org/10.1002/(SICI)1522-2594(199911)42:5<963::AID-MRM17>3.0.CO;2-L).
- [17] Craig H. Meyer et al. “Fast Spiral Coronary Artery Imaging”. In: *Magnetic Resonance in Medicine* 28.2 (1992), pp. 202–213. ISSN: 1522-2594. DOI: 10.1002/mrm.1910280204. URL: <http://dx.doi.org/10.1002/mrm.1910280204>.
- [18] Gary H. Glover and Song Lai. “Self-navigated spiral fMRI: Interleaved versus single-shot”. In: *Magnetic Resonance in Medicine* 39.3 (1998), pp. 361–368. ISSN: 1522-2594. DOI: 10.1002/mrm.1910390305. URL: <http://dx.doi.org/10.1002/mrm.1910390305>.
- [19] Klaus Scheffler and Jürgen Hennig. “Reduced circular field-of-view imaging”. In: *Magnetic Resonance in Medicine* 40.3 (1998), pp. 474–480. ISSN: 1522-2594. DOI: 10.1002/mrm.1910400319. URL: <http://dx.doi.org/10.1002/mrm.1910400319>.
- [20] Dana C. Peters et al. “Undersampled projection reconstruction applied to MR angiography”. In: *Magnetic Resonance in Medicine* 43.1 (2000), pp. 91–101. ISSN: 1522-2594. DOI: 10.1002/(SICI)1522-2594(200001)43:1<91::AID-MRM11>3.0.CO;2-4. URL: [http://dx.doi.org/10.1002/\(SICI\)1522-2594\(200001\)43:1<91::AID-MRM11>3.0.CO;2-4](http://dx.doi.org/10.1002/(SICI)1522-2594(200001)43:1<91::AID-MRM11>3.0.CO;2-4).
- [21] Andrew V. Barger et al. “Time-resolved contrast-enhanced imaging with isotropic resolution and broad coverage using an undersampled 3D projection trajectory”. In: *Magnetic Resonance in Medicine* 48.2 (2002), pp. 297–305. ISSN: 1522-2594. DOI: 10.1002/mrm.10212. URL: <http://dx.doi.org/10.1002/mrm.10212>.
- [22] Peder E. Z. Larson. “MAGNETIC RESONANCE IMAGING OF SEMI-SOLID TISSUES”. PhD thesis. Stanford University, 2007.

- [23] Jiang Du et al. “Two-dimensional ultrashort echo time imaging using a spiral trajectory”. In: *Magnetic Resonance Imaging* 26.3 (), pp. 304–312. DOI: 10.1016/j.mri.2007.08.005. URL: <http://dx.doi.org/10.1016/j.mri.2007.08.005>.
- [24] Hisamoto Moriguchi and Jeffrey L. Duerk. “Iterative Next-Neighbor Regridding (INNG): Improved reconstruction from nonuniformly sampled k-space data using rescaled matrices”. In: *Magnetic Resonance in Medicine* 51.2 (2004), pp. 343–352. ISSN: 1522-2594. DOI: 10.1002/mrm.10692. URL: <http://dx.doi.org/10.1002/mrm.10692>.
- [25] Jeffrey A Fessler and Bradley P Sutton. “Nonuniform fast Fourier transforms using min-max interpolation”. In: *Signal Processing, IEEE Transactions on* 51.2 (2003), pp. 560–574.
- [26] Philip James Beatty. “RECONSTRUCTION METHODS FOR FAST MAGNETIC RESONANCE IMAGING”. PhD thesis. Stanford University, Dec. 2006.
- [27] P. B. Roemer et al. “The NMR phased array”. In: *Magnetic Resonance in Medicine* 16.2 (1990), pp. 192–225. DOI: 10.1002/mrm.1910160203. URL: <http://dx.doi.org/10.1002/mrm.1910160203>.
- [28] Klaas P. Pruessmann et al. “SENSE: Sensitivity encoding for fast MRI”. In: *Magnetic Resonance in Medicine* 42.5 (1999), pp. 952–962. ISSN: 1522-2594. DOI: 10.1002/(SICI)1522-2594(199911)42:5<952::AID-MRM16>3.0.CO;2-S. URL: [http://dx.doi.org/10.1002/\(SICI\)1522-2594\(199911\)42:5<952::AID-MRM16>3.0.CO;2-S](http://dx.doi.org/10.1002/(SICI)1522-2594(199911)42:5<952::AID-MRM16>3.0.CO;2-S).
- [29] Mark A. Griswold et al. “Generalized autocalibrating partially parallel acquisitions (GRAPPA)”. In: *Magnetic Resonance in Medicine* 47.6 (2002), pp. 1202–1210. ISSN: 1522-2594. DOI: 10.1002/mrm.10171. URL: <http://dx.doi.org/10.1002/mrm.10171>.
- [30] Michael Lustig and John M. Pauly. “SPIRiT: Iterative self-consistent parallel imaging reconstruction from arbitrary k-space”. In: *Magnetic Resonance in Medicine* 64.2

- (2010), pp. 457–471. ISSN: 1522-2594. DOI: 10.1002/mrm.22428. URL: <http://dx.doi.org/10.1002/mrm.22428>.
- [31] Martin Uecker et al. “ESPIRiT—an eigenvalue approach to autocalibrating parallel MRI: Where SENSE meets GRAPPA”. In: *Magnetic Resonance in Medicine* 71.3 (2014), pp. 990–1001. ISSN: 1522-2594. DOI: 10.1002/mrm.24751. URL: <http://dx.doi.org/10.1002/mrm.24751>.
- [32] Klaas P. Pruessmann et al. “Advances in sensitivity encoding with arbitrary k-space trajectories”. In: *Magnetic Resonance in Medicine* 46.4 (2001), pp. 638–651. ISSN: 1522-2594. DOI: 10.1002/mrm.1241. URL: <http://dx.doi.org/10.1002/mrm.1241>.
- [33] Neal Parikh and Stephen Boyd. “Proximal Algorithms”. In: *Foundations and Trends in Optimization* 1.3 (2014), pp. 127–239.
- [34] Michael Lustig, David Donoho, and John M. Pauly. “Sparse MRI: The Application of Compressed Sensing for Rapid MR Imaging”. In: *Magnetic Resonance in Medicine* 58.6 (2007), pp. 1182–1195. ISSN: 1522-2594. DOI: 10.1002/mrm.21391. URL: <http://dx.doi.org/10.1002/mrm.21391>.
- [35] Stefanie Winkelmann et al. “An optimal radial profile order based on the Golden Ratio for time-resolved MRI”. In: *IEEE transactions on medical imaging* 26.1 (2007), pp. 68–76.
- [36] John Kurhanewicz et al. “Analysis of cancer metabolism by imaging hyperpolarized nuclei: prospects for translation to clinical research”. In: *Neoplasia (New York, NY)* 13.2 (2011), p. 81.
- [37] Jan H Ardenkjær-Larsen et al. “Increase in signal-to-noise ratio of  $> 10,000$  times in liquid-state NMR”. In: *Proceedings of the National Academy of Sciences* 100.18 (2003), pp. 10158–10163.

- [38] Sarah J. Nelson et al. “Metabolic Imaging of Patients with Prostate Cancer Using Hyperpolarized [1-13C]Pyruvate”. In: *Science Translational Medicine* 5.198 (2013), 198ra108. DOI: 10.1126/scitranslmed.3006070. eprint: <http://stm.sciencemag.org/content/5/198/198ra108.full.pdf>. URL: <http://stm.sciencemag.org/content/5/198/198ra108.abstract>.
- [39] Charles H Cunningham et al. “Design of flyback echo-planar readout gradients for magnetic resonance spectroscopic imaging”. In: *Magnetic resonance in medicine* 54.5 (2005), pp. 1286–1289.
- [40] Y-F. Yen et al. “Imaging considerations for in vivo 13C metabolic mapping using hyperpolarized 13C-pyruvate”. In: *Magnetic Resonance in Medicine* 62.1 (2009), pp. 1–10. ISSN: 1522-2594. DOI: 10.1002/mrm.21987. URL: <http://dx.doi.org/10.1002/mrm.21987>.
- [41] Marc S. Ramirez et al. “Radial spectroscopic MRI of hyperpolarized [1-13C] pyruvate at 7 tesla”. In: *Magnetic Resonance in Medicine* 72.4 (2014), pp. 986–995. ISSN: 1522-2594. DOI: 10.1002/mrm.25004. URL: <http://dx.doi.org/10.1002/mrm.25004>.
- [42] Dirk Mayer et al. “Fast metabolic imaging of systems with sparse spectra: application for hyperpolarized 13C imaging”. In: *Magn Reson Med* 56.4 (2006), pp. 932–7.
- [43] Sonal Josan et al. “Dynamic metabolic imaging of hyperpolarized [2-13C]pyruvate using spiral chemical shift imaging with alternating spectral band excitation”. In: *Magnetic Resonance in Medicine* 71.6 (2014), pp. 2051–2058. ISSN: 1522-2594. DOI: 10.1002/mrm.24871. URL: <http://dx.doi.org/10.1002/mrm.24871>.
- [44] Jochen Leupold et al. “Fast multiecho balanced SSFP metabolite mapping of (1)H and hyperpolarized (13)C compounds”. In: *MAGMA* 22.4 (2009), pp. 251–6. DOI: 10.1007/s10334-009-0169-z.

- [45] Florian Wiesinger et al. “IDEAL spiral CSI for dynamic metabolic MR imaging of hyperpolarized [1-13C]pyruvate”. In: *Magn Reson Med* 68.1 (2012), pp. 8–16. DOI: 10.1002/mrm.23212.
- [46] Jeremy W. Gordon et al. “Joint spatial-spectral reconstruction and k-t spirals for accelerated 2D spatial/1D spectral imaging of 13C dynamics”. In: *Magnetic Resonance in Medicine* 71.4 (2014), pp. 1435–1445. ISSN: 1522-2594. DOI: 10.1002/mrm.24796. URL: <http://dx.doi.org/10.1002/mrm.24796>.
- [47] Cornelius von Morze et al. “Multi-band frequency encoding method for metabolic imaging with hyperpolarized [1-(13)C]pyruvate.” eng. In: *J Magn Reson* 211.2 (2011), pp. 109–113. ISSN: 1096-0856 (Electronic); 1090-7807 (Linking). DOI: 10.1016/j.jmr.2011.04.007.
- [48] Angus Z Lau et al. “Rapid multislice imaging of hyperpolarized 13C pyruvate and bicarbonate in the heart”. In: *Magn Reson Med* 64.5 (2010), pp. 1323–31. DOI: 10.1002/mrm.22525.
- [49] Charles H Cunningham et al. “Pulse sequence for dynamic volumetric imaging of hyperpolarized metabolic products”. In: *J Magn Reson* 193.1 (2008), pp. 139–146.
- [50] Arjun Arunachalam et al. “Accelerated spectroscopic imaging of hyperpolarized C-13 pyruvate using SENSE parallel imaging”. In: *NMR in Biomedicine* 22.8 (2009), pp. 867–873.
- [51] James Tropp et al. “Multi-Channel Metabolic Imaging, with SENSE reconstruction, of Hyperpolarized [1-13C] Pyruvate in a Live Rat at 3.0 tesla on a Clinical MR Scanner”. In: *J Magn Reson* 208.1 (2011), pp. 171–177. DOI: 10.1016/j.jmr.2010.10.007.
- [52] Michael A Ohliger et al. “Combined parallel and partial fourier MR reconstruction for accelerated 8-channel hyperpolarized carbon-13 in vivo magnetic resonance Spectroscopic imaging (MRSI)”. In: *J Magn Reson Imaging* 38.3 (2013), pp. 701–13. DOI: 10.1002/jmri.23989.



- [53] Peder E Z Larson et al. “Fast dynamic 3D MR spectroscopic imaging with compressed sensing and multiband excitation pulses for hyperpolarized  $^{13}\text{C}$  studies”. In: *Magn Reson Med* 65.3 (2011), pp. 610–9. DOI: 10.1002/mrm.22650.
- [54] Simon Hu et al. “3D compressed sensing for highly accelerated hyperpolarized  $^{13}\text{C}$  MRSI with in vivo applications to transgenic mouse models of cancer”. In: *Magnetic Resonance in Medicine* 63.2 (2010), pp. 312–321. ISSN: 1522-2594. DOI: 10.1002/mrm.22233. URL: <http://dx.doi.org/10.1002/mrm.22233>.
- [55] Kilian Weiss et al. “Accelerating hyperpolarized metabolic imaging of the heart by exploiting spatiotemporal correlations”. In: *NMR in Biomedicine* 26.11 (2013), pp. 1380–1386. ISSN: 1099-1492. DOI: 10.1002/nbm.2963. URL: <http://dx.doi.org/10.1002/nbm.2963>.
- [56] David M. Wilson et al. “Multi-compound Polarization by DNP Allows Simultaneous Assessment of Multiple Enzymatic Activities In Vivo”. In: *J Magn Reson* 205.1 (2010), pp. 141–147.
- [57] Albert P. Chen et al. “Simultaneous investigation of cardiac pyruvate dehydrogenase flux, Krebs cycle metabolism and pH, using hyperpolarized  $[1,2-^{13}\text{C}_2]$ pyruvate in vivo”. In: *NMR Biomed* 25.2 (2012), pp. 305–311. ISSN: 1099-1492. DOI: 10.1002/nbm.1749. URL: <http://dx.doi.org/10.1002/nbm.1749>.
- [58] P Mansfield. “Spatial mapping of the chemical shift in NMR”. In: *Magn Reson Med* 1.3 (1984), pp. 370–86.
- [59] Elfar Adalsteinsson et al. “Volumetric spectroscopic imaging with spiral-based k-space trajectories”. In: *Magnetic resonance in medicine* 39.6 (1998), pp. 889–898.
- [60] Dong-Hyun Kim and Daniel M. Spielman. “Reducing gradient imperfections for spiral magnetic resonance spectroscopic imaging”. In: *Magnetic Resonance in Medicine* 56.1 (2006), pp. 198–203. ISSN: 1522-2594. DOI: 10.1002/mrm.20928. URL: <http://dx.doi.org/10.1002/mrm.20928>.

- [61] Hochong H Wu, Jin Hyung Lee, and Dwight G Nishimura. “MRI using a concentric rings trajectory”. In: *Magnetic Resonance in Medicine* 59.1 (2008), pp. 102–112.
- [62] Holden H. Wu. “MAGNETIC RESONANCE IMAGING USING A CONCENTRIC RINGS K-SPACE TRAJECTORY”. PhD thesis. Stanford University, Sept. 2009.
- [63] Kie Tae Kwon et al. “Three-dimensional magnetization-prepared imaging using a concentric cylinders trajectory”. In: *Magnetic Resonance in Medicine* 71.5 (2014), pp. 1700–1710. ISSN: 1522-2594. DOI: 10.1002/mrm.24823. URL: <http://dx.doi.org/10.1002/mrm.24823>.
- [64] Jon K. Furuyama, Neil E. Wilson, and M. Albert Thomas. “Spectroscopic imaging using concentrically circular echo-planar trajectories in vivo”. In: *Magnetic Resonance in Medicine* 67.6 (2012), pp. 1515–1522. ISSN: 1522-2594. DOI: 10.1002/mrm.23184. URL: <http://dx.doi.org/10.1002/mrm.23184>.
- [65] Brian A Hargreaves, Dwight G Nishimura, and Steven M Conolly. “Time-optimal multidimensional gradient waveform design for rapid imaging”. In: *Magnetic resonance in medicine* 51.1 (2004), pp. 81–92.
- [66] Inc. CVX Research. *CVX: Matlab Software for Disciplined Convex Programming, version 2.0*. <http://cvxr.com/cvx>. Aug. 2012.
- [67] A. Papoulis. “Generalized sampling expansion”. In: *Circuits and Systems, IEEE Transactions on* 24.11 (1977), pp. 652–654. ISSN: 0098-4094. DOI: 10.1109/TCS.1977.1084284.
- [68] Xiaoping Hu Gregory Metzger. “Application of Interlaced Fourier Transform to Echo-Planar Spectroscopic Imaging”. In: *J Magn Reson* 125.1 (1997), pp. 166–170.
- [69] Lei Zhao et al. “Gradient-Echo Imaging Considerations for Hyperpolarized  $^{129}\text{Xe}$  MR”. In: *Journal of Magnetic Resonance, Series B* 113.2 (1996), pp. 179–183.

- [70] Chi-Ming Tsai and Dwight G Nishimura. “Reduced aliasing artifacts using variable-density k-space sampling trajectories”. In: *Magnetic resonance in medicine* 43.3 (2000), pp. 452–458.
- [71] Felix A. Breuer et al. “General formulation for quantitative G-factor calculation in GRAPPA reconstructions”. In: *Magnetic Resonance in Medicine* 62.3 (2009), pp. 739–746. ISSN: 1522-2594. DOI: 10.1002/mrm.22066. URL: <http://dx.doi.org/10.1002/mrm.22066>.
- [72] Matt A. Bernstein, Kevin F. King, and Xiaohong Joe Zhou. *Handbook of MRI Pulse Sequence*. MA, USA: Elsevier Academic Press, 2004, pp. 726–732.
- [73] James G Pipe, Ergun Ahunbay, and Padmanabhan Menon. “Effects of interleaf order for spiral MRI of dynamic processes”. In: *Magnetic resonance in medicine* 41.2 (1999), pp. 417–422.
- [74] Mat A. Bernstein et al. “Concomitant gradient terms in phase contrast MR: Analysis and correction”. In: *Magnetic Resonance in Medicine* 39.2 (1998), pp. 300–308. ISSN: 1522-2594. DOI: 10.1002/mrm.1910390218. URL: <http://dx.doi.org/10.1002/mrm.1910390218>.
- [75] Rebecca Smith-Bindman et al. “Use of diagnostic imaging studies and associated radiation exposure for patients enrolled in large integrated health care systems, 1996–2010”. In: *JAMA* 307.22 (2012), pp. 2400–2409. DOI: 10.1001/jama.2012.5960. eprint: [/data/Journals/JAMA/24193/joc120030\\_2400\\_2409.pdf](/data/Journals/JAMA/24193/joc120030_2400_2409.pdf). URL: [+http://dx.doi.org/10.1001/jama.2012.5960](http://dx.doi.org/10.1001/jama.2012.5960).
- [76] Peter B. Bach et al. “Benefits and harms of ct screening for lung cancer: A systematic review”. In: *JAMA* 307.22 (2012), pp. 2418–2429. DOI: 10.1001/jama.2012.5521. eprint: [/data/Journals/JAMA/24193/jrv120003\\_2418\\_2429.pdf](/data/Journals/JAMA/24193/jrv120003_2418_2429.pdf). URL: [+http://dx.doi.org/10.1001/jama.2012.5521](http://dx.doi.org/10.1001/jama.2012.5521).

- [77] Diana L Miglioretti et al. “Pediatric Computed Tomography and Associated Radiation Exposure and Estimated Cancer Risk”. In: *JAMA pediatrics* 167.8 (Aug. 2013), pp. 700–707. DOI: 10.1001/jamapediatrics.2013.311. URL: <http://www.ncbi.nlm.nih.gov/pmc/articles/PMC3936795/>.
- [78] Mannudeep K. Kalra, Aaron D. Sodickson, and William W. Mayo-Smith. “CT Radiation: Key Concepts for Gentle and Wise Use”. In: *RadioGraphics* 35.6 (2015). PMID: 26466180, pp. 1706–1721. DOI: 10.1148/rg.2015150118. eprint: <http://dx.doi.org/10.1148/rg.2015150118>. URL: <http://dx.doi.org/10.1148/rg.2015150118>.
- [79] C. J. Bergin, J. M. Pauly, and A Macovski. “Lung Parenchyma: Projection Reconstruction MR Imaging.” In: *Radiology* 179.3 (1991), pp. 777–781.
- [80] J R Mayo, A. Mackay, and N L Müller. “MR Imaging of The Lungs: Value of Short TE Spin-echo Pulse Sequences”. In: *Ajr American Journal of Roentgenology* 159.5 (1992), pp. 951–6.
- [81] Hiroto Hatabu et al. “MR imaging of Pulmonary Parenchyma with A Half-Fourier Single-shot Turbo Spin-echo (HASTE) Sequence”. In: *European Journal of Radiology* 29.2 (1999), pp. 152 –159. ISSN: 0720-048X. DOI: [http://dx.doi.org/10.1016/S0720-048X\(98\)00167-3](http://dx.doi.org/10.1016/S0720-048X(98)00167-3). URL: <http://www.sciencedirect.com/science/article/pii/S0720048X98001673>.
- [82] Yoshiharu Ohno et al. “N Stage Disease in Patients with Non-Small Cell Lung Cancer: Efficacy of Quantitative and Qualitative Assessment with STIR Turbo Spin-Echo Imaging, Diffusion-weighted MR Imaging, and Fluorodeoxyglucose PET/CT”. In: *Radiology* 261.2 (2011). PMID: 21926377, pp. 605–615. DOI: 10.1148/radiol.11110281. eprint: <http://dx.doi.org/10.1148/radiol.11110281>. URL: <http://dx.doi.org/10.1148/radiol.11110281>.
- [83] G. Lutterbey et al. “Lung MRI at 3.0 T: A comparison of Helical CT and High-field MRI in the Detection of Diffuse Lung Disease”. In: *European Radiology* 15.2

- (2004), pp. 324–328. ISSN: 1432-1084. DOI: 10.1007/s00330-004-2548-1. URL: <http://dx.doi.org/10.1007/s00330-004-2548-1>.
- [84] Markus Weiger, Franciszek Hennel, and Klaas P. Pruessmann. “Sweep MRI with Algebraic Reconstruction”. In: *Magnetic Resonance in Medicine* 64.6 (2010), pp. 1685–1695. ISSN: 1522-2594. DOI: 10.1002/mrm.22516. URL: <http://dx.doi.org/10.1002/mrm.22516>.
- [85] Osamu Togao et al. “Ultrashort Echo Time (UTE) MRI of the Lung: Assessment of Tissue Density in the Lung Parenchyma”. In: *Magnetic Resonance in Medicine* 64.5 (2010), pp. 1491–1498. ISSN: 1522-2594. DOI: 10.1002/mrm.22521. URL: <http://dx.doi.org/10.1002/mrm.22521>.
- [86] Kevin M. Johnson et al. “Optimized 3D Ultrashort Echo Time Pulmonary MRI”. In: *Magnetic Resonance in Medicine* 70.5 (2013), pp. 1241–1250. ISSN: 1522-2594. DOI: 10.1002/mrm.24570. URL: <http://dx.doi.org/10.1002/mrm.24570>.
- [87] Mark E. Crowe et al. “Automated rectilinear self-gated cardiac cine imaging”. In: *Magnetic Resonance in Medicine* 52.4 (2004), pp. 782–788. ISSN: 1522-2594. DOI: 10.1002/mrm.20212. URL: <http://dx.doi.org/10.1002/mrm.20212>.
- [88] Martin Buehrer et al. “Prospective self-gating for simultaneous compensation of cardiac and respiratory motion”. In: *Magnetic Resonance in Medicine* 60.3 (2008), pp. 683–690. ISSN: 1522-2594. DOI: 10.1002/mrm.21697. URL: <http://dx.doi.org/10.1002/mrm.21697>.
- [89] Pascal Spincemaille et al. “Kalman filtering for real-time navigator processing”. In: *Magnetic Resonance in Medicine* 60.1 (2008), pp. 158–168. ISSN: 1522-2594. DOI: 10.1002/mrm.21649. URL: <http://dx.doi.org/10.1002/mrm.21649>.
- [90] C. A. Bookwalter, M. A. Griswold, and J. L. Duerk. “Multiple Overlapping k-Space Junctions for Investigating Translating Objects (MOJITO)”. In: *IEEE Transactions*

- on Medical Imaging* 29.2 (2010), pp. 339–349. ISSN: 0278-0062. DOI: 10.1109/TMI.2009.2029854.
- [91] Joseph Y. Cheng et al. “Nonrigid motion correction in 3D using autofocusing with localized linear translations”. In: *Magnetic Resonance in Medicine* 68.6 (2012), pp. 1785–1797. ISSN: 1522-2594. DOI: 10.1002/mrm.24189. URL: <http://dx.doi.org/10.1002/mrm.24189>.
- [92] Robert Manka et al. “Performance of Simultaneous Cardiac-Respiratory Self-gated Three-dimensional MR Imaging of the Heart: Initial Experience”. In: *Radiology* 255.3 (2010). PMID: 20501728, pp. 909–916. DOI: 10.1148/radiol.10091103. eprint: <http://dx.doi.org/10.1148/radiol.10091103>. URL: <http://dx.doi.org/10.1148/radiol.10091103>.
- [93] Stefan Weick et al. “DC-gated high resolution three-dimensional lung imaging during free-breathing”. In: *Journal of Magnetic Resonance Imaging* 37.3 (2013), pp. 727–732. ISSN: 1522-2586. DOI: 10.1002/jmri.23798. URL: <http://dx.doi.org/10.1002/jmri.23798>.
- [94] Muhammad Usman et al. “Compressive Manifold Learning: Estimating One-dimensional Respiratory Motion Directly from Undersampled K-space Data”. In: *Magnetic Resonance in Medicine* 72.4 (2014), pp. 1130–1140. ISSN: 1522-2594. DOI: 10.1002/mrm.25010. URL: <http://dx.doi.org/10.1002/mrm.25010>.
- [95] Jan Paul et al. “High-resolution Respiratory Self-gated Golden Angle Cardiac MRI: Comparison of Self-gating Methods in Combination with k-t SPARSE SENSE”. In: *Magnetic Resonance in Medicine* 73.1 (2015), pp. 292–298. ISSN: 1522-2594. DOI: 10.1002/mrm.25102. URL: <http://dx.doi.org/10.1002/mrm.25102>.
- [96] Marta Tibiletti et al. “Multistage Three-dimensional UTE Lung Imaging by Image-based Self-gating”. In: *Magnetic Resonance in Medicine* 75.3 (2016), pp. 1324–1332.

- ISSN: 1522-2594. DOI: 10.1002/mrm.25673. URL: <http://dx.doi.org/10.1002/mrm.25673>.
- [97] P. G. Batchelor et al. “Matrix Description of General Motion Correction Applied to Multishot Images”. In: *Magnetic Resonance in Medicine* 54.5 (2005), pp. 1273–1280. ISSN: 1522-2594. DOI: 10.1002/mrm.20656. URL: <http://dx.doi.org/10.1002/mrm.20656>.
- [98] Freddy Odille et al. “Generalized Reconstruction by Inversion of Coupled Systems (GRICS) Applied to Free-breathing MRI”. In: *Magnetic Resonance in Medicine* 60.1 (2008), pp. 146–157. ISSN: 1522-2594. DOI: 10.1002/mrm.21623. URL: <http://dx.doi.org/10.1002/mrm.21623>.
- [99] Gastao Cruz et al. “Accelerated Motion Corrected Three-dimensional Abdominal MRI using Total Variation Regularized SENSE Reconstruction”. In: *Magnetic Resonance in Medicine* 75.4 (2016), pp. 1484–1498. ISSN: 1522-2594. DOI: 10.1002/mrm.25708. URL: <http://dx.doi.org/10.1002/mrm.25708>.
- [100] Dirk Manke et al. “Model evaluation and calibration for prospective respiratory motion correction in coronary MR angiography based on 3-D image registration.” eng. In: *IEEE Trans Med Imaging* 21.9 (2002), pp. 1132–1141. ISSN: 0278-0062 (Print); 0278-0062 (Linking). DOI: 10.1109/TMI.2002.804428.
- [101] Himanshu Bhat et al. “3D radial sampling and 3D affine transform-based respiratory motion correction technique for free-breathing whole-heart coronary MRA with 100% imaging efficiency”. In: *Magnetic Resonance in Medicine* 65.5 (2011), pp. 1269–1277. ISSN: 1522-2594. DOI: 10.1002/mrm.22717. URL: <http://dx.doi.org/10.1002/mrm.22717>.
- [102] Hui Xue et al. “Motion Compensated Magnetic Resonance Reconstruction Using Inverse-Consistent Deformable Registration: Application to Real-Time Cine Imag-

- ing”. In: *Medical image computing and computer-assisted intervention* 14.Pt 1 (2011), pp. 564–572. URL: <http://www.ncbi.nlm.nih.gov/pmc/articles/PMC3346952/>.
- [103] Johannes F. M. Schmidt et al. “Nonrigid retrospective respiratory motion correction in whole-heart coronary MRA”. In: *Magnetic Resonance in Medicine* 66.6 (2011), pp. 1541–1549. ISSN: 1522-2594. DOI: 10.1002/mrm.22939. URL: <http://dx.doi.org/10.1002/mrm.22939>.
- [104] Christian Buerger, Claudia Prieto, and Tobias Schaeffter. “Highly efficient 3D motion-compensated abdomen MRI from undersampled golden-RPE acquisitions”. In: *Magnetic Resonance Materials in Physics, Biology and Medicine* 26.5 (2013), pp. 419–429. ISSN: 1352-8661. DOI: 10.1007/s10334-013-0370-y. URL: <http://dx.doi.org/10.1007/s10334-013-0370-y>.
- [105] M. Salman Asif et al. “Motion-adaptive spatio-temporal regularization for accelerated dynamic MRI”. In: *Magnetic Resonance in Medicine* 70.3 (2013), pp. 800–812. ISSN: 1522-2594. DOI: 10.1002/mrm.24524. URL: <http://dx.doi.org/10.1002/mrm.24524>.
- [106] Nadia K. Paschke et al. “Comparison of image-based and reconstruction-based respiratory motion correction for golden radial phase encoding coronary MR angiography”. In: *Journal of Magnetic Resonance Imaging* 42.4 (2015), pp. 964–971. DOI: 10.1002/jmri.24858. URL: <http://dx.doi.org/10.1002/jmri.24858>.
- [107] Christopher M. Rank et al. “4D Respiratory Motion-compensated Image Reconstruction of Free-breathing Radial MR data with Very High undersampling”. In: *Magnetic Resonance in Medicine* (2016). doi:10.1002/mrm.26206. ISSN: 1522-2594. DOI: 10.1002/mrm.26206. URL: <http://dx.doi.org/10.1002/mrm.26206>.
- [108] Alexander Loktyushin et al. “Blind retrospective motion correction of MR images”. In: *Magnetic Resonance in Medicine* 70.6 (2013), pp. 1608–1618. ISSN: 1522-2594. DOI: 10.1002/mrm.24615. URL: <http://dx.doi.org/10.1002/mrm.24615>.



- [109] Mehdi H. Moghari et al. “Free-Breathing 3D Cardiac MRI Using Iterative Image-Based Respiratory Motion Correction”. In: *Magnetic Resonance in Medicine* 70.4 (2013), pp. 1005–1015. ISSN: 1522-2594. DOI: 10.1002/mrm.24538. URL: <http://dx.doi.org/10.1002/mrm.24538>.
- [110] R. Reeve Ingle et al. “Nonrigid Autofocus Motion Correction for Coronary MR Angiography with A 3D Cones Trajectory”. In: *Magnetic Resonance in Medicine* 72.2 (2014), pp. 347–361. ISSN: 1522-2594. DOI: 10.1002/mrm.24924. URL: <http://dx.doi.org/10.1002/mrm.24924>.
- [111] Jieying Luo et al. “Nonrigid motion correction with 3D image-based navigators for coronary MR angiography”. In: *Magnetic Resonance in Medicine* (2016), doi:10.1002/mrm.26273. ISSN: 1522-2594. DOI: 10.1002/mrm.26273. URL: <http://dx.doi.org/10.1002/mrm.26273>.
- [112] Kevin M. Johnson et al. “Improved Least Squares MR Image Reconstruction using Estimates of K-Space Data Consistency”. In: *Magnetic Resonance in Medicine* 67.6 (2012), pp. 1600–1608. ISSN: 1522-2594. DOI: 10.1002/mrm.23144. URL: <http://dx.doi.org/10.1002/mrm.23144>.
- [113] Joseph Y. Cheng et al. “Free-breathing Pediatric MRI with Nonrigid Motion Correction and Acceleration”. In: *Journal of Magnetic Resonance Imaging* 42.2 (2015), pp. 407–420. DOI: 10.1002/jmri.24785. URL: <http://dx.doi.org/10.1002/jmri.24785>.
- [114] Christoph Forman et al. “Reduction of respiratory motion artifacts for free-breathing whole-heart coronary MRA by weighted iterative reconstruction”. In: *Magnetic Resonance in Medicine* 73.5 (2015), pp. 1885–1895. ISSN: 1522-2594. DOI: 10.1002/mrm.25321. URL: <http://dx.doi.org/10.1002/mrm.25321>.
- [115] Tao Zhang et al. “Fast Pediatric 3D Free-breathing Abdominal Dynamic Contrast Enhanced MRI with High Spatiotemporal Resolution”. In: *Journal of Magnetic Res-*

- onance Imaging* 41.2 (2015), pp. 460–473. DOI: 10.1002/jmri.24551. URL: <http://dx.doi.org/10.1002/jmri.24551>.
- [116] Li Feng et al. “XD-GRASP: Golden-angle Radial MRI with Reconstruction of Extra Motion-state Dimensions using Compressed Sensing”. In: *Magnetic Resonance in Medicine* (2016), 75: 775–788. ISSN: 1522-2594. DOI: 10.1002/mrm.25665. URL: <http://dx.doi.org/10.1002/mrm.25665>.
- [117] J Trzasko, A Manduca, and E Borisch. “Local versus Global Low-rank Promotion in Dynamic MRI Series Reconstruction”. In: *Proc Int Symp Magn Reson in Medicine* (2011), p. 4371. DOI: 10.5296/jsss.v1i2.5769.s851. URL: <http://cds.ismrm.org/protected/11MProceedings/files/4371.pdf>.
- [118] Tao Zhang, John M. Pauly, and Ives R. Levesque. “Accelerating parameter mapping with a locally low rank constraint”. In: *Magnetic Resonance in Medicine* 73.2 (2015), pp. 655–661. ISSN: 1522-2594. DOI: 10.1002/mrm.25161. URL: <http://dx.doi.org/10.1002/mrm.25161>.
- [119] Tao Zhang et al. “Robust self-navigated body MRI using dense coil arrays”. In: *Magnetic Resonance in Medicine* 76.1 (2016), pp. 197–205. ISSN: 1522-2594. DOI: 10.1002/mrm.25858. URL: <http://dx.doi.org/10.1002/mrm.25858>.
- [120] Junmin Liu and Maria Drangova. “Combination of multidimensional navigator echoes data from multielement RF coil”. In: *Magnetic Resonance in Medicine* 64.4 (2010), pp. 1208–1214. ISSN: 1522-2594. DOI: 10.1002/mrm.22496. URL: <http://dx.doi.org/10.1002/mrm.22496>.
- [121] Li Feng et al. “Compressed sensing with synchronized cardio-respiratory sparsity for free-breathing cine MRI: initial comparative study on patients with arrhythmias”. In: *Journal of Cardiovascular Magnetic Resonance* 16.1 (2014), pp. 1–2. ISSN: 1532-429X. DOI: 10.1186/1532-429X-16-S1-017. URL: <http://dx.doi.org/10.1186/1532-429X-16-S1-017>.

- [122] Jing Liu et al. “Respiratory and cardiac self-gated free-breathing cardiac CINE imaging with multiecho 3D hybrid radial SSFP acquisition”. In: *Magnetic Resonance in Medicine* 63.5 (2010), pp. 1230–1237. ISSN: 1522-2594. DOI: 10.1002/mrm.22306. URL: <http://dx.doi.org/10.1002/mrm.22306>.
- [123] Amir Beck and Marc Teboulle. “A Fast Iterative Shrinkage-Thresholding Algorithm for Linear Inverse Problems”. In: *SIAM Journal on Imaging Sciences* 2.1 (2009), pp. 183–202. DOI: 10.1137/080716542. eprint: <http://dx.doi.org/10.1137/080716542>. URL: <http://dx.doi.org/10.1137/080716542>.
- [124] M. A. T. Figueiredo and R. D. Nowak. “An EM algorithm for wavelet-based image restoration”. In: *IEEE Transactions on Image Processing* 12.8 (2003), pp. 906–916. ISSN: 1057-7149. DOI: 10.1109/TIP.2003.814255.
- [125] Jiangtao Peng et al. “Asymmetric Least Squares for Multiple Spectra Baseline Correction”. In: *Analytica Chimica Acta* 683.1 (2010), pp. 63–68. ISSN: 0003-2670. DOI: <http://dx.doi.org/10.1016/j.aca.2010.08.033>. URL: <http://www.sciencedirect.com/science/article/pii/S0003267010010627>.
- [126] Stephen Boyd et al. “Distributed Optimization and Statistical Learning via the Alternating Direction Method of Multipliers”. In: *Found. Trends Mach. Learn.* 3.1 (Jan. 2011), pp. 1–122. ISSN: 1935-8237. DOI: 10.1561/22000000016. URL: <http://dx.doi.org/10.1561/22000000016>.
- [127] Martin Uecker et al. *BART: Berkeley Advanced Reconstruction Toolbox*. doi:10.5281/zenodo.50726. DOI: 10.5281/zenodo.50726. URL: 10.5281/zenodo.50726.
- [128] Sampada Bhawe et al. “Blind retrospective motion correction of MR images”. In: *Investigative Radiology* 51.6 (2016), pp. 387–399. ISSN: 0020-9996. DOI: 10.1097/RLI.0000000000000253. URL: <http://dx.doi.org/10.1097/RLI.0000000000000253>.

- [129] Nii Okai Addy et al. “High-resolution variable-density 3D cones coronary MRA”. In: *Magnetic Resonance in Medicine* 74.3 (2015), pp. 614–621. ISSN: 1522-2594. DOI: 10.1002/mrm.25803. URL: <http://dx.doi.org/10.1002/mrm.25803>.
- [130] Nii Okai Addy et al. “3D image-based navigators for coronary MR angiography”. In: *Magnetic Resonance in Medicine* (2016). doi:10.1002/mrm.26269. ISSN: 1522-2594. DOI: 10.1002/mrm.26269. URL: <http://dx.doi.org/10.1002/mrm.26269>.
- [131] Kevin M. Johnson. “Hybrid radial-cones trajectory for accelerated MRI”. In: *Magnetic Resonance in Medicine* (2016). doi:10.1002/mrm.26188. ISSN: 1522-2594. DOI: 10.1002/mrm.26188. URL: <http://dx.doi.org/10.1002/mrm.26188>.
- [132] Dana C. Peters, J. Andrew Derbyshire, and Elliot R. McVeigh. “Centering the projection reconstruction trajectory: Reducing gradient delay errors”. In: *Magnetic Resonance in Medicine* 50.1 (2003), pp. 1–6. ISSN: 1522-2594. DOI: 10.1002/mrm.10501. URL: <http://dx.doi.org/10.1002/mrm.10501>.
- [133] P. Speier and F. Trautwein. “Robust radial imaging with predetermined isotropic gradient delay correction”. In: *Proc. Intl. Soc. Mag. Reson. Med.* 14 (2006), p. 2379.
- [134] Yantian Zhang et al. “A novel k-space trajectory measurement technique”. In: *Magnetic Resonance in Medicine* 39.6 (1998), pp. 999–1004. ISSN: 1522-2594. DOI: 10.1002/mrm.1910390618. URL: <http://dx.doi.org/10.1002/mrm.1910390618>.
- [135] Jeff H. Duyn et al. “Simple Correction Method for k-Space Trajectory Deviations in MRI”. In: *Journal of Magnetic Resonance* 132.1 (1998), pp. 150–153. ISSN: 1090-7807. DOI: <http://dx.doi.org/10.1006/jmre.1998.1396>. URL: <http://www.sciencedirect.com/science/article/pii/S1090780798913969>.
- [136] P. Gurney, J. Pauly, and D. G. Nishimura. “A Simple Method for Measuring B<sub>0</sub> Eddy Currents”. In: *Proc. Intl. Soc. Mag. Reson. Med.* 13 (2005), p. 866.

- [137] Anagha Deshmane et al. “Self-calibrated trajectory estimation and signal correction method for robust radial imaging using GRAPPA operator gridding”. In: *Magnetic Resonance in Medicine* 75.2 (2016), pp. 883–896. ISSN: 1522-2594. DOI: 10.1002/mrm.25648. URL: <http://dx.doi.org/10.1002/mrm.25648>.
- [138] Christoph Barmet, Nicola De Zanche, and Klaas P. Pruessmann. “Spatiotemporal magnetic field monitoring for MR”. In: *Magnetic Resonance in Medicine* 60.1 (2008), pp. 187–197. DOI: 10.1002/mrm.21603. URL: <http://dx.doi.org/10.1002/mrm.21603>.
- [139] Nicola De Zanche et al. “NMR probes for measuring magnetic fields and field dynamics in MR systems”. In: *Magnetic Resonance in Medicine* 60.1 (2008), pp. 176–186. DOI: 10.1002/mrm.21624. URL: <http://dx.doi.org/10.1002/mrm.21624>.
- [140] K. T. Block and M. Uecker. “Simple method for adaptive gradient-delay compensation in radial MRI”. In: *Proc. Intl. Soc. Mag. Reson. Med.* 19 (2011), p. 2816.
- [141] D Smith and B Welch. “Self-calibrated gradient delay correction for golden angle radial MRI”. In: *Proc. Intl. Soc. Mag. Reson. Med.* 22 (2014), p. 229.
- [142] Tobias Wech et al. “Using self-consistency for an iterative trajectory adjustment (SCITA)”. In: *Magnetic Resonance in Medicine* 73.3 (2015), pp. 1151–1157. ISSN: 1522-2594. DOI: 10.1002/mrm.25244. URL: <http://dx.doi.org/10.1002/mrm.25244>.
- [143] Julianna D. Ianni and William A. Grissom. “Trajectory Auto-Corrected image reconstruction”. In: *Magnetic Resonance in Medicine* 76.3 (2016), pp. 757–768. ISSN: 1522-2594. DOI: 10.1002/mrm.25916. URL: <http://dx.doi.org/10.1002/mrm.25916>.
- [144] Nicole Seiberlich et al. “Non-Cartesian data reconstruction using GRAPPA operator gridding (GROG)”. In: *Magnetic Resonance in Medicine* 58.6 (2007), pp. 1257–1265. ISSN: 1522-2594. DOI: 10.1002/mrm.21435. URL: <http://dx.doi.org/10.1002/mrm.21435>.


- [145] Peter J. Shin et al. “Calibrationless parallel imaging reconstruction based on structured low-rank matrix completion”. In: *Magnetic Resonance in Medicine* 72.4 (2014), pp. 959–970. ISSN: 1522-2594. DOI: 10.1002/mrm.24997. URL: <http://dx.doi.org/10.1002/mrm.24997>.
- [146] E Peterson et al. “Acquisition-free nyquist ghost correction for parallel imaging accelerated epi.” In: *Proc. Intl. Soc. Mag. Reson. Med.* 23. 2015, p. 0075. URL: <http://cds.ismrm.org/protected/15MPresentations/abstracts/0075.pdf>.
- [147] Alan V Oppenheim, Alan S Willsky, and Syed Hamid Nawab. *Signals and systems*. Vol. 2. Prentice-Hall Englewood Cliffs, NJ, 1983.
- [148] M. Lustig, S. J. Kim, and J. M. Pauly. “A fast method for designing time-optimal gradient waveforms for arbitrary k-space trajectories”. In: *IEEE Transactions on Medical Imaging* 27.6 (2008), pp. 866–873. ISSN: 0278-0062. DOI: 10.1109/TMI.2008.922699.
- [149] F. Ong and M. Lustig. “Beyond Low Rank + Sparse: Multiscale Low Rank Matrix Decomposition”. In: *IEEE Journal of Selected Topics in Signal Processing* 10.4 (2016), pp. 672–687. ISSN: 1932-4553. DOI: 10.1109/JSTSP.2016.2545518.
- [150] Hisamoto Moriguchi and Jeffrey L. Duerk. “Bunched phase encoding (BPE): A new fast data acquisition method in MRI”. In: *Magnetic Resonance in Medicine* 55.3 (2006), pp. 633–648. ISSN: 1522-2594. DOI: 10.1002/mrm.20819. URL: <http://dx.doi.org/10.1002/mrm.20819>.

**Publishing Agreement**

*It is the policy of the University to encourage the distribution of all theses, dissertations, and manuscripts. Copies of all UCSF theses, dissertations, and manuscripts will be routed to the library via the Graduate Division. The library will make all theses, dissertations, and manuscripts accessible to the public and will preserve these to the best of their abilities, in perpetuity.*

***Please sign the following statement:***

*I hereby grant permission to the Graduate Division of the University of California, San Francisco to release copies of my thesis, dissertation, or manuscript to the Campus Library to provide access and preservation, in whole or in part, in perpetuity.*

  
\_\_\_\_\_  
Author Signature

12/12/2016  
\_\_\_\_\_  
Date